2014

Investigation of Thermo-Mechanical Fatigue Characteristics for Cast Aluminum (AL319-T7)

Luke Miller
University of Windsor

Investigation of Thermo-Mechanical Fatigue Characteristics for Cast Aluminum (AL319-T7)

By

Luke W. Miller

A Thesis Submitted to the Faculty of Graduate Studies through Mechanical, Automotive, and Materials Engineering in Partial Fulfillment of the Requirements for the Degree of Master of Applied Science at the University of Windsor

Windsor, Ontario, Canada

2014

Investigation of Thermal Mechanical Fatigue Characteristics for Cast Aluminum (AL319-T7)

By

Luke Miller

APPROVED BY:

_____

S. Cheng

Department of Civil and Environmental Engineering

_____

D. Green

Department of Mechanical, Automotive and Materials Engineering

_____

P. Frise, Co-Advisor

Department of Mechanical, Automotive and Materials Engineering

_____

F. Ghrib, Advisor

Department of Civil and Environmental Engineering

February 14th 2014

Declaration of Originality

I hereby certify that I am the sole author of this thesis and that no part of this thesis has been published or submitted for publication.

I certify that, to the best of my knowledge, my thesis does not infringe upon any copyright nor violate any proprietary rights and that any ideas, techniques, quotations, or any other material from the work of other people included in my thesis, published or otherwise, are fully acknowledged in accordance with the standard referencing practices.

I declare that this is a true copy of my thesis, including any final revisions, as approved by my thesis advisor.

Abstract

In today's transient economy, the demand for new alternative technologies is increasing. Vehicle fuel economy has become the most important phrase in the automotive industry. The ability to achieve optimal fuel economy has many trade-offs. In terms of engine components, this trade-off comes in the form of component reliability. In the past, most engine components were constructed of cast iron. Currently many cast iron components have been replaced by aluminum components to reduce part weight. In parallel with the use of light weight components, higher thermal loadings have been applied to engine components due to the increasing use of fuel saving technologies.

Current aluminum reliability concerns have led to a thermal mechanical fatigue (TMF) investigation of the aluminum casting alloy, AL319-T7. This thesis attempts to model TMF behaviour for an AL319-T7 cylinder head using a combined hardening material model, in which the effects of creep and oxidation have been neglected.

Dedication

I would like to dedicate this thesis to my parents for the countless amounts of support they have given me through all of my academic and non-academic endeavours.

Acknowledgements

This thesis was conducted in a joint double degree program with the University of Windsor and Politecnico di Torino. The research for this thesis was conducted at the Chrysler Automotive Research and Development (A.R.D.C) Centre in Windsor, Ontario, Canada and at Centro Ricerche FIAT in Torino, Italy. I would like to acknowledge the many supporters involved in my thesis, listed below:

Dr. Faouzi Ghrib – University of Windsor – Academic Advisor

Dr. Peter Frise – University of Windsor – Academic Co-Advisor

Dr. Eugenio Brusa – Politecnico di Torino – Academic Advisor

Jim Chen – Chrysler Group LLC – Industrial Advisor

William Resh – Chrysler Group LLC – Industrial Advisor

Raffaele Bonavolonta – FIAT Group – Industrial Advisor

Mario Durando – FIAT Group – Industrial Advisor

Table of Contents

List of Figures

List of Tables

List of Abbreviations, Symbols, and Nomenclature

TMF – Thermal Mechanical Fatigue

FLC – Fatigue Life Calculator

Fortran– Formula Translator

LCF – Low Cycle Fatigue

HCF – High Cycle Fatigue

ASTM – American Society for Testing and Materials

SWT – Smith Watson Topper

MTS – Multi-purpose Testware Software

MPT – Multi-purpose Testware

LLC – Limited Liability Company

FIAT – Fabbrica Italiana Automobili Torino (Italian Automobile Factory Turin)

IP – In-Phase

OP – Out-of-Phase

S-N – Strain Life Diagram

σ – Stress

ε – Strain

$\Delta\sigma$ – Stress Range

$\Delta\varepsilon$ – Strain Range

$\Delta\varepsilon_p$ – Plastic Strain Range

$\Delta\varepsilon_e$ – Elastic Strain Range

E – Young's Modulus

k – Strain Hardening Coefficient

n – Strain Hardening Exponent

k' – Cyclic Strain Hardening Coefficient

n' – Cyclic Strain Hardening Exponent

σ'_f – Fatigue Strength Coefficient

ε'_f – Fatigue Ductility Coefficient

c – Fatigue Ductility Exponent

b – Fatigue Strength Exponent

N_f – Fatigue Life

σ_{max} – Maximum Stress

σ_{min} – Minimum Stress

σ_a – Stress Amplitude

σ_m – Mean Stress

$\varepsilon_{a,q}$ – Equivalent Strain Amplitude

ν – Poisson's Ratio

$\varepsilon_{x,a}$ – Strain Amplitude in x-direction

$\varepsilon_{y.a}$ – Strain Amplitude in y-direction

$\varepsilon_{z,a}$ – Strain Amplitude in z-direction

$\gamma_{ij,a}$ – Direction Shear Strain Amplitude

γ_{xy} – Shear Strain Amplitude in xy Direction

γ_{xz} – Shear Strain Amplitude in xy Direction

γ_{yz} – Shear Strain Amplitude in yz Direction

$\Delta\varepsilon_x$ – Strain Range in x-direction

$\Delta\varepsilon_y$ – Strain Range in y-direction

$\Delta\varepsilon_z$ – Strain Range in z-direction

$\Delta\gamma_{xy}$ – Shear Strain Amplitude in xy Direction

$\Delta\gamma_{xz}$ – Shear Strain Amplitude in xy Direction

$\Delta\gamma_{yz}$ – Shear Strain Amplitude in yz Direction

a – ASME Equivalent Strain Amplitude

$\lambda(T)$ – Temperature Damage Factor

n – Material Exponent (Taira's Model)

C_1 – Material Constant Independent of Temperature

$\lambda(\sigma_a,T)$ – Iso-thermal Temperature Damage Factor

$N(\sigma_a)$ – Fatigue Life at Room Temperature

$N(\sigma_{a,T})$ – Fatigue Life at Elevated Temperature

$\lambda(T_e)$ – Temperature Damage Factor for Equivalent Temperature

α – Material Constant

c – Material Constant

T – Temperature

w – Energy Released for One Fatigue Cycle

W – Accumulated Energy Released

i - Cycle Number

$\Delta\sigma_i$ – Stress Range for i^{th} Cycle

$\Delta\varepsilon_{pi}$ – Plastic Strain Range for i^{th} Cycle

C – Initial Material Strength Constant

λ – Material Constant

Chapter 1 Introduction

1.1 Research Motivation

The primary motivation for this thesis is that vehicle fuel economy must increase and tail pipe emissions must be reduced. As stated by the National Highway Traffic Safety Administration (NHTSA), the corporate average fuel economy (CAFE) by the year 2025 must be 54.5 mpg (4.3 L/100km) [12]. To meet this demand, vehicle components must be lighter while still maintaining or enhancing durability. Components, such as a cylinder head, are subject to higher temperatures due to advances in fuel-saving technologies. This means that durability becomes a very important concern because engine components will experience higher thermal loadings. Chrysler and FIAT are interested in the investigation of thermal mechanical fatigue (TMF) characteristics of the aluminum alloy, AL319-T7. To ensure that these new CAFE standards can be met and that part durability is not compromised, Chrysler and FIAT have asked for a procedure/tool to be developed using the most economical means necessary to predict part durability (fatigue life) for AL319-T7.

1.2 Advantages of Aluminum Components

The application of aluminum for casting cylinder heads has greatly increased over approximately the last 20 years. This trend is expected to continue to grow into the future as the need for lighter components increases. Table 1.1illustrates the increasingly popular trend of using aluminum as a cylinder head casting material.

Table 1.1: Evolution of aluminum as a cylinder head material over approximately the past two decades. [20]

% of Aluminum Cylinder Heads			
	1994	**2000**	**2005**
Passenger Cars	78%	85%	95%
Light Trucks	20%	40%	60%

There are considerable advantages to substituting aluminum for the traditional cast iron material. Benefits associated with using aluminum as a casting material include:

- Weight reduction: V8 Engine Block – Heavy, 150 lbs (Cast Iron) vs. Light, 68lbs (Aluminum) [20].
- Casting of very complex shapes can be done using aluminum [20].
- Increased thermal conductivity in comparison to cast iron [20].

1.3 Types of Mechanical and Thermal Loadings

Stresses and strains may develop when a material is subjected to mechanical and/or thermal loading. There are two types of mechanical loading that can take place, monotonic and cyclic. A thermal loading can also occur when there is a temperature change.

The first and simplest type of mechanical loading that material can experience is monotonic loading. This type of loading occurs when a component is loaded under conditions producing non-reversed stresses. The second type of mechanical loading that a material may be subjected to is cyclical loading. Cyclical loading involves both tensile and compressive loading until failure. Another state of loading that may develop stresses and strains is thermal loading; in response to thermal expansion or contraction, the material will experience either tensile or compressive loading. The afore mentioned types of mechanical loading (monotonic and cyclic loading) can occur in an iso-thermal (constant temperature) state. The condition in which both mechanical and thermal loads occur at the same time is referred to as Thermo-Mechanical Fatigue (TMF). TMF is the most critical type of loading when component durability is a concern. A material subjected to TMF may experience a shorter fatigue life when compared to a material experiencing iso-thermal loading. TMF loading occurs in two different manners, In-Phase (IP) or Out-of-Phase

(OP). IP loading happens when thermal expansion occurs in conjunction with tensile loading. OP loading is a state in which the thermal loading acts in the opposite direction of the mechanical loading.

1.4 Material Model Development

Developing the constitutive laws that a material is actually subjected to is important when simulation accuracy is a priority. The choice of material model is of great importance when replicating material properties in a Computer Aided Engineering (CAE) program. The material studied in this thesis was subjected to plastic deformations and high temperatures, thus only elasto-viscoplastic material models were used. The different types of elasto-viscoplastic hardening material models that can be considered are:

1. Linear Kinematic
2. Non-Linear Kinematic
3. Non-Linear Kinematic and Isotropic Hardening

The numerical order of the above list represents the increasing complexity of the material model, with 3 being the most complex model. As the complexity of the material model increases, so does its accuracy. The time needed to develop the material model also increases, however, because more material parameters are required. Figure 1.1provides a visual representation of how the accuracy and complexity of material models relate to development time.

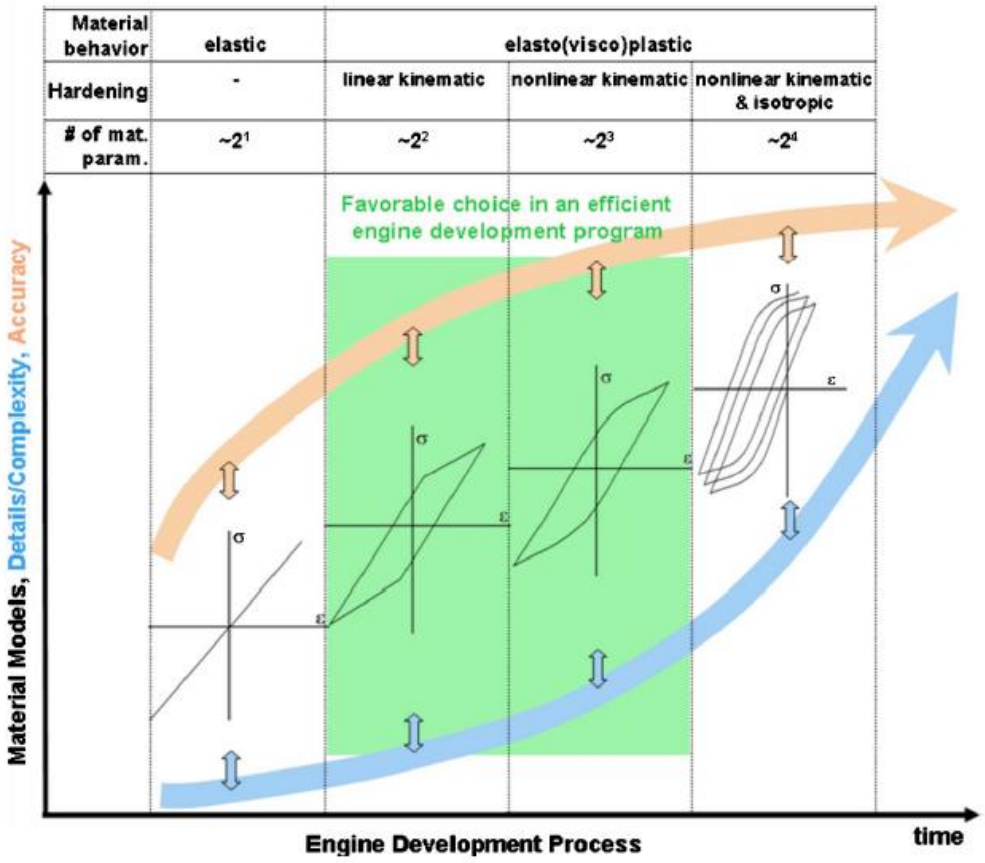

Figure 1.1: Representation of the relationship between complexity, accuracy, and time consumption for different types of material models. [25]

1.5 Fatigue Life Prediction Damage Models

1.5.1 Strain based Damage Models

Researchers in the fatigue field have studied several fatigue life prediction damage models. Each damage model has its own unique characteristics that differentiate them and possibly better suit them for certain applications. Most damage models were developed using a strain based approach. In this thesis the strain based damage models studied are listed below:

1. Basquin-Manson-Coffin
2. Smith-Watson-Topper (SWT)
3. Morrow

4. von Mises (Multi-axial)
5. ASME (Multi-axial)

1.5.2 Energy based Damage Models

The energy based damage model used in this work is the Skelton model. This model predicts the fatigue life based on the total energy released when subjected to a loading condition. The total energy released is represented by the area of the hysteresis loop.

1.5.3 Thermo-Mechanical Fatigue Damage Model

The TMF damage model studied is the Taira's model. This unique approach was used to capture the effects that temperature may have on material subjected to cyclical loading. This model can be applied to both iso-thermal and TMF types of loading.

1.6 Comparable Thermo Mechanical Fatigue Research

Due to the commercial needs previously described, the importance of accurate TMF knowledge has grown significantly. Available TMF research findings usually pertain to experimental testing and the associated physical phenomena; however, a more recent trend is to accurately model TMF using CAE to simulate the effects of TMF. The simulated TMF results can be used to predict and compare fatigue life using different damage models.

In the TMF field, research has been reported, which is similar to that presented in this thesis. Nevertheless, these studies differ from one another. Current TMF durability research focuses on modelling material properties with the effects of creep or oxidation in combination with a non-linear kinematic hardening model. In the research of Grieb [26], TMF life predictions were investigated for the valve bridge of a cylinder head using several different types of materials. FEA simulations were conducted in ABAQUS on a specimen similar to a cylinder head valve

bridge. However, the type of material model used was not specified. Using the FEA results, values of fatigue life were predicted and then compared to experimental results.

Delprete [16, 17] studied the effects of multi-axial TMF loading using a damage assessment for an exhaust manifold. FEA simulations were conducted for an exhaust manifold using a combined hardening approach that included the effects of oxidation.

A study examining the TMF of a cylinder head was conducted by Trampert, Taner Gocmez, and Stefan Pischinger [27]. In this research, different types of cast iron cylinder head materials were investigated. The type of material model used in this case was a non-linear kinematic hardening model.

1.7 Research Objectives of this Thesis

This thesis was conducted in partnership with multiple affiliates, which include Chrysler Group LLC., FIAT, University of Windsor, Politecnico di Torino, and the University of Michigan.

The primary purpose of this research is to investigate the accuracy of TMF life predictions when modeling the material with only a combined hardening model. A combined hardening model is comprised of both kinematic and isotropic hardening. This is the first attempt in the TMF research field to accurately model a material experiencing TMF loading using only the combined hardening model while neglecting the effects of oxidation and creep. This approach will significantly reduce the complexity of the material model, which will lead to financial and temporal benefits. Figure 1.2 outlines the process used to complete the research in this thesis:

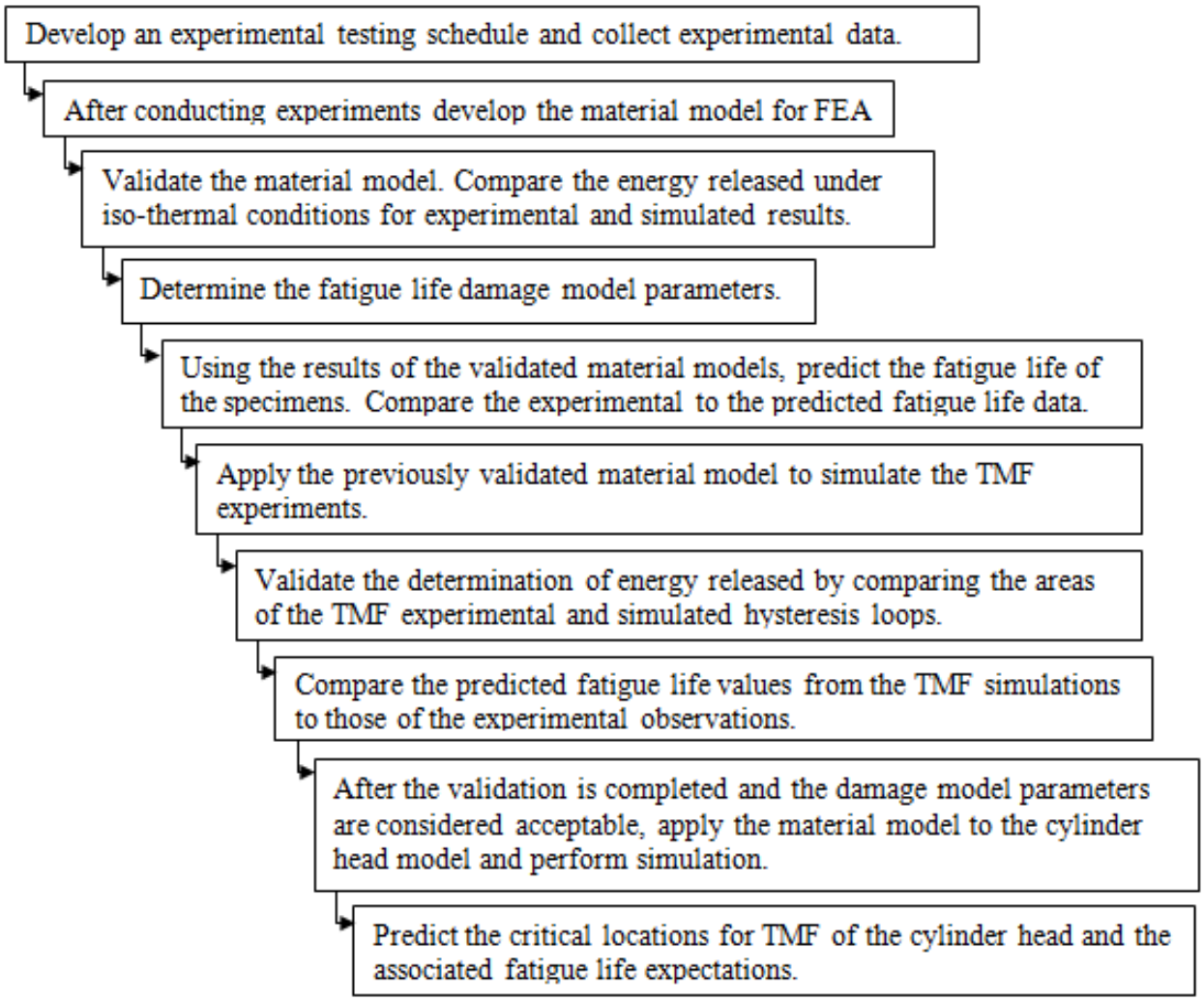

Figure 1.2: Flowchart of the process used to complete the research in this thesis

1.8 Thesis Organization

Chapter 2 contains a literature review that outlines several fatigue phenomena and various damage models used to predict fatigue life. The experimental testing methods are described in Chapter 3, which includes the processes used to develop the monotonic and cyclic fatigue material models. The monotonic, iso-thermal, and TMF specimen model simulations and the corresponding validation procedures are also described and explained in Chapter 3. Chapter 3 concludes by outlining procedures for which the calibration of the fatigue damage model parameters. The fatigue life prediction results are presented in Chapter 4 for both the material

test specimens and the cylinder head. A discussion of the experiments, material model development, damage model parameters, and fatigue life predictions is provided in Chapter 5. Chapter 6 includes this study's final conclusions and future recommendations for the continuation of this research.

Chapter 2 Literature Review

2.1 Definition of Thermo-Mechanical Fatigue (TMF)

TMF is caused by the combination of thermal and mechanical loading in which stress, strain, and temperature vary with time [21]. Loading of this type can be much more damaging than loading under iso-thermal conditions. Iso-thermal loading is a condition in which temperature remains constant throughout the mechanical loading cycle. The conditions that promote TMF are usually found during the start-up and shut-down cycles of high temperature components and equipment [21]. There are two types of conditions when TMF loading transpires: In-phase (IP) and Out-of-phase (OP) conditions (Figure 2.1).

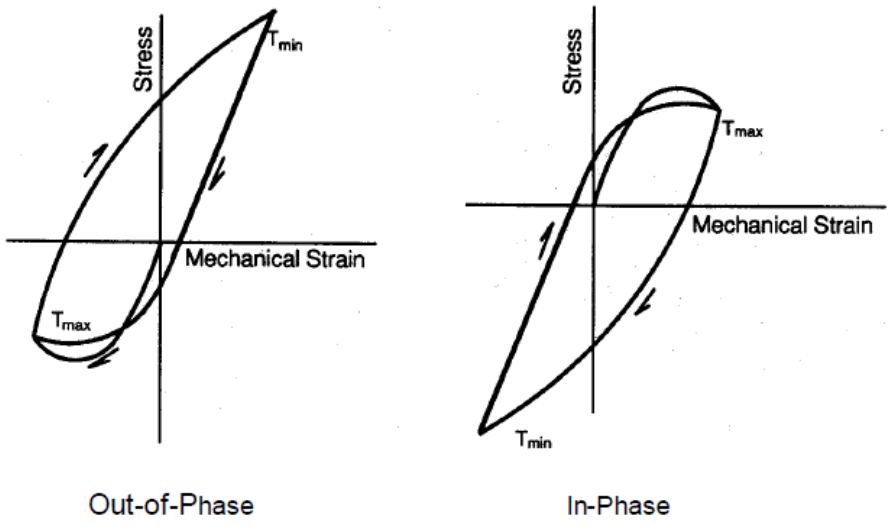

Figure 2.1: TMF loading and temperature phasing. Out-of-Phase loading is when the mechanical loading and the temperature loading occur in separate directions (material is heated and loaded under compression). In-Phase loading is when both the mechanical and temperature loading is applied in the same direction (material is heated and loaded under tension). [21]

2.2 Fatigue Phenomena

2.2.1 Cyclic Fatigue Background

Many different phenomena contribute to the effects of cyclic fatigue; including: cyclic hardening and softening stabilization, plastic shakedown, ratchetting, and mean stress relaxation. When material is subjected to continuous cyclic loading a hysteresis loop will generate. This hysteresis

loop represents a cyclic stress-strain (σ-ε) curve in which the material experiences both elastic and plastic deformations. The hysteresis loop consists of 2 curves, one representing compressive loading and the other representing tensile loading.

The hysteresis loop is a critical measure for fatigue and can be used to assess many associated parameters. The strain range (Δε) is the width of the hysteresis loop and the height of the hysteresis loop is the stress range (Δσ).The measure of plastic deformation or energy released by the material is found by calculating the area inside the hysteresis loop.

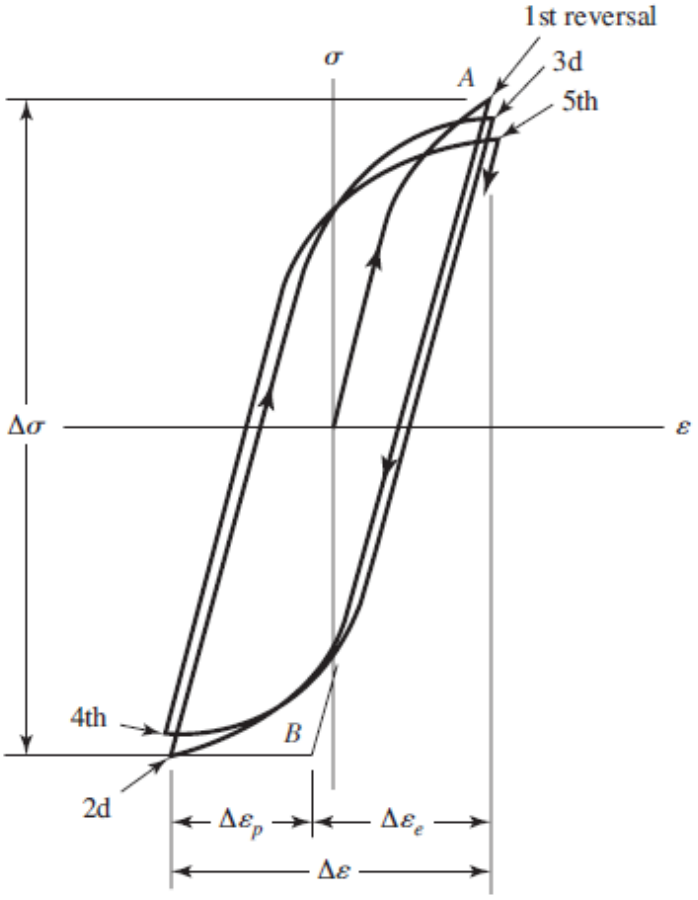

Figure 2.2: True Stress - True Strain hysteresis loop. This figure shows a material that is subjected to the cyclic softening phenomenon. Cyclic softening occurs because the maximum stress (σ_{max}) falls within each loop. [4]

Three conditions can lead to fatigue that is associated with a hysteresis loop: cyclic softening, cyclic hardening, and cyclically stable conditions. Figure 2.2 illustrates a typical hysteresis loop for a material undergoing cyclic softening. Cyclic softening occurs when there is a physical change to the material structure due to loading that makes the material less resistant to deformations, causing the material to soften. Cyclic hardening occurs when the density of the material is increased. A material is cyclically stable when it is continually subjected to cyclic loading, and no longer exhibits the hardening or softening phenomena.

The ratio of ultimate strength to yield strength can be used to predict if a material will undergo cyclic hardening or softening. A ratio greater than 1.4 is considered to lead to cyclic hardening [23] and a ratio less than 1.2 to lead to be cyclic softening [23]. An alternative method to use is the monotonic strain hardening exponent (n) to predict cyclic hardening or softening. If the monotonic strain hardening exponent is greater than 0.2, the material will experience cyclic hardening [24], and an exponent (n) that is less than 0.1 will show cyclic softening [24].

2.2.2 Cyclic Hardening and Softening Stabilization

A material subjected to a uniaxial cyclic loading deformation is characterized by a cyclic σ-ε curve (hysteresis loop). Figure 2.3 displays the various types of cyclic loading that a material may be subjected to in a uniaxial direction. Strain-controlled loading (Figure 2.3*b*) is the type of cyclic loading that was applied during experimental testing for the research presented in this thesis.

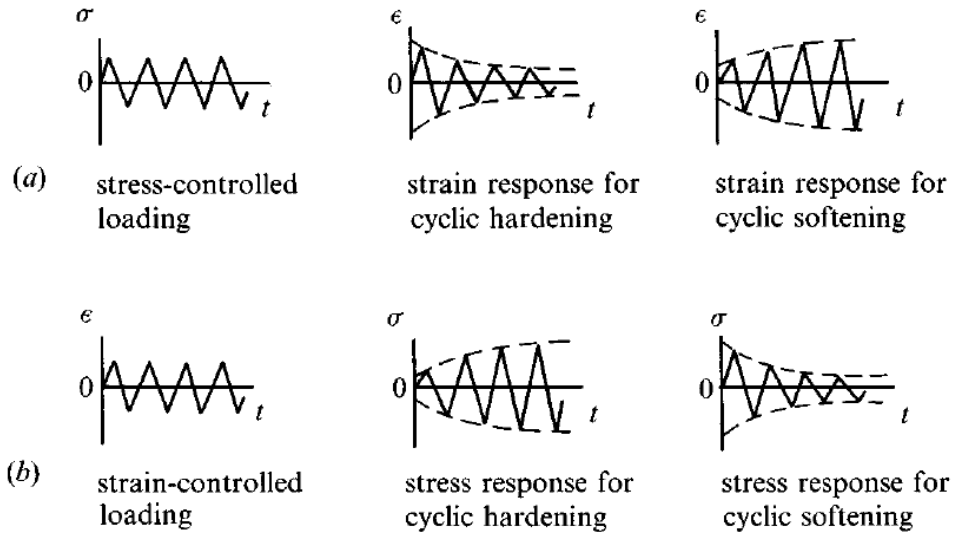

Figure 2.3: Transient phenomena associated with different types of cyclic loading. [1]

2.2.3 Plastic Shakedown

Figure 2.4 illustrates Plastic Shakedown, a state of deformation due to a closed cycle of alternating plasticity that occurs without any accumulation of plastic strains [4]. When the "stabilized plastic shakedown" region has been established as shown in Figure 2.4, the plastic shakedown period terminates. At this point, the increase in stress indicates that cyclic hardening is taking place.

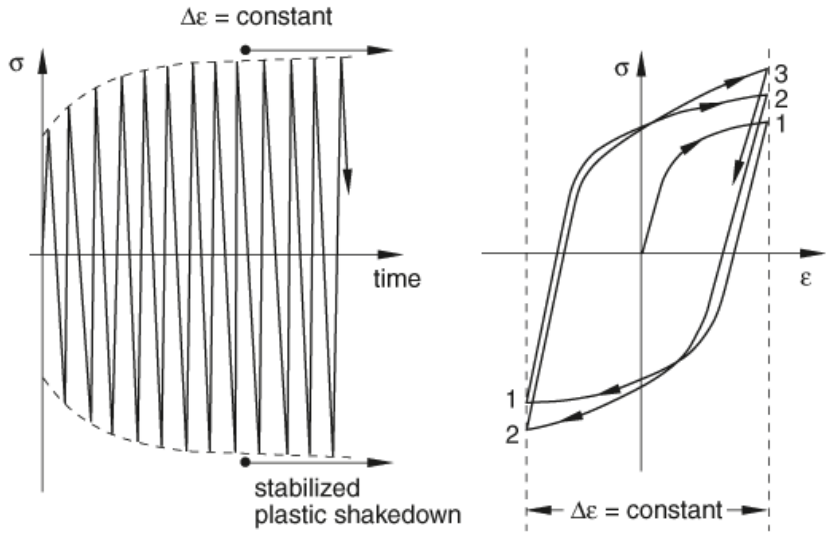

Figure 2.4: Plastic Shakedown. This phenomenon usually occurs during the initial loading state and is concluded once a state of stabilization is reached. [11]

2.2.4 Ratchetting or Cyclic Creep

When a material is subjected to repeated cyclic stresses of fixed amplitudes, ratchetting or cyclic creep can occur. If the plastic deformation in the loading cycle is not opposed by an equal and opposite plastic deformation in the unloading cycle, ratchetting effects will be seen. Figure 2.5*(a)* shows the process of ratchetting for a fatigue softened material that is subjected to repeated cyclic loading. In this case ratcheting occurs in the direction of increasing tensile strains (rightward movement). Figure 2.5 *(b)* shows ratcheting in a material experiencing repeated compressive mean stress cycles (leftward movement).

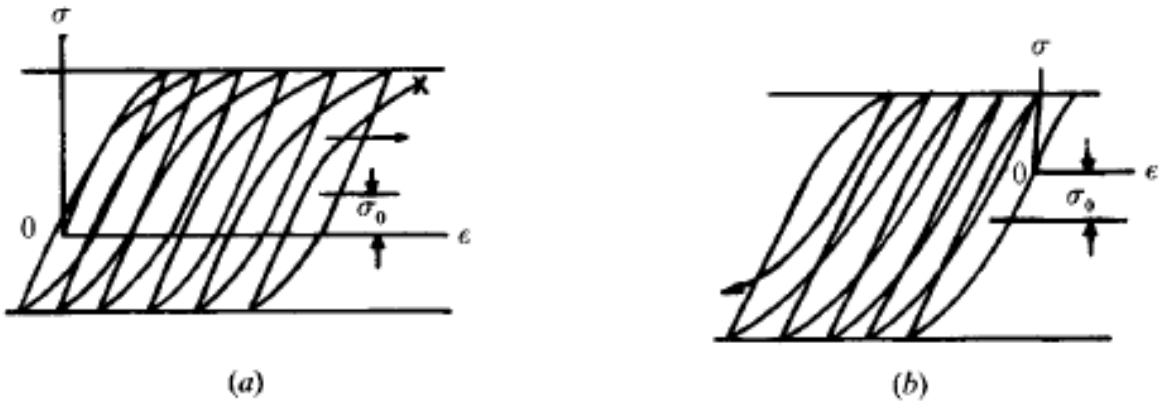

Figure 2.5: Ratchetting or Cyclic Creep (a) Tensile Mean stress (specimen is initially loaded under tension) (b) Compressive mean stress (specimen is initially loaded under compression). [4]

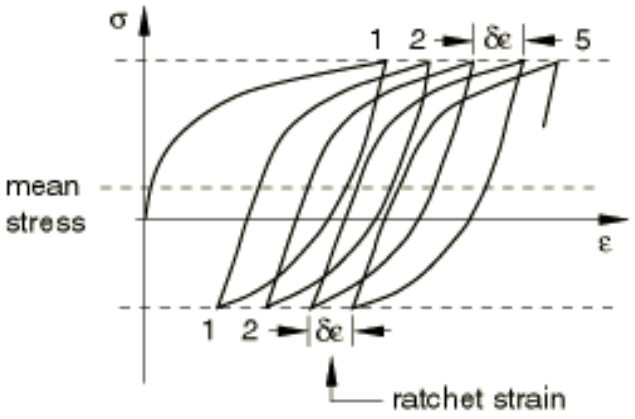

Figure 2.6: Rachetting or Cyclic Creep for non-zero mean stress and the effect on the ratchet strain range. [11]

Figure 2.6 illustrates the mean stress between loading and unloading cycles, and the strain due to ratchetting. This is the strain range found between each cycle's maximum and minimum stress.

2.2.5 Mean Stress Relaxation

Mean Stress Relaxation is a process in which the mean stress experienced by the material eventually equals zero. The case illustrated in Figure 2.7 is a material that is subjected to cyclic softening. Figure 2.7 (a) shows the cyclic fatigue softening process occurring when the strain is at a maximum value of *A*; after this point, the strain begins to decrease until stabilizing at *C*.

Figure 2.7 (*b*) shows the phenomenon of mean stress relaxation taking place as the number of cycles increases.

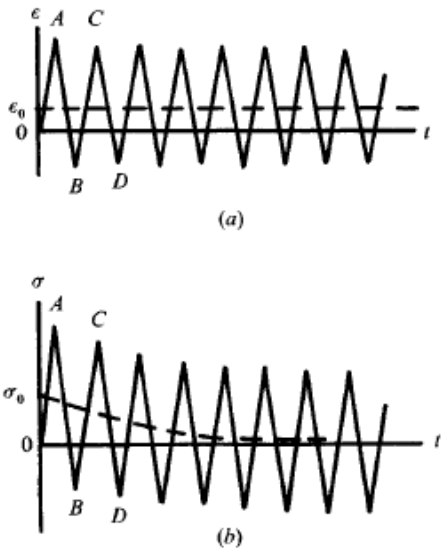

Figure 2.7: a) Cyclic Fatigue softening process due to an initial strain. b) Mean stress relaxation for a cyclically softened material subjected to strain-controlled fatigue. [4]

Mean Stress Relaxation can also occur in materials subjected to cyclic hardening; however, the effects shown in Figure 2.7 would be slightly altered. In this case, the value at *A* would be less than *C* and the value at *B* would be greater than *D in* Figure 2.7 *(a)* and *(b)*, respectively. During cyclic hardening conditions, the material yields more for loading under tension than it does for loading under compression; thus, the curves will shift downward.

2.2.6 Stress or Strain Approximations

Determining the strain hardening exponent (*n*) and the strength hardening coefficient (*k*) can be extremely beneficial. The variables *n* and *k* enable the approximation of a σ-ε for a specified strain rate over an entire temperature range. Variables *n* and *k* can be applied to the Ramberg-Osgood relation to determine the σ-ε parameters for any operating temperature. Equations 2.1

and 2.2 represent the constitutive law known as the Ramberg-Osgood relation for monotonic and cyclic uniaxial loading of a ductile material, respectively.

$$\varepsilon = \frac{\sigma}{E} + \left(\frac{\sigma}{k}\right)^{\frac{1}{n}} \qquad \textit{Equation 2.1}$$

$$\frac{\Delta\varepsilon}{2} = \frac{\Delta\sigma}{2E} + \left(\frac{\Delta\sigma}{2k'}\right)^{\frac{1}{n'}} \qquad \textit{Equation 2.2}$$

The variables identified in Equations 2.1 and 2.2 are defined as follows; true strain (ε), true stress (σ), modulus of elasticity (*E*), monotonic strain hardening exponent (*n*), monotonic strength hardening coefficient (*k*), true strain range (Δε), true stress range (Δσ), cyclic strain hardening exponent (*n'*), and the cyclic strength hardening coefficient (*k'*). In general, well-annealed, polycrystalline metals of high purity exhibit cyclic hardening due to dislocation multiplication, as evidenced by an increase in the stress amplitude over repeated fatigue cycles (at a fixed strain amplitude); work-hardened materials undergo strain softening under cyclic loading [1].

2.3 Uniaxial and Multiaxial Fatigue Damage Models

Uniaxial damage models can be used to predict the development of a crack on the surface of a material. The low-cycle fatigue life of materials is estimated with uniaxial damage models that are properly calibrated in accordance with experimental data. These models may incorporate damage evolution, crack nucleation, and the growth of cracks into a single function, which reflects the understanding that the fatigue life of a component is the number of cycles needed to induce initial damage, such as the development of a crack on the surface of a component that may then propagate to induce final part failure.

A material can be subjected to two different types of fatigue: high cycle fatigue (HCF) and low cycle fatigue (LCF). HCF appears in materials that experience low stress or strain amplitudes and that are designed for operation primarily in the elastic region. Components experiencing HCF are generally designed for very long part life, of more than 10^4 cycles. When high stress or strain amplitudes are experienced primarily in the plastic region during operation, LCF will be experienced. LCF generally implies fatigue life of less than 10^4 cycles. Figure 2.8 illustrates the difference between HCF and LCF when viewed as a stress amplitude – life (S-N) diagram.

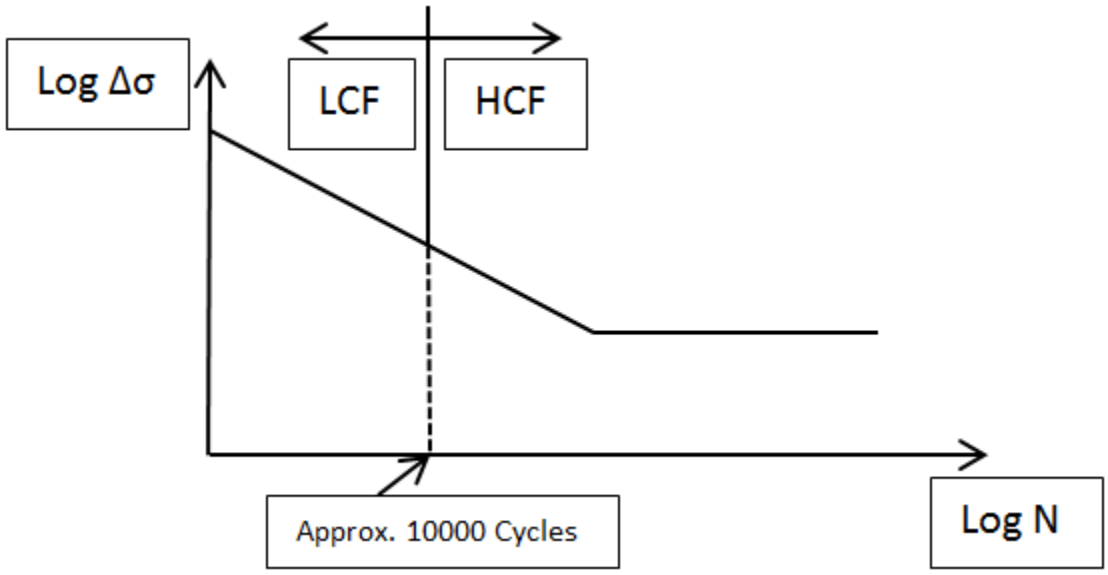

Figure 2.8: Low-cycle fatigue S-N curve. Cut-off usually occurs at approximately 10,000 cycles. Less than 10,000 cycles is considered to be LCF and greater than 10,000 cycles is considered to be HCF. [22]

In order to investigate and test the validity of any damage model, experiments must be performed on test specimens. These experiments can be performed in various ways, but must follow the ASTM E466-E468 standards, and include: plane bending, rotating bending, uniaxial tension and compression, and strictly tension tests. Regardless of the experimental procedure used, the tests should be applied to smooth hourglass shaped test specimens, and performed using either a strain or a stress based approach. In a strain based approach, the strain range is fixed, but in a stress

based approach, the stress range is fixed. The experiments presented in this thesis were conducted using a fixed strain range until the specimen failed.

Several damage models have been proposed by researchers using different approaches to the determination of fatigue life. The damage models investigated in this thesis are energy based or empirically based models related to strain partitioning. The Skelton model uses the energy based approach, and the Basquin-Manson-Coffin model, Smith-Watson-Topper (SWT) model, Morrow model, and Taira's model use an empirical strain based approach. The von Mises and ASME models are examples of multiaxial damage models, which are also empirically strain based approaches. Taira's model is a TMF life prediction model.

2.3.1 Strain Based Approaches

The Basquin-Manson-Coffin Model

This model is also known as a strain-life method, which means that the estimation of fatigue life is based on the total strain amplitude. This approach, as is the case for all damage models, provides only an approximation of the fatigue life of a material because the method is based on several compounded assumptions. In particular, this damage model is based on two equations: the Manson-Coffin and Basquin equations. The Manson-Coffin equation is the plastic strain and the Basquin equation employs the elastic strain, which expresses the fatigue life. Equation 2.3 shows the Manson-Coffin relationship for plastic strain [1].

$$\frac{\Delta\varepsilon_p}{2} = \varepsilon'_f \left(2N_f\right)^c \qquad \textit{Equation 2.3}$$

Here, $\frac{\Delta\varepsilon_p}{2}$ is the plastic strain amplitude; this can be obtained from a stabilized σ-ε hysteresis loop. ε'_f is the fatigue ductility coefficient and represents the true strain at the time of fracture. The fatigue ductility exponent, *c*, can be identified by the slope of the plastic strain line.

The Basquin equation for elastic strain [1] is presented in Equation 2.4.

$$\frac{\Delta\varepsilon_e}{2} = \frac{\sigma'_f}{E}\left(2N_f\right)^b \qquad \textit{Equation 2.4}$$

In this equation, $\frac{\Delta\varepsilon_e}{2}$ is the elastic strain amplitude range, σ'_f is the fatigue strength coefficient and is the true stress corresponding to the point of fracture. The fatigue strength exponent, *b*, is the slope of the elastic strain line, and E is the modulus of elasticity. The remaining variable is the fatigue life (N_f). Figure 2.9 illustrates the association of these variables with the relationship between fatigue life and strain amplitude. The variables, ε'_f and σ'_f, are obtained by finding the respective intersections of the plastic and elastic strain curves with the strain amplitude axis. The point at which the elastic strain curve intersects with the strain amplitude axis is $\frac{\sigma'_f}{E}$, and thus, σ'_f can be obtained from this relationship.

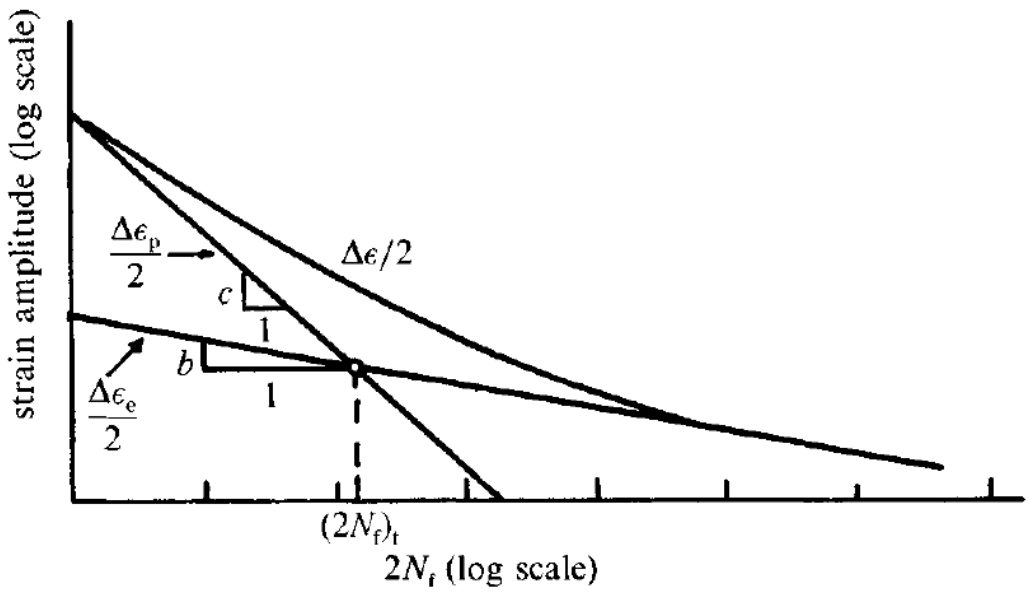

Figure 2.9: Log-Log plot of the relation of fatigue life with strain amplitude. [1]

Determining the Fatigue Strength Coefficient (b) and the Fatigue Ductility Exponent (c)

The variables, *b* and *c*, can be determined from experimental data by calculating the slopes of the plastic and elastic curves, respectively. However, Morrow [5] has developed a function for describing this relationship. Equation 2.5 and Equation 2.6 show the relationship between the fatigue strength coefficient *b*, the fatigue ductility exponent *c*, and the cyclic hardening exponent, *n'*.

$$b = \frac{-n'}{1+5n'} \qquad \textit{Equation 2.5}$$

$$c = \frac{-1}{1+5n'} \qquad \textit{Equation2.6}$$

These relationships can then be used to estimate the fatigue strength coefficient (*b*) and the fatigue ductility exponent (*c*) as long as the cyclic hardening exponent (*n'*) is known.

The elastic and plastic strain curves represent high-cycle and low-cycle fatigue respectively. By summing the two together, the total strain amplitude can be obtained, which represents both types of fatigue. Equation 2.7 shows the total strain amplitude relationship [1].

$$\frac{\Delta\varepsilon}{2} = \frac{\Delta\varepsilon_e}{2} + \frac{\Delta\varepsilon_p}{2} \qquad \textit{Equation 2.7}$$

Figure 2.10 shows how the variables for Equation 2.7 can be assessed from a stabilized hysteresis loop.

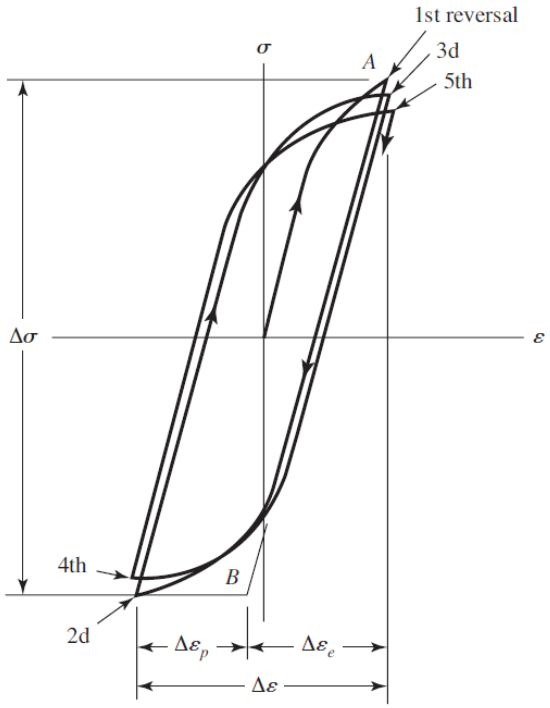

Figure 2.10: Representation of typical variables of a hysteresis loop. This figure displays how the Δε is comprised of the $\Delta\varepsilon_p$ and $\Delta\varepsilon_e$ and how to evaluate it from a hysteresis loop. [4]

Thus, by combining the Manson-Coffin and Basquin equations, the Basquin-Manson-Coffin function [1] shown in Equation 2.8 is obtained. This equation establishes the basis of the strain life damage model approach.

$$\frac{\Delta\varepsilon}{2} = \frac{\sigma'_f}{E}\left(2N_f\right)^b + \varepsilon'_f\left(2N_f\right)^c \qquad \textit{Equation2.8}$$

Smith Watson Topper (SWT) Model

The SWT model was proposed by Smith et al [9]. The relationship includes both the cyclic strain amplitude ($\Delta\varepsilon/2$) and the maximum stress (σ_{max}). This damage model produces excellent results for a uniaxial loading situation in which a correction for the mean stress is needed. This damage model is also very good for approximating the fatigue life of aluminum alloys, and is also well suited for situations in which failure occurs due to tensile loading [9]. Equation 2.9 shows the relationship between the variables in the SWT model.

$$\sigma_{\max}\left(\frac{\Delta\varepsilon}{2}\right) = \frac{\left(\sigma'_f\right)^2}{E}\left(2N_f\right)^{2b} + \sigma'_f\varepsilon'_f\left(2N_f\right)^{b+c} \qquad \textit{Equation 2.9}$$

The term, σ_{max} is the same as the stress amplitude (σ_a), and thus, this variable can be determined using Equation 2.11 (below). All of the other parameters are the same as those included in the Basquin-Manson-Coffin damage model.

Morrow Damage Model

This method is also a modification of the Basquin-Manson-Coffin model [1], intended to account for the effects of mean stress (σ_m) offsets. Figure 2.11 shows a constant stress range test for an experiment in which the mean stress was not zero.

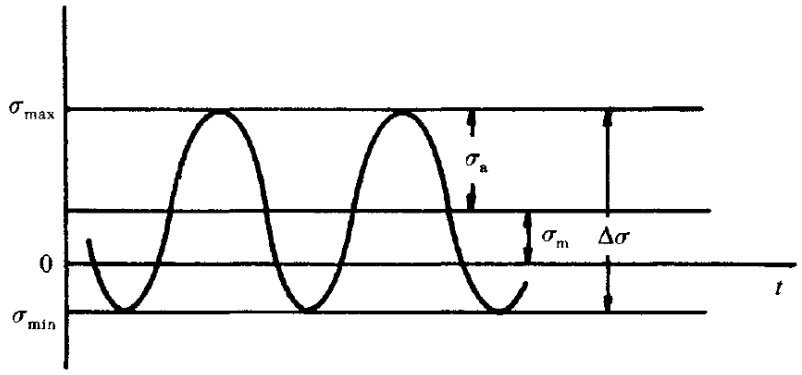

Figure 2.11: Effect of mean stress for a constant stress range experiment. [1]

The parameters in Figure 2.11 can be expressed by Equations 2.10, 2.11, and 2.12.

$$\Delta\sigma = \sigma_{max} - \sigma_{min} \qquad \textit{Equation 2.10}$$

$$\sigma_a = \frac{\sigma_{max} - \sigma_{min}}{2} \qquad \textit{Equation 2.11}$$

$$\sigma_m = \frac{\sigma_{max} + \sigma_{min}}{2} \qquad \textit{Equation 2.12}$$

In order to predict outcomes using the relationship between stress range and fatigue life under the influence of non-zero mean stress, the Basquin model cannot be directly applied. Thus, Morrow [1] modified the original Basquin equation to account for mean stress effects as shown in Equation 2.13.

$$\sigma_a = \left(\sigma'_f - \sigma_m\right)\left(2N_f\right)^b \qquad \textit{Equation 2.13}$$

Consequently, the function derived from the Morrow [1] equation is expressed as shown in Equation 2.14.

$$\frac{\Delta\varepsilon}{2} = \frac{\left(\sigma'_f - \sigma_m\right)}{E}\left(2N_f\right)^b + \varepsilon'_f\left(2N_f\right)^c \qquad \textit{Equation 2.14}$$

von Mises Damage Model

The von Mises damage model (Equation 2.15) [16] is considered to be a strain based approach, which can be used to relate uniaxial fatigue to multi-axial fatigue. It does this by using the

equivalent strain amplitude, which is derived from the normal ($\varepsilon_{i,a}$) and shear($\gamma_{ij,a}$) strain amplitudes in each direction, along with the Poisson's ratio(v); these measures can be used to determine an equivalent strain amplitude. ($\varepsilon_{a,eq}$) is shown in Equation 2.15.

$$\varepsilon_{a,eq} = \frac{1}{(1+v)\sqrt{2}}\sqrt{\left[\left(\varepsilon_{x,a}-\varepsilon_{y,a}\right)^2+\left(\varepsilon_{x,a}-\varepsilon_{z,a}\right)^2+\left(\varepsilon_{y,a}-\varepsilon_{z,a}\right)^2+\frac{3}{2}\left(\gamma_{xy}^2+\gamma_{xz}^2+\gamma_{yz}^2\right)\right]} \quad \textit{Equation 2.15}$$

The approximation of the equivalent strain range can be applied to the uniaxial Basquin-Manson-Coffin damage model to predict the fatigue life.

ASME Damage Model

The ASME damage model was introduced in 1988 as an ASME Boiler and Pressure Vessel Code Procedure [17,18]. This method is based on the von Mises model. The equivalent strain amplitude is determined on the basis of three dimensional strain ranges. This strain range is the difference between two equivalent points on one hysteresis loop at two different times. Each point represents a loaded and an unloaded condition. Using the relationships described in Equation 2.16 and Equation 2.17, the equivalent strain amplitude can be calculated and applied to the Basquin-Manson-Coffin curves to predict the fatigue life.

$$a = \sqrt{\left[\left(\Delta\varepsilon_x-\Delta\varepsilon_y\right)^2+\left(\Delta\varepsilon_x-\Delta\varepsilon_z\right)^2+\left(\Delta\varepsilon_y-\Delta\varepsilon_z\right)^2+6\left(\Delta\gamma_{xy}^2+\Delta\gamma_{xz}^2+\Delta\gamma_{yz}^2\right)\right]} \quad \textit{Equation 2.16}$$

$$\varepsilon_{a,eq} = \frac{1}{2}\max\left(\frac{\sqrt{2}}{3}\cdot a\right) \qquad \textit{Equation 2.17}$$

Taira's Damage Model

Taira's model is a strain based approach that uses a function proposed by Manson and Coffin that has been modified to include a damage factor related to temperature [14,19]. This relationship described in Equation 2.18, and includes the following parameters [14,19]:

- Temperature Damage Factor ($\lambda(T)$)

- Plastic Strain Range ($\Delta\varepsilon_p$)

- Material Exponent (*n*), which is 2 in most cases

- Material Constant Independent of Temperature (C_1)

- Fatigue Life (N_f)

$$\lambda(T)\cdot\left(\Delta\varepsilon_p\right)^n \cdot N_f = C_1 \qquad \textit{Equation 2.18}$$

The iso-thermal damage factor can easily be determined by relating the fatigue life at room temperature to the fatigue life at an elevated temperature. The temperature damage factor relationship shown in Equation 2.19 is applicable to isothermal conditions only [14, 19]. Here, $N(\sigma_a)$ is the fatigue life at room temperature and $N(\sigma_a,T)$ is the fatigue life at an elevated temperature condition.

$$\lambda(\sigma_a,T) = \frac{N(\sigma_a)}{N(\sigma_a,T)} \qquad \textit{Equation 2.19}$$

If TMF conditions are experienced, then either Equation 2.20 or Equation 2.21 should be applied [14, 19].

$$(i) \qquad \lambda(T_e) = \frac{1}{T_2 - T_1}\int_{T_1}^{T_2} \lambda(T)dT \qquad \textit{Equation 2.20}$$

$$(ii) \qquad \lambda(T_e) = \frac{1}{T_2^{'} - T_1}\int_{T_1}^{T_2^{'}} \lambda(T)dT + \frac{\lambda(T_2)}{2} \qquad \textit{Equation 2.21}$$

If the equivalent temperature is close to the mean temperature (*i*) $T_e \cong T_m = \frac{T_1 + T_2}{2}$ then Equation 2.20 is applied. If the equivalent temperature $T_e \cong T_2$ is close to the upper limit (*ii*) then Equation 2.21 is implemented. In Equation 2.21, $T_2^{'}$ is the threshold temperature of the material. Figure

2.12 shows that the damage factor is an approximation of the area found under the curve, which relates the isothermal damage factor and the equivalent temperature.

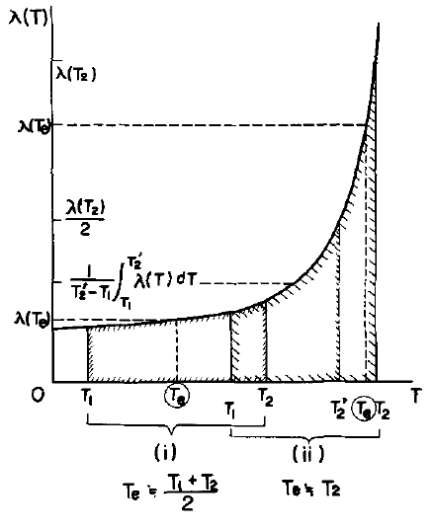

Figure 2.12: Damage factor relationship with equivalent temperatures. The damage factor is an approximation of the area found under the curve which relates the isothermal damage factor and the equivalent temperature. [14, 19]

To determine the parameter C_1, Equation 2.22 and Equation 2.23 are solved by means of substitution. In Equation 2.22, α is equal to 0.5 in most cases. C is obtained from Equation 2.22, using values of $\Delta\varepsilon_p$ and N_f obtained from experimental data. Using the calculated value of C, Equation 2.23 is used to solve for C_1.

$$\Delta\varepsilon_p \cdot N_f^{\alpha} = C \qquad \textit{Equation 2.22}$$

$$C_1 = C^2 \cdot \lambda(T) \qquad \textit{Equation 2.23}$$

2.3.2 Energy Based Approach

Skelton Damage Model

The Skelton model is an energy based approach, which accounts for both the energy released by one cycle, and the accumulated energy release. The amount of energy released is obtained by determining the area contained within a stabilized cycle of a hysteresis loop. The estimate of dissipated energy can ultimately be used to determine the number of cycles until the

development of crack formation as well as crack propagation. However, in order to determine crack propagation, the values of many variables are needed, requiring additional experimental testing. The approach discussed below only pertains to crack formation, and is not applicable to crack propagation.

An approach proposed by Skelton [3] to determine the enclosed area for a one cycle hysteresis loop can be found in Equation 2.24.

$$w = \frac{\Delta\sigma\Delta\varepsilon_p}{1+n'} \qquad \textit{Equation 2.24}$$

The value of *w* represents the amount of energy that is released for one cycle per unit volume. $\Delta\sigma$ and $\Delta\varepsilon_p$ are the total stress and plastic strain ranges of the stabilized hysteresis loop, respectively.

Skelton [7] also developed a method in which the accumulated amount of energy released can be approximated. This means that the energy for each cycle is added together beginning from the first cycle until *N* cycles. Equation 2.25 describes the accumulated energy dissipation approximation.

$$W = \sum_{i=1}^{N} \frac{\Delta\sigma_i\Delta\varepsilon_{p,i}}{1+n'} \qquad \textit{Equation 2.25}$$

Here, $\Delta\sigma_i$ and $\Delta\varepsilon_{p,i}$ represent the total stress range and the plastic strain range, respectively, for the corresponding cycle.

The work of Skelton established that energy accumulation to the critical value of failure is nearly always constant [3,7], enabling the summation of the $\Delta\varepsilon_{p,i}$ to be removed from the original equation and replaced with the value for $\Delta\varepsilon_p$ derived from a stabilized loop. Equations 2.24 and 2.25 are combined in order to determine the accumulated energy dissipation at a critical value.

The energy accumulation independent of strain range can be determined as shown in Equation 2.26 [7].

$$W = \frac{C\Delta\varepsilon_p}{1+n'}\sum_{1}^{N} N^{\lambda} \qquad \textit{Equation 2.26}$$

C is the initial material strength constant (stress at initial loading cycle on a S-N curve) for a given plastic strain, and can be determined using Equation 2.27. λ is a material constant that can be determined through a log-log plot of the total strain versus the plastic strain for the corresponding hysteresis loop. The value of λ will be positive for cyclic hardening material and negative for cyclic softening material.

$$\Delta\sigma = CN^{\lambda} \qquad \textit{Equation 2.27}$$

Equation 2.26 can be further simplified by replacing the summation portion of the equation with an integral over a stabilized σ-ε curve, and thus, generating Equation 2.28. If the total dissipated energy (*W*) is known, then the number of cycles to failure can be approximated with Equation 2.28.

$$W = \frac{C\Delta\varepsilon_p N^{1+\lambda}}{(1+n')(1+\lambda)} \qquad \textit{Equation 2.28}$$

Finally, the relationship can be further developed to determine the fatigue life based on the critical dissipated energy accumulation (W_c) and dissipated energy per cycle (w). Accordingly, Equation 2.29 expresses the function used to define the number of cycles until failure.

$$N_f = \frac{W}{w} \qquad \textit{Equation 2.29}$$

2.4 Applications of Thermo- Mechanical Fatigue (TMF)

In the TMF field, similar research to that presented in this thesis has been conducted, with some variations in focus and approach. For example, the research of Grieb [26], investigated TMF life predictions for the valve bridge of a cylinder head using several different types of materials. Valve bridge geometry was developed to replicate that of a real cylinder head, as shown in Figure 2.13.

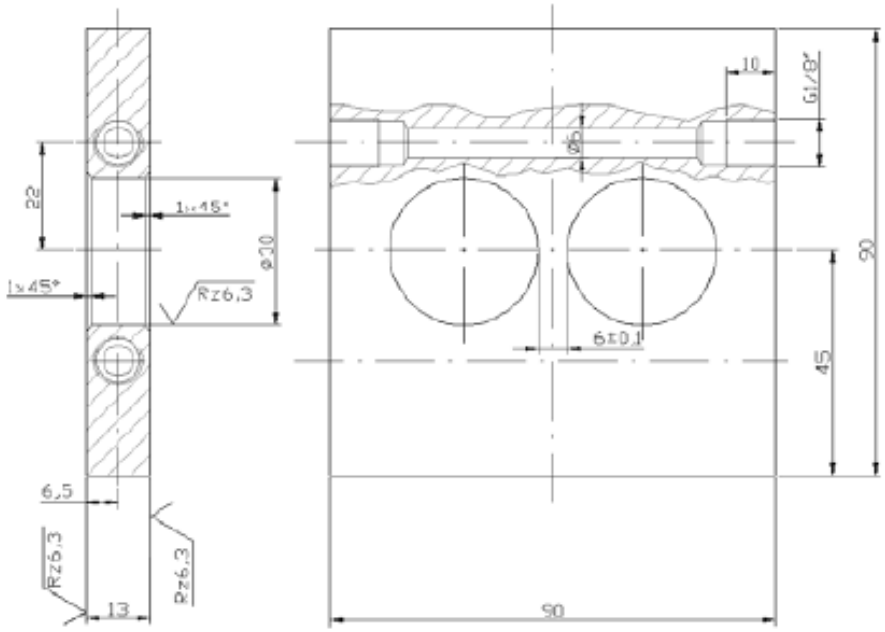

Figure 2.13: Geometry of the fabricated valve bridge that was used in the study of Grieb. [26]

The materials studied included the following: AlSi7Mg-T6, AlSi5Cu1-T6, AlSi5Cu3-T7, AlMg3Si1-T6, AlMg3Si1 (Cu)-T6, and AlMg3Si1 (Sc, Zr)-T5. For the prediction of fatigue life, two damage models were used: the Chaboche model and a damage prediction model developed by IWM Fraunhofer Institute Freiburg. To generate thermal loading, specimens were tested over

the range of 50-400°C. FEA simulations were conducted with ABAQUS for model specimens similar to the experimental specimens. The type of material model used in these studies was not specified, however. The predictions for the fatigue life of the specimens were obtained using the FEA results and compared to the experimental results for fatigue life in actual specimens.

Delprete [16, 17] studied the effects of multi-axial TMF loading, and damage assessments were created for specimens of an exhaust manifold. FEA simulations were conducted on an exhaust manifold using a combined hardening approach that included the effects of oxidation. The determinations of critical areas were based on the locations of maximum stress and strain. The fatigue life estimates were predicted using the following multi-axial damage models; the von Mises, ASME, Sonsino-Grubisic, Kandil-Brown-Miller, and Fatemi-Socie models.

Another attempt to examine the effects of TMF on specimens of a cylinder head was conducted by Trampert, Taner Gocmez, and Stefan Pischinger [27]. In this research different types of cast iron cylinder head materials were investigated. Experiments were conducted on test specimens, and the experimental results were then compared to the results obtained from simulations performed with the same specimen geometry. The type of material model used in this case was a non-linear kinematic hardening model. The TMF life estimates were predicted using the following damage models: the Manson-Coffin, the Energetic Approach, and the Smith-Watson-Topper (SWT) models. The accuracy of the result comparisons were used to validate the predicted fatigue life for the cylinder head specimens as no experimental test data for fatigue life was available for the cylinder head specimens. Fatigue life predictions were conducted for only the combustion chamber geometry; other locations on the cylinder head were not addressed in this research.

2.5 Literature Review Conclusion

Several damage models where studied in this thesis to provide for a better comparison and approximation of the predicted fatigue life. Fatigue damage models based on different criteria (strain, energy, multi-axial, and TMF) were selected to identify what condition each damage model is best suited for.

The previously discussed TMF research all vary slightly in their primary focus. This thesis investigates the accuracy of TMF characteristics of AL319-T7 when modelling the material with only a combined hardening model. This is the first attempt in the TMF research field to accurately model a material experiencing TMF loading using only the combined hardening model while neglecting the effects of oxidation and creep. The other approaches discussed in this literature review attempted to capture viscous effects (creep and oxidation). Also, this thesis applies the Tiara's fatigue life prediction model in a fatigue life calculator program (discussed in Chapter 4), which is not currently available in a known TMF commercial fatigue life prediction software.

Chapter 3 Application of Research Methodology

3.1 Material Model Development from Experimental Results

3.1.1 Background of Research Approach

The first step to determining the material characteristics of the AL319-T7 alloy when subjected to TMF is the development of the material model for use in CAE. Experiments for this thesis were conducted at the University of Michigan to obtain measurements for the mechanical properties of the AL319-T7 alloy; these data were used to determine model parameters. These experiments were conducted over five temperature levels (25, 150, 200, 250, and 300 °C) and at three strain rates ($5x10^{-5}$, $5x10^{-4}$, and $5x10^{-3}$ mm/mm/s). A detailed description and explanation of the procedures, as well as the theory used to develop the AL319-T7 alloy material model, follows.

This section describes the experiments that were performed to obtain the mechanical properties of the AL319-T7 alloy. The experimental procedures followed three different approaches: monotonic loading (tension only), cyclic loading (tension and compression), and TMF cyclic loading (tension and compression with varied temperature). The experimental equipment used for these tests included an MTS servo hydraulic silent flow flex test 40 equipped with a 100 kN load capacity. Table 3.1contains details about the test machine's specifications.

Table 3.1: Experimental testing apparatus specifications

Experimental Equipment	
Machine	MTS servo hydraulic silent flow flex test 40 - 100 kN load capacity
Controller	MPT 793 10 multipurpose test ware version 5.0
Extensometer	MTS Model # 632 54F-14
Heating Coil	Ambrell Easyheat

The test specimens were cut from cast AL319-T7 alloy cylinder heads, and then machined to the appropriate dimensions for testing. The monotonic loading and cyclic (iso-thermal and TMF) loading tests were performed on two types of specimens with different dimensions. The monotonic loading and cyclic loading specimens are depicted in Figure 3.1 and Figure 3.2, respectively. The use of two different geometries during testing is a requirement of the ASTM E606 standards.

The standard testing procedures are listed below:

1. The critical diameter of the specimen must be measured in three different sections and the average value should be used.
2. All of the MPT software windows should be opened and ready for testing.
3. The tensile testing procedure with a ramp function and data acquisition system must be created with the MPT software.
4. The test specimen must be placed in the machine properly, being securely clamped at each end of the specimen.
5. The extensometer is properly mounted on the gauge (centre) section of the specimen.
6. The test can be started once the parameters are all auto offset and the interlocks are all enabled.
7. The test can start at the defined strain rate. The strain and displacement will be recorded. When the specimen fails the test will automatically stop due to the interlocks.

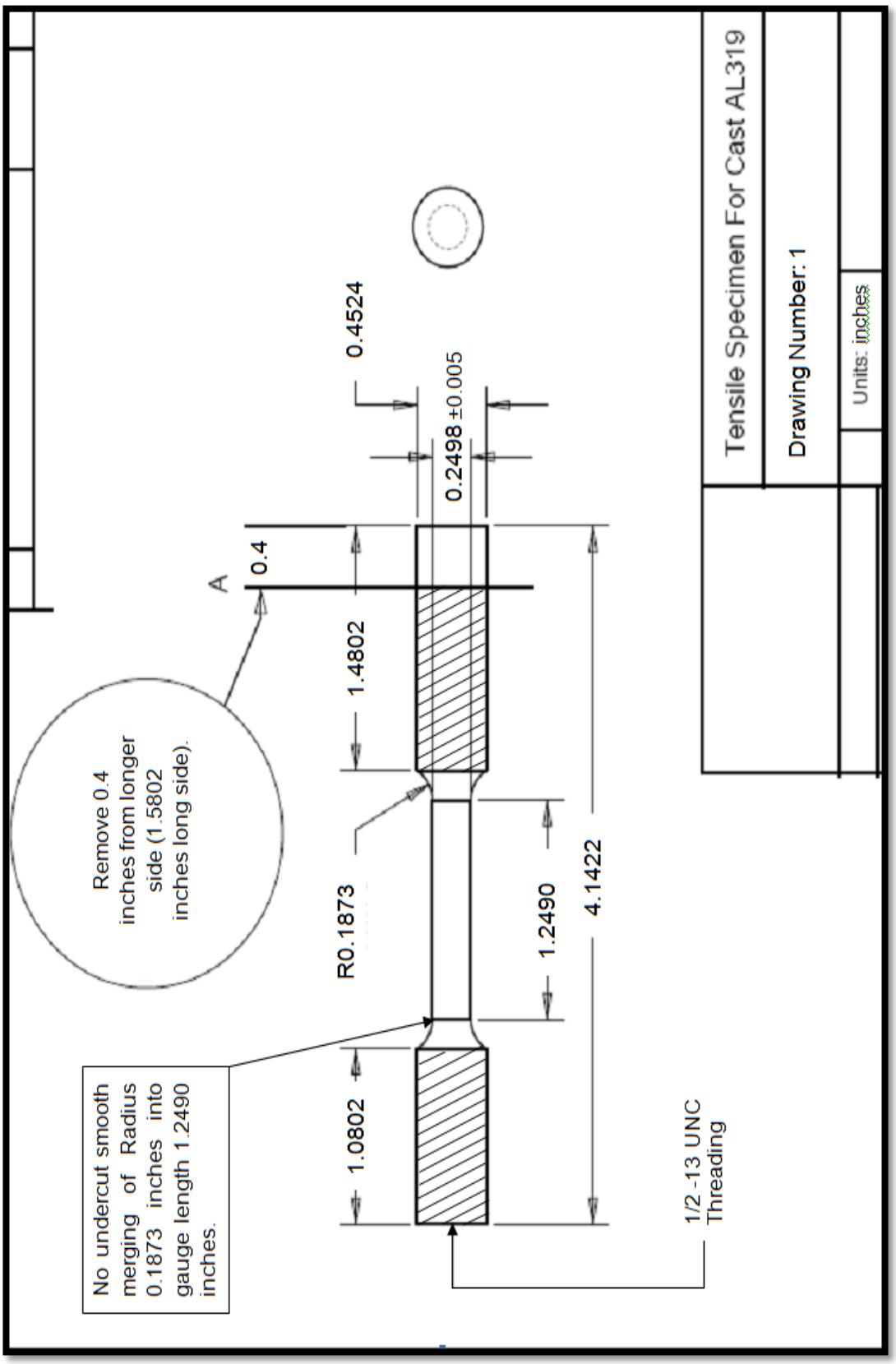

Figure 3.1: Geometry of the AL319-T7 monotonic loading test specimen

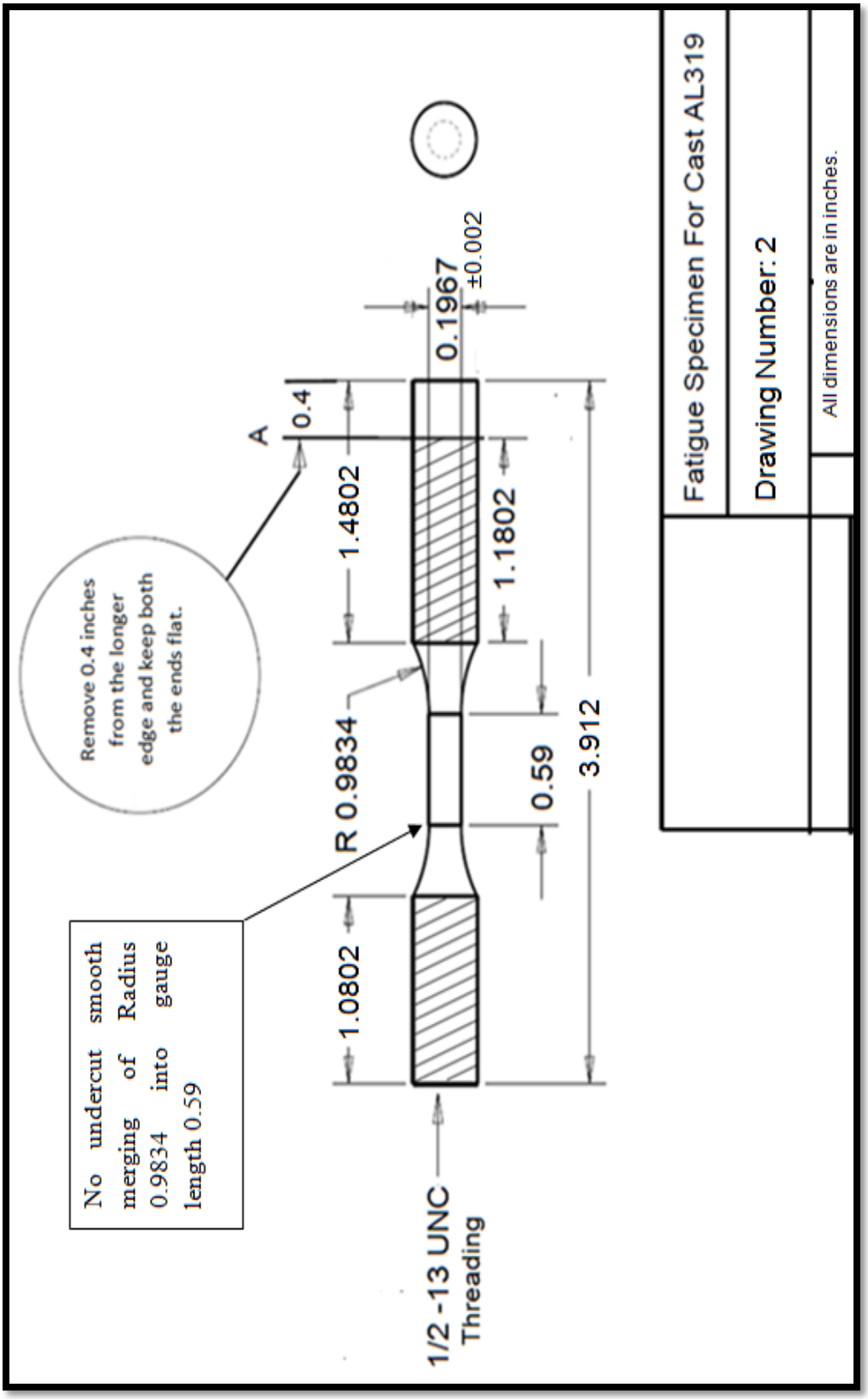

Figure 3.2: Geometry of the AL319-T7 cyclic loading fatigue test specimen

The fatigue test specimens were heated using a heating coil that was wrapped around the test specimen. The heating coil was set at a constant temperature corresponding to one of the five predefined temperatures for the iso-thermal tests. For the TMF tests the heating coil varied the temperature between 150°C and 300°C. Figure 3.3 illustrates set up of the experimental apparatus used in these tests.

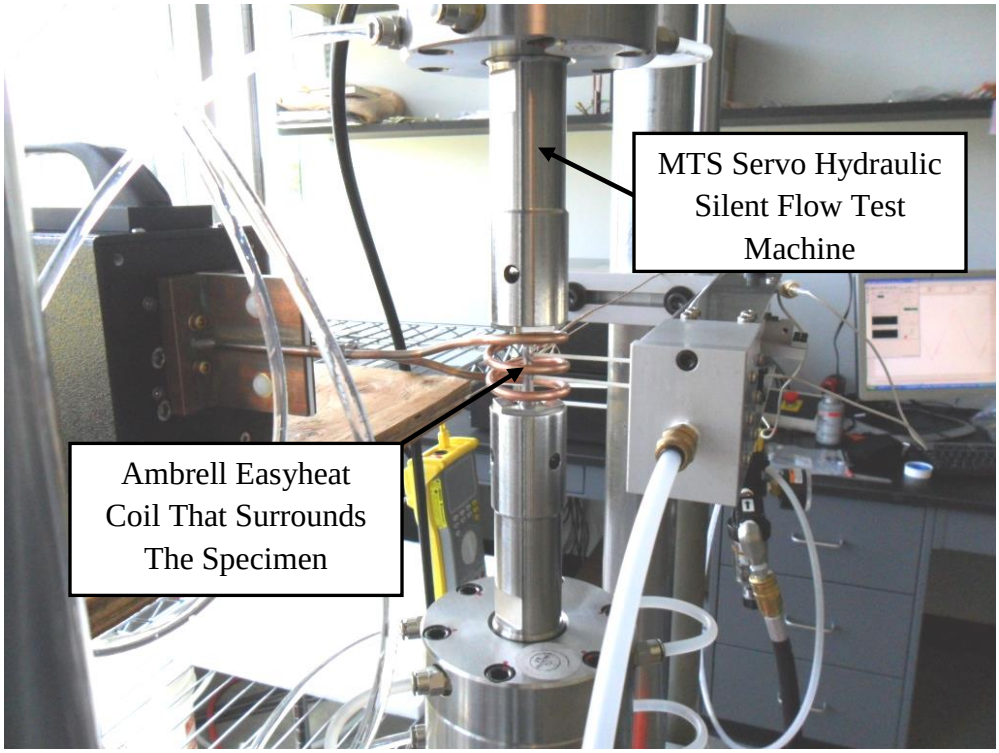

Figure 3.3: Experimental apparatus for the fatigue tests. This image shows the Ambrell Easyheat coil and the MTS servo hydraulic silent flow test machine.

The MTS machine that was used in this study is capable of performing tests requiring load control, strain control, and displacement control; these tests were performed using a strain control approach at three different strain rates. The strain rates tested were $5x10^{-5}$(R1), $5x10^{-4}$(R2), and $5x10^{-3}$(R3) mm/mm/s and will be referred to as R1, R2, and R3 throughout this thesis. In general, strain rate is defined as the derivative of strain with respect to time: the relationship between strain and time is described in Equation 3.1 [4]. In this equation, L_0 is the

original length, $L(t)$ is the length at each time, and $v(t)$ is the speed at which the ends are moving away from each other.

$$\dot{\varepsilon}(t) = \frac{d\varepsilon}{dt} = \frac{d}{dt}\left(\frac{L(t) - L_0}{L_0}\right) = \frac{1}{L_0}\frac{dL}{dt}(t) = \frac{v(t)}{L_0} \qquad \textit{Equation 3.1}$$

The output from the data acquisition system contains the raw data measures for axial displacement (mm), axial force (N), and axial strain (mm/mm) with the corresponding time history. In order to determine the actual mechanical properties of the material, the following equations [4] were used.

$$\sigma_e = \frac{P}{A_0} \qquad \textit{Equation 3.2}$$

$$\varepsilon_e = \frac{l - l_0}{l_0} \qquad \textit{Equation 3.3}$$

$$\sigma = \frac{P}{A} = \frac{P}{A_0}(1 + \varepsilon_e) = \sigma_e(1 + \varepsilon_e) \qquad \textit{Equation 3.4}$$

$$\varepsilon = \int_{l_0}^{l} \frac{dl}{l} = \ln\frac{l}{l_0} \qquad \textit{Equation 3.5}$$

The definitions for the variables in the above four equations are:

- P (Axial Force)
- A_0 (Initial Cross-Sectional Area)
- A *(Actual Instantaneous Area)*
- l (Instantaneous Length of Gauge Section)
- l_0 (Initial Length of Gauge Section)
- σ_e (Engineering Stress)
- ε_e (Engineering Strain)

- σ (True Stress)
- ε (True Strain)

As noted the values for engineering strain (axial strain) are captured by the data acquisition system, and are included in the raw data file. Thus, other related parameters, such as engineering stress, true stress, and true strain, were calculated using the above equations.

3.2 Experimental Data Currently Available

As mentioned above, the research design includes tests that will be conducted over five temperature levels and at three strain rates; however, at this point not all of this experimental data has been collected. At this stage all of the monotonic testing has been completed and the dataset collected under monotonic test conditions is available and complete, however, not all of the cyclic loading data has been collected. For the cyclic loading data, only the R1 data has been collected at all temperature ranges for the iso-thermal and TMF tests. The test required to collect the R2 and R3 strain rate data are yet to be completed, and so are not presented and discussed in this thesis, which focuses on monotonic and cyclic loading at the R1 strain rate for the development and assessment of the material model.

3.2.1 Monotonic Loading Data

The following tables (Table 3.2, Table 3.3, and Table 3.4) contain the monotonic loading data: the "Total Test Time" represents the latency from time zero until the specimen experiences failure; the "Total Axial Displacement" is the total distance travelled by the non-fixed end of the specimen until it experiences failure

Table 3.2: Monotonic loading experimental data available forstrain rate, R1

R1 - $5x10^{-5}$	
25°C	
Total Test Time (s)	**Total Axial Displacement (mm)**
427	0.828651
150°C	
Total Test Time (s)	**Total Axial Displacement (mm)**
839	1.4683703
200°C	
Total Test Time (s)	**Total Axial Displacement (mm)**
520	1.02831
250°C	
Total Test Time (s)	**Total Axial Displacement (mm)**
337	0.97731155
300°C	
Total Test Time (s)	**Total Axial Displacement (mm)**
690	2.1691556

Table 3.3: Monotonic loading experimental data available for strain rate, R2

R2 - $5x10^{-4}$	
25°C	
Total Test Time (s)	**Total Axial Displacement (mm)**
46	0.97015506
150°C	
Total Test Time (s)	**Total Axial Displacement (mm)**
61	1.2378516
200°C	
Total Test Time (s)	**Total Axial Displacement (mm)**
58	1.0135393
250°C	
Total Test Time (s)	**Total Axial Displacement (mm)**
28	0.97009891
300°C	
Total Test Time (s)	**Total Axial Displacement (mm)**
29	1.6616853

Table 3.4: Monotonic loading experimental data available for strain rate, R3

R3 - $5x10^{-3}$	
25°C	
Total Test Time (s)	**Total Axial Displacement (mm)**
4	0.88134474
150°C	
Total Test Time (s)	**Total Axial Displacement (mm)**
5	1.0116192
200°C	
Total Test Time (s)	**Total Axial Displacement (mm)**
9	1.4380398
250°C	
Total Test Time (s)	**Total Axial Displacement (mm)**
12	1.5754163
300°C	
Total Test Time (s)	**Total Axial Displacement (mm)**
6	1.7164412

3.2.2 Iso-thermal Cyclic Test Data

A summary of the cyclic iso-thermal test data that has been collected to date is provided in Table 3.5. For the R2 strain rate, the only data currently available is for the temperature condition of 25°C, and data collection for other temperature conditions is not yet complete. The column "Total Stabilized Cycle Time" in Table 3.5 shows the latency from the beginning of a stabilized hysteresis loop until specimen failure; the variable "Number of Stable Cycles", like the variable "Total Stabilized Cycle Time", is the number of cycles from initiation of a stabilized hysteresis loop until the specimen fails; "Displacement Amplitude" shows the distance that the un-fixed end of the test specimen moves up and down throughout the cycle.

Table 3.5: Cyclic loading experimental data available for strain rate, R1

R1 - $5x10^{-5}$			
25°C			
Strain amplitude (Δε/2)	**Total Stabilized Cycle Time (s)**	**Number of Stable Cycles**	**Displacement Amplitude (mm)**
0.005	400	38	0.116802
0.004	320	25	0.11084
0.003	186	38	0.09435
150°C			
Strain amplitude (Δε/2)	**Total Stabilized Cycle Time (s)**	**Number of Stable Cycles**	**Displacement Amplitude (mm)**
0.005	401	1	0.116802
0.004	331	2	0.11084
0.003	290	2	0.09435
200°C			
Strain amplitude (Δε/2)	**Total Stabilized Cycle Time (s)**	**Number of Stable Cycles**	**Displacement Amplitude (mm)**
0.005	390	8	0.116802
0.004	326	16	0.11084
0.003	251	16	0.09435
250°C			
Strain amplitude (Δε/2)	**Total Stabilized Cycle Time (s)**	**Number of Stable Cycles**	**Displacement Amplitude (mm)**
0.005	399	4	0.116802
0.004	322	10	0.11084
0.003	242	8	0.09435
300°C			
Strain amplitude (Δε/2)	**Total Stabilized Cycle Time (s)**	**Number of Stable Cycles**	**Displacement Amplitude (mm)**
0.005	400	19	0.116802
0.004	NA	NA	NA
0.003	NA	NA	NA

3.2.3 Cyclic Thermal Mechanical Fatigue (TMF) Test Data

Many complications occurred during the performance of the TMF experiments. Many specimens were destroyed during testing while trying to obtain reliable results; consequently, very little data was collected and available for inclusion of this thesis. The only data examined and presented here was collected during an IP TMF test at the R1 strain rate. Temperature was varied between

150°C and 300°C during this IP TMF study. Table 3.6 summarizes the TMF experimental data currently available and examined in this thesis.

Table 3.6: Cyclic TMF experimental data available for strain rate, R1

150°C - 300°C			
Strain amplitude (Δε/2)	**Total Stabilized Cycle Time (s)**	**Number of Stable Cycles**	**Displacement Amplitude (mm)**
0.007	560	87	0.118 and -0.426

3.3 Material Model Development

Two material models need to be developed to replicate the material properties of AL319-T7; one material model to represent monotonic loading and the other to represent cyclic loading. The material model used to characterize monotonic loading is an isotropic hardening model. A combined hardening model, comprised of kinematic and isotropic hardening, was used to simulate cyclic loading. After development, these material models were then applied in ABAQUS to represent the material properties of AL319-T7.

3.3.1 Isotropic Hardening

Isotropic hardening is the uniform expansion of the yield surface when a material undergoes plastic deformation [27], as shown in Figure 3.4.

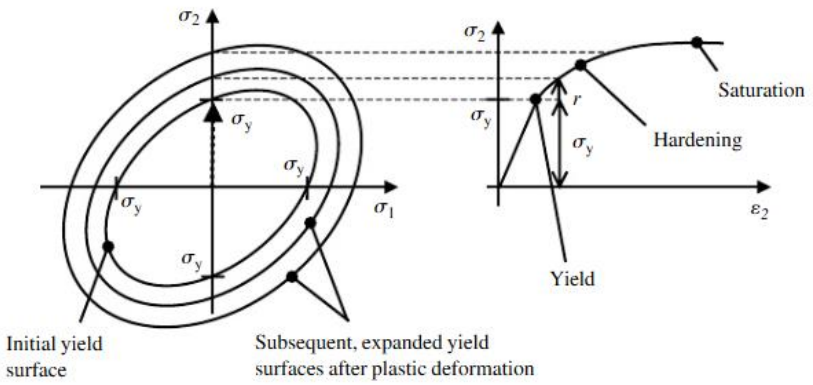

Figure 3.4: Isotropic Hardening. Isotropic hardening is the expansion of the yield surface due to plastic deformation. The curve on the right is the uniaxial σ-ε curve. [27]

The amount of expansion that takes place is a function of the accumulated plastic strain, *p*, and the stress tensor (**σ**); this relationship is defined in Equation 3.6.

$$f(\sigma, p) = \sigma_e - \sigma_y(p) = 0, \text{ where } p = \int_0^t \varepsilon_p(t)dt \qquad \textit{Equation 3.6}$$

In Equation 3.6, the term, σ_e, is a scalar quantity known as the effective stress or the von Mises stress. σ_y is the yield stress developed in the y-direction of loading. The yield stress in the y-direction as a function of plastic strain can also be described in the form of Equation 3.7.

$$\sigma_y(p) = \sigma_{y0} + r(p) \qquad \textit{Equation 3.7}$$

The initial yield stress is denoted as σ_{y0} and the term *r(p)* refers to the isotropic hardening function. To define the term r(p), the initial first derivative is most commonly used [27]. Equation 3.8 represents the first derivative of the isotropic hardening function, and *b* and *Q* are material constants. The form of Equation 3.8 gives an exponential shape to the uniaxial σ-ε curve.

$$\dot{r}(p) = b(Q - r)\dot{p} \qquad \textit{Equation 3.8}$$

Integrating Equation 3.8 with the initial condition of r(0)=0 yields the final isotropic hardening relationship, as seen in Equation 3.9.

$$r(p) = Q\left(1 - e^{-bp}\right) \qquad \textit{Equation 3.9}$$

The material constant, *Q*, is a saturated value and it will ultimately determine the maximum yield stress achieved when using the isotropic hardening model. The term, *b*, determines the rate at which this saturation will occur. The uniaxial σ-ε curve shown in Figure 3.4 is represented by the function defined in Equation 3.9.

3.3.2 Kinematic Hardening

Kinematic hardening involves the translation of the yield surface within the stress space, as shown in Figure 3.5. When monotonic loading is applied, it is a reasonable assumption that only isotropic hardening occurs [27]. However, if cyclic loading occurs, this assumption is no longer valid [27]. Isotropic hardening is not suitable for modeling cyclic loading; when a load reversal occurs, the elastic region of the curve for isotropic hardening is often too large, and does not accurately represent the experimental observations. A true representation of the observations requires a shorter elastic region for the curve, as shown in Figure 3.5. This is called the Bauschinger effect [27].

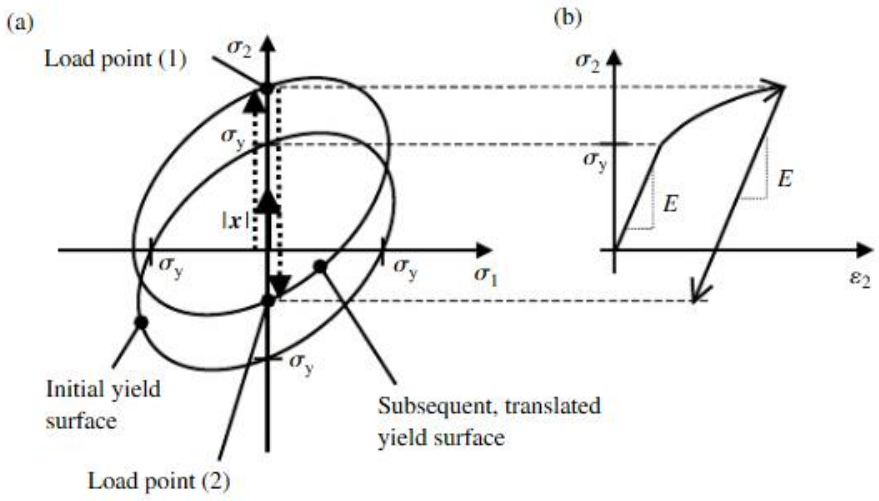

Figure 3.5: Kinematic Hardening. (a) The translation of the yield surface. (b) The σ-ε curve with the translated yield surface. [27]

To capture the translation effect of kinematic hardening the yield function that describes the yield surface must depend on the location of the surface within the stress space. Figure 3.5 shows how the yield surface can be translated when a plastic deformation is applied. Due to this phenomenon the hysteresis loop will translate to the new location by a distance of |x|.

The relationship that defines kinematic hardening in terms of the stresses relative to the new yield surface centre is defined in Equation 3.10 [27].

$$f = \left(\frac{3}{2} (\sigma' - x') : (\sigma' - x') \right)^{\frac{1}{2}} - \sigma_y \qquad \textit{Equation 3.10}$$

In this equation, x' represents the back stress within the stress space, and σ' is the corresponding stress within the stress space.

3.3.3 Combined Hardening

Combined hardening is the combination of both isotropic and kinematic hardening. It is important to use combined hardening for modeling cyclic loading in which many cycles occur. In a single cycle, the dominant form of hardening is kinematic. However, when a large number of cycles occur prior to the point of stabilization, isotropic hardening can occur. The effect a combined hardening model can have on a hysteresis loop is depicted in Figure 3.6.

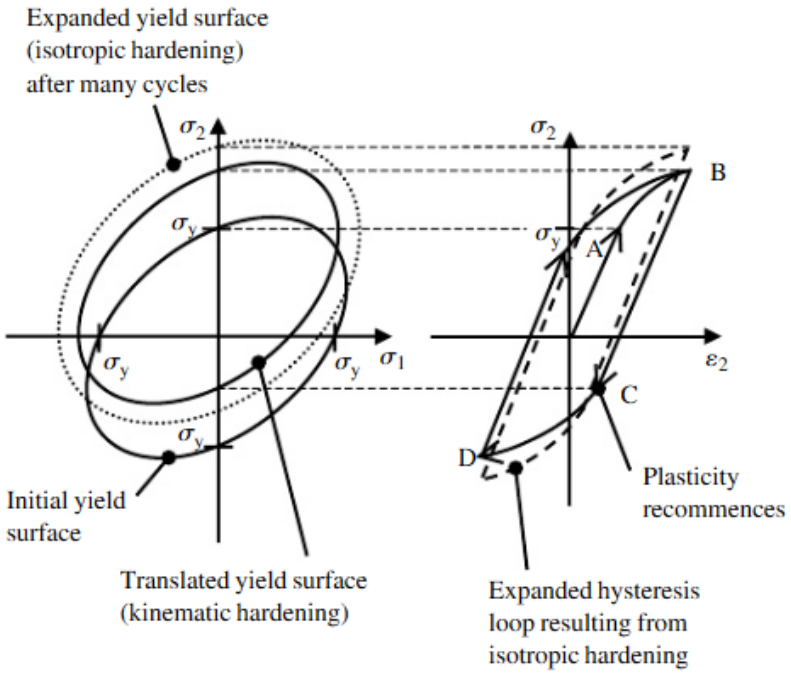

Figure 3.6: Combined Hardening. The effects of both kinematic and isotropic hardening on a hysteresis loop. [27]

For combined hardening the yield function is dependent on three terms: stress, back stress, and accumulated plastic strain. The combined hardening yield function is shown in Equation 3.11.

$$f = J(\sigma' - x') - r(p) - \sigma_y \qquad \textit{Equation 3.11}$$

The consistency condition for combined hardening is:

$$\frac{\partial f}{\partial \sigma} \cdot d\sigma + \frac{\partial f}{\partial x} \cdot dx + \frac{\partial f}{\partial p} dp = 0 \qquad \textit{Equation 3.12}$$

Equation 3.12 can be re-written to include the effects of the plastic multiplier, seen in Equation 3.13.

$$d\lambda = \frac{\left(\frac{\partial f}{\partial \sigma}\right) \cdot d\sigma}{\left(\frac{2}{3}\right) c \left(\frac{\partial f}{\partial \sigma}\right) \cdot \left(\frac{\partial f}{\partial \sigma}\right) - \gamma \left(\frac{\partial f}{\partial \sigma}\right) \cdot x + b(Q - r(p))} \qquad \textit{Equation 3.13}$$

The final form of the combined hardening function for a von Mises material is shown in Equation 3.14.

$$d\sigma = E\left(1 - \frac{E}{E + c - \gamma x + b(Q - r(p))}\right) d\varepsilon \qquad \textit{Equation 3.14}$$

3.3.4 Summary of Material Models

Three material models were presented, isotropic hardening, kinematic hardening, and combined hardening models. The isotropic hardening model simulates the expansion of the yield surface, and is best suited for monotonic loading situations. The kinematic hardening model represents the translation of the yield surface; this type of material model is best suited for modeling one cycle of loading. The combined hardening model incorporates features of isotropic and kinematic hardening. The combined hardening model is best suited for modeling multiple cycles

of loading. The selection and application of these material models in the studies presented in this thesis is solely dependent on the type of loading condition under examination.

3.3.5 Application of the Material Models

In this section, the procedures for the development of the material models for monotonic and cyclic loading are presented. The method used to calculate the material models is derived from the ABAQUS Analysis User Manual (Chp. 22.2.2), which encompasses the material model theory previously described.

Monotonic Loading Material Model Development Steps

To develop the material model that best represents monotonic loading in this thesis (the isotropic hardening model), a series of essential steps must be followed. The following procedure explains the steps in the process used to determine the monotonic material model.

Step 1

Before any of the material properties can be defined, the σ and ε data obtained from the monotonic loading tests must be extracted from the data acquisition files.

Step 2

A material model is required for input into ABAQUS; in this case the isotropic hardening material model, comprised of the plastic strain and the corresponding true stress, was applied. However, before these variables can be determined, the modulus of elasticity for each experimental condition (i.e., each temperature and strain rate) must be calculated. In order to determine the modulus of elasticity, a linear curve was fit to the elastic region of the stress-strain curve for each experimental condition. For example, the modulus of elasticity calculation for the 25°C R3 condition is depicted in Figure 3.7.

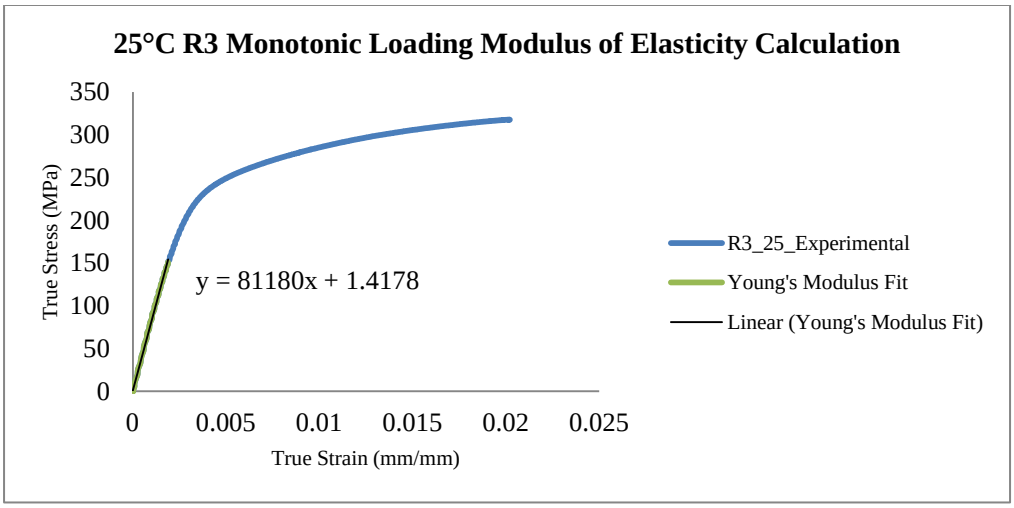

Figure 3.7: Modulus of elasticity calculation example; taken from 25℃ R3 calculation data sheet.

Step 3

Using the modulus of elasticity calculated for each temperature and strain rate condition the amount of plastic strain was determined. The plastic strain values were calculated using Equation 3.15 from the true stress and true strain data that represent the plastic region of the material.

$$\varepsilon_{pl} = \varepsilon - \left(\frac{\sigma}{E}\right) \qquad \textit{Equation 3.15}$$

With the plastic strain determined, a curve was translated to the y-axis, as seen in Figure 3.8. This newly generated curve was then used to represent the isotropic hardening material model.

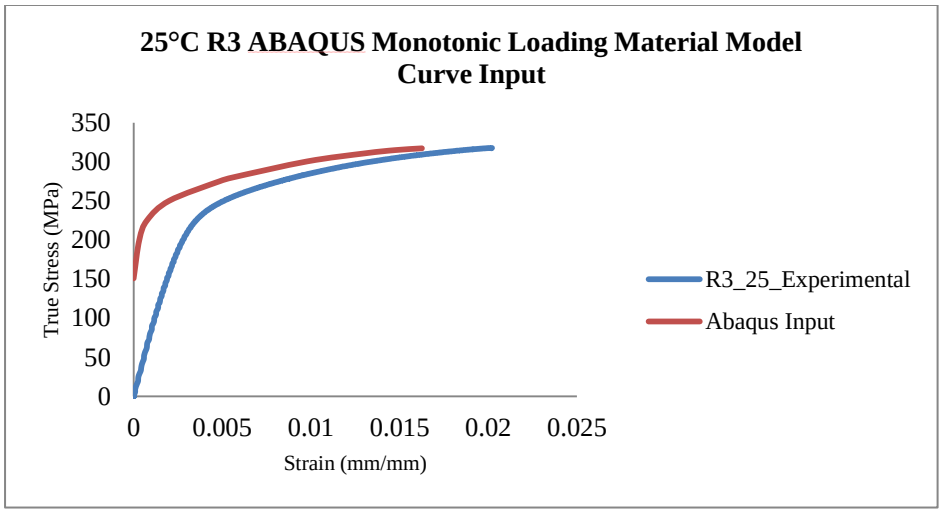

Figure 3.8: Plastic strain and true stress curve for ABAQUS material model; taken from 25°C R3 calculation data sheet.

The monotonic loading material models determined for all of the conditions using the above method can be found in Appendix A (Table A.1 to Table A.13). These are the material models that were provided as input to ABAQUS in order to simulate the monotonic loading material properties of AL319-T7.

Cyclic Loading Material Model Development

The cyclic loading material model requires a much more extensive process than the monotonic loading material model due to its greater complexity. There are two different types of material models that can be used in ABAQUS to represent material properties, "Half Cycle" and "Parameters" models. The methods used in this thesis pertain to the procedures for the "Half Cycle" model. The procedure for the "Parameters" model requires the input of some types of experimental test data (e.g. yield stress at zero plastic strain, kinematic hardening parameter C_1, and Gamma), which were not available in the experimental test data provided for this study. Thus, the "Half Cycle" procedures were followed; further details about the development of the cyclic loading material model used here are found in the next two sections.

Development of the Kinematic Hardening Model

The kinematic hardening component of the combined hardening model can be determined from stabilized test data. A stabilized cycle is a cycle in which a steady state condition of the stress-strain curve is reached due to a fixed strain range (Δε). The σ-ε curve will no longer change in shape from cycle to cycle. Figure 3.9 displays a stabilized σ-ε curve along with the parameters needed to develop the kinematic hardening component of the material model.

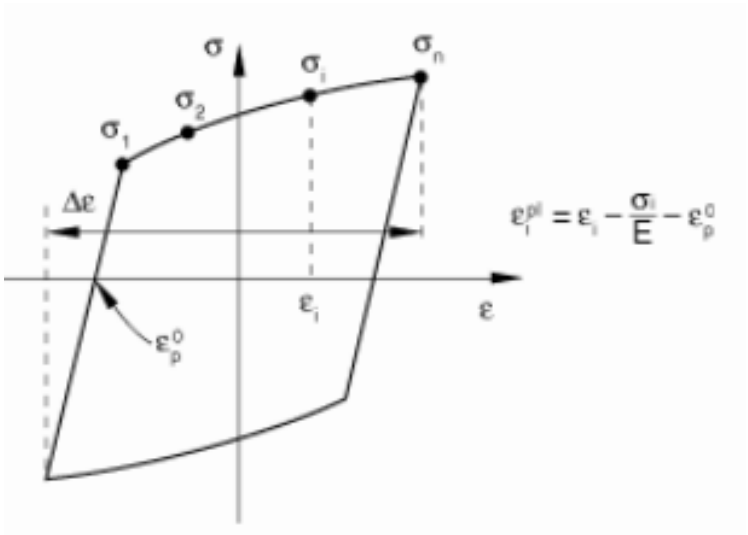

Figure 3.9: Stabilized Stress-Strain curve [11]

The original values of σ and ε must be modified so that the strain axis can shift to begin at the locus of the initial plastic strain (ε_p^0), which is zero on the ε-axis. Thus new values for the plastic strain must be determined using Equation 3.16.

$$\varepsilon_i^{pl} = \varepsilon_i - \frac{\sigma_i}{E} - \varepsilon_p^0 \qquad \textit{Equation 3.16}$$

The variables in Equation 3.16 are described as follows: ε_i is the true strain for cycle *i*, σ_i is the true stress for cycle *i*, E is the material's modulus of elasticity, and ε_p^0 is the strain corresponding to the true stress at zero. Thus, using the plastic strain that has been calculated, with the axis shift

accounted for, and with the true stress known, the material properties due to kinematic hardening were determined.

Development of the Cyclic Isotropic Hardening Model

The following is an explanation of how the isotropic hardening component of the combined hardening model was determined using cyclic loading experimental data. The isotropic hardening component is determined by specifying the equivalent stress based on the size of the initial surface stress (σ^0) as a function of equivalent plastic strain ($\bar{\varepsilon}^{pl}$). Since the material's modulus of elasticity is large compared to its hardening modulus the results can be interpreted as repeated cycles over the same plastic strain range [11], as seen in Equation 3.17.

$$\Delta\varepsilon^{pl} \approx \Delta\varepsilon - \frac{2\sigma_1^t}{E} \qquad \textit{Equation 3.17}$$

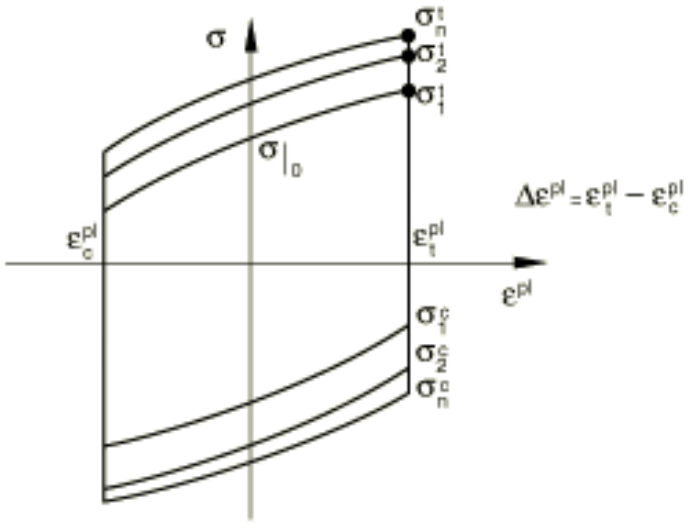

Figure 3.10: Symmetric strain cycle to accompany the plastic strain range ($\Delta\varepsilon^{pl}$). [11]

Figure 3.10 shows the materials isotropic hardening effects as it reaches its stabilized σ-ε curve. The subscripts of *c* and *t* represent compression and tension, respectively. The plastic strain range associated with the effects shown in this figure is found described in Equation 3.17.

To determine the initial surface stress (σ_i^0) of the corresponding cycle, the kinematic component of the yield stress must be isolated; this is assumed for both compression and tension loading cycles. The subscript (*i*) represents the cycle number. The following series of equations explains the processes required to determine the initial surface stress (σ_i^0) and the equivalent plastic strain ($\bar{\varepsilon}_i^{pl}$).

$$\sigma_i^0 = \sigma_i^t - \alpha_i \qquad \textit{Equation 3.18}$$

Equation 3.18 is a function of the peak stress (σ_i^t) of the corresponding cycle in tension and the back stress (α_i). The back stress is a function of the stress in the tension cycle (σ_i^t) and the stress in the compression cycle (σ_i^c), as defined in Equation 3.19.

$$\alpha_i = \frac{\left(\sigma_i^t + \sigma_i^c\right)}{2} \qquad \textit{Equation 3.19}$$

The remaining variable with unknown value that needs to be calculated is the equivalent plastic strain ($\bar{\varepsilon}_i^{pl}$). The equivalent plastic strain ($\bar{\varepsilon}_i^{pl}$) is a function of *i* and the plastic strain range ($\Delta\varepsilon^{pl}$), and is defined in Equation 3.20.

$$\bar{\varepsilon}^{pl} = \frac{1}{2}(4i - 3)\Delta\varepsilon^{pl} \qquad \textit{Equation 3.20}$$

Now, both the values for the initial surface stress and the equivalent plastic strain are known. These data can be used to generate the σ-ε curve that represents the isotropic cyclic hardening property of the material model.

Isotropic and Kinematic Hardening Material Model Development Steps

The initial steps in the procedure to determine the cyclic loading material model are similar to the procedure for determining monotonic loading material model, until the step in which the

Kinematic and Isotropic hardening parameters are determined. The following list describes the steps in the process to determine the cyclic loading material model.

Step 1

As was the case for the monotonic loading material model, the σ and ε data must be obtained from the cyclic loading experimental data.

Step 2

Before the next step can be completed the modulus of elasticity must be calculated for each experimental condition (temperature and strain rate conditions). To determine the modulus of elasticity, a linear curve is fit to the elastic region of a stabilized cyclic σ-ε curve in either the loading or unloading portion of the curve. For example, the calculation for the 25°C R1 condition is shown in Figure 3.11.

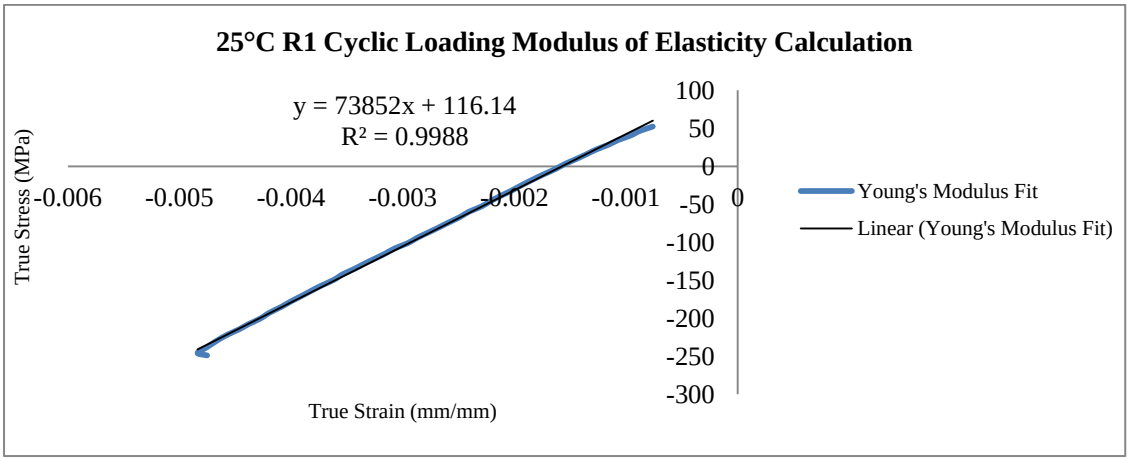

Figure 3.11: Cyclic loading modulus of elasticity calculation example, taken from 25°C R1 calculation data sheet.

Step 3

As was the case for the plastic strain calculation for the monotonic loading data, the plastic strain must be determined for the cyclic loading data. However, the process differs because a combined material model is being used. First the plastic strain offset parameter (ε_p^0) must be determined to

shift the plastic strain curve to the σ-axis, so that the initial plastic strain is 0. This was done using the linear equation developed in Step 2 (modulus of elasticity linear fit, shown in Figure 3.11), and by solving for ε_p^0. Using the linear equation of the line fit to the curve when the stress is equal to zero, the ε_p^0 was calculated.

Step 4

Using the plastic strain offset, the plastic strain was calculated using Equation 3.16.

Step 5

At this point the σ and ε_p were plotted. From this plot, a new curve was created to replicate the plastic region in either the loading or unloading portion of the cycle. The parameters of this new curve were input into ABAQUS as the kinematic hardening material model. Figure 3.12 shows the replicated curve for the R1 25°C condition.

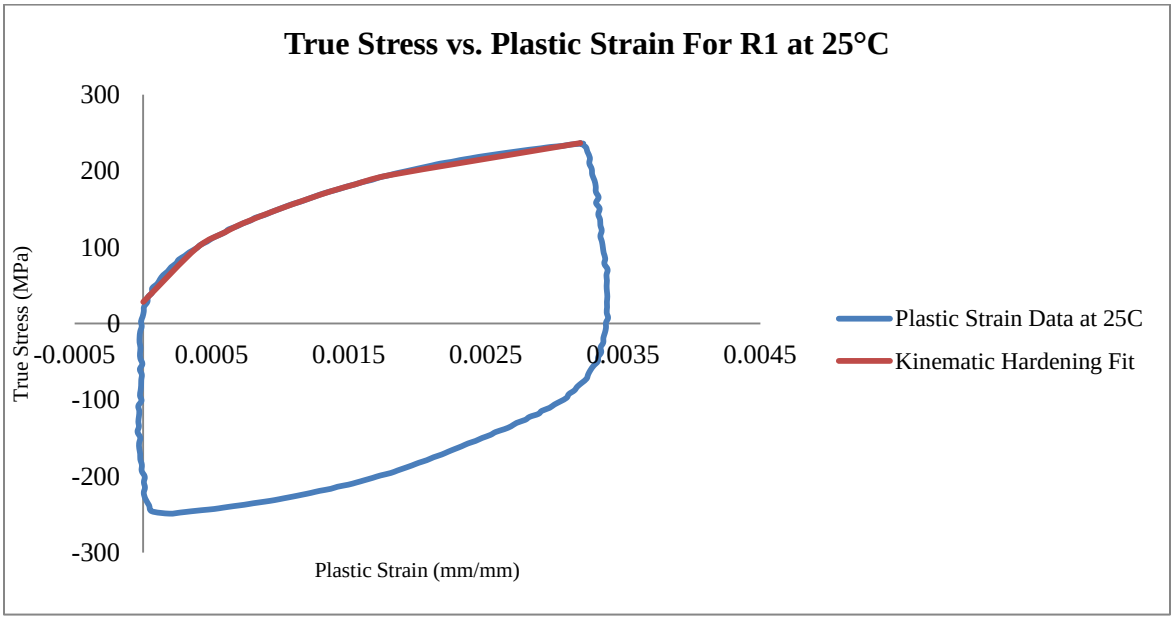

Figure 3.12: Cyclic plastic strain curve fit, taken from 25°C R1 calculation data sheet.

Step 6

The initial step in determining the Isotropic hardening model's material properties uses curves that represent the cyclic hardening (expansion of hysteresis loop) observed in the tested material. In this case, three curves were used; the first curve had the lowest σ_{max} and the third curve had the highest σ_{max}, illustrating the cyclic hardening phenomenon. This process was presented previously, and is illustrated in Figure 3.10.

Step 7

At this point, the plastic strain was calculated for each curve; however, the plastic strain was calculated differently for the Kinematic hardening model than it was for the Isotropic hardening model. In the case of isotropic hardening, the calculation captures the expansion of the material properties, but not the translation. The plastic strain in this case was calculated similarly to the calculation of the monotonic loading plastic strain, as shown in Equation 3.15.

Step 8

The plastic strain range was then determined by linearization of the plastic strain values at the location of maximum stress. This was done by plotting the true stress versus the plastic strain (previously calculated in *Step 7*).

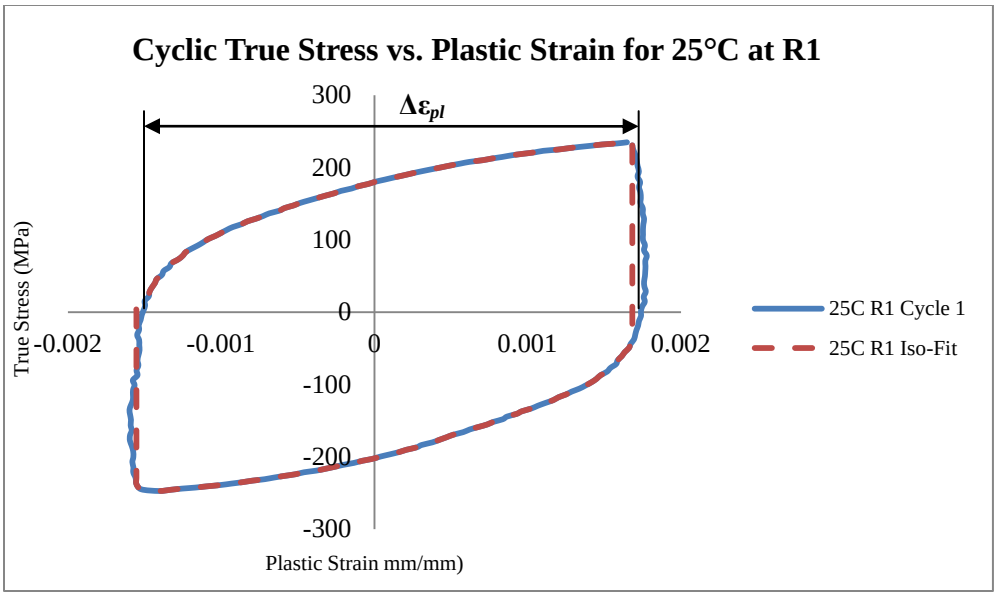

Figure 3.13: Example of the determination of the plastic strain range; taken from 25°C R1 calculation data sheet.

In Figure 3.13 the plastic strain range is approximated when the true stress is zero, which is approximately 0.0035 mm/mm in this case. This procedure was carried out for each of the hysteresis loops that replicate the cyclic hardening of the material, as in the example depicted in Figure 3.10.

Step 9

This step decouples the kinematic component of the yield stress. The initial surface stress (σ_i^0) was calculated using the peak stress (σ_i^t) (also known as σ_{max} of the corresponding cycle) in tension, and subtracting the back stress (α_i). (For clarification of the terms σ_i^0 and σ_i^t refer to the representation in Figure 3.10). To determine the back stress due to the hysteresis loop, the difference in stress between compression and tension states needs to be considered. The back stress was determined using Equation 3.19. Using this value for backstress, the initial yield stress was determined using Equation 3.18.

Step 10

The final step in determining the isotropic hardening properties of the material was to calculate the equivalent plastic strain, using Equation 3.20.

The steps required to build the kinematic and isotropic materials for application in ABAQUS were presented previously. Table A.14-Table A.18.

contain the details for the material models under all of the cyclic loading conditions that were used in ABAQUS to simulate the material properties of AL319-T7.

3.4 Specimen Simulations

This section describes the procedures for both the monotonic and cyclic specimen simulations performed in ABAQUS. Each subsection includes a description of the geometry and the mesh of the test specimen, followed by an explanation of each component of the ABAQUS input simulation file.

3.4.1 Iso-thermal Monotonic Loading Specimen Simulation Overview

Model of Monotonic Loading Specimen: Geometry and Mesh

The specimen model was initially created in CATIA V5 to the dimensions of the ASTM E606 standards for a monotonically loaded specimen, as shown in Figure 3.1. After the creation of the CAD geometry, the model specimen was imported into ABAQUS. In ABAQUS, the mesh was created and is shown in Figure 3.14. The mesh, itself, is comprised of C3D8 (ABAQUS type) quadrilateral elements. There are 4290 elements and 5214 nodes in the model of the tension specimen.

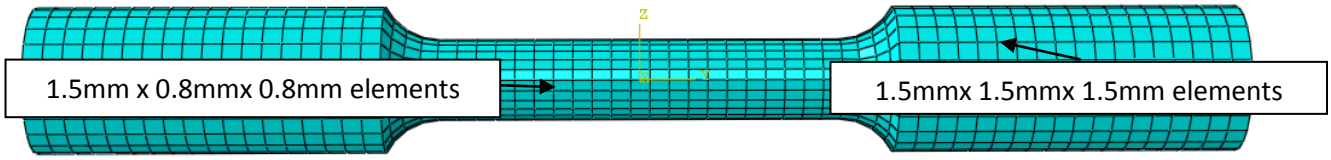

Figure 3.14: Representation of the monotonically loaded meshed specimen model

Monotonic Loading Specimen Model ABAQUS Processing

This section outlines each of the main components of the ABAQUS simulation model, and concludes with the presentation of the ABAQUS input file for clarification.

Monotonic Loading Specimen Model Material Properties

The first set of information required by ABAQUS to perform any calculations is the material properties. The material properties entered into ABAQUS are those that were calculated as described previously, in the Material Model Development section. For the monotonic loading tests, details for the necessary components, *Density, *Elastic, and *Plastic, are entered. The component *Density, represents the density of the material in kg/mm^3. The component *Elastic, includes the modulus of elasticity (MPa) and the Poisson's ratio of the material, and the *Plastic component contains the measure of the true stress (MPa) and the plastic strain (mm/mm) of the material. Figure 3.15 shows an example of the material properties from an ABAQUS input file used in this research.

```
** MATERIALS
**
*Material, name=AL319
*Density
 2.3e-09,
*Elastic
81180., 0.33
*Plastic
 150.841,           0.
 200.038, 0.000320411
 225.181,  0.00075972
 250.099,  0.00200684
 275.028,  0.00483945
 280.061,  0.00560741
 300.489,  0.00978846
 310.918,     0.013078
 314.935,    0.0147456
 317.228,    0.0162565
```

Figure 3.15: ABAQUS input of monotonic loading material properties for 25°C at R3, which includes the density, elastic, and plastic properties' of the material.

Monotonic Loading Specimen Model Coupling Constraints

To replicate the experimental observations, the model specimen needed to have one end fixed and the other end free to move along the vertical axis only. To do this, a coupling constraint was made at each end, with two different reference points (RP). These reference points were coupled to nodes, which represent the clamped portion of the specimen (fixed and moveable ends). This means that any boundary condition applied to the reference point will cause all of the coupled nodes to act in the same way. Figure 3.16 depicts these reference points, identified as RP-1 and RP-2.

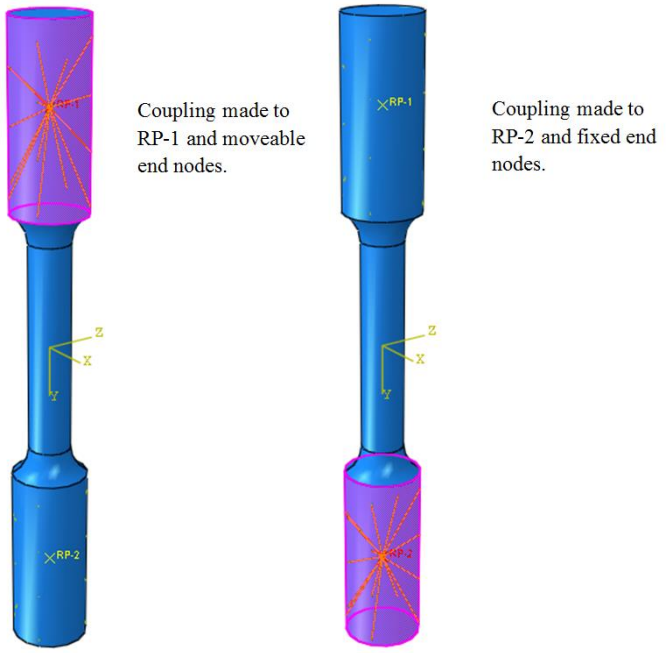

Figure 3.16: Monotonic loading specimen model coupling reference points.

The ABAQUS input file shown in, Figure 3.17 presents the code defining these coupling constraints. In this block of code, RP-1 is linked to the nodes associated with the upper moveable end of the specimen (_PickedSet7_CNS_), RP-2 is linked to the nodes associated with the lower fixed end of the specimen (_PickedSet9_CNS). This means that each RP is linked to a defined node set.

```
** Constraint: Constraint-1
*Coupling, constraint name=Constraint-1, ref node=_PickedSet8, surface=_PickedSet7_CNS_
*Kinematic
** Constraint: Constraint-2
*Coupling, constraint name=Constraint-2, ref node=_PickedSet10, surface=_PickedSet9_CNS_
*Kinematic
```

Figure 3.17: ABAQUS input of monotonic loading coupling constraints for 25°C at R3.

Monotonic Loading Specimen Model: Boundary Conditions

Defined boundary conditions are used to emulate the experimental conditions. The monotonic loading simulation has 9 boundary conditions, as shown in Figure 3.18. For example, the boundary conditions for the 25°C R3 condition are defined in this portion of the input file as

follows: BC-3 is linked to RP-2 coupling and allows displacement in the y-direction by a pre-determined amount; BC-4 is linked to RP-2 coupling and prevents displacement in the x direction; BC-5 is linked to RP-2 coupling and prevents displacement in the z direction; BC-6 is linked to RP-2 coupling and prevents rotation about the x-axis; BC-7 is linked to RP-2 coupling and prevents rotation about the y-axis; BC-8 is linked to RP-2 coupling and prevents rotation about the z-axis; and BC-9 is linked to RP-1 and prevents all displacements and rotations.

```
** BOUNDARY CONDITIONS
**
** Name: BC-3 Type: Displacement/Rotation
*Boundary, amplitude=Amp-1
_PickedSet39, 2, 2, 0.881345
** Name: BC-4 Type: Displacement/Rotation
*Boundary, amplitude=Amp-1
_PickedSet46, 1, 1
** Name: BC-5 Type: Displacement/Rotation
*Boundary, amplitude=Amp-1
_PickedSet47, 3, 3
** Name: BC-6 Type: Displacement/Rotation
*Boundary, amplitude=Amp-1
_PickedSet48, 4, 4
** Name: BC-7 Type: Displacement/Rotation
*Boundary, amplitude=Amp-1
_PickedSet49, 5, 5
** Name: BC-8 Type: Displacement/Rotation
*Boundary, amplitude=Amp-1
_PickedSet50, 6, 6
** Name: BC-9 Type: Displacement/Rotation
*Boundary, amplitude=Amp-1
+--  6 lines: _PickedSet45, 1, 1---------------
```

Figure 3.18: ABAQUS input of monotonic loading boundary conditions for 25°C at R3.

Monotonic Loading: Specimen Model Amplitude

The amplitude applied to the previously described boundary conditions was used to simulate the monotonic loading experiment; the specimen was displaced in only one direction from start to end. For this condition (R3 at 25°C), the time lapse was 4.1582031 seconds; this short time period was due to the very high strain rate (R3). Figure 3.19 shows segments of the ABAQUS input for the amplitude applied to simulate a monotonic loading experiment. The values in the centre (0 and 4.1582031) indicate the time (in seconds) for application of the boundary conditions. The outer values (0 and 1) indicate the change in the displacement applied to RP-2. In ABAQUS, increments of 0.1 seconds are created for the time span from 0 to 4.1582031

seconds. The time, 0.1 seconds was used to capture enough data points for a true representation of the σ-ε curve. For each of these increments, the stress and strains are calculated until the final condition is met.

```
*Amplitude, name=Amp-1, time=TOTAL TIME
         0.,           0.,    4.1582031,           1.
```

Figure 3.19: ABAQUS input of monotonic loading amplitude for 25°C at R3

Monotonic Loading Specimen Model: Predefined Fields

A predefined field is used to apply a temperature field to each node of the model. Figure 3.20 shows the input to apply a temperature of 25°C to _PickedSet56 (i.e., all nodes of the monotonic loading specimen model). This predefined field was used to replicate an iso-thermal monotonic loading test.

```
** PREDEFINED FIELDS
**
** Name: Predefined Field-1   Type: Temperature
*Temperature
_PickedSet56, 25.
```

Figure 3.20: ABAQUS input of monotonic loading predefined field for 25°C at R3

Monotonic Loading Specimen Model: Loading Steps

To simulate a monotonic loading test, only one step is required, as seen in Figure 3.21. In this step, the simulation simply displaces the moveable end of the specimen by the amount defined by the boundary conditions for the period of time indicated by the amplitude. ABAQUS then calculates the relevant outcome data, such as the logarithmic strain (LE) and the stress (S), which can be then used for post-processing analyses.

```
** STEP: Step-1
**
*Step, name=Step-1, nlgeom=YES, inc=10000
*Visco, cetol=0.01
0.01, 4.1582, 1e-05, 0.1
**
** BOUNDARY CONDITIONS
**
** Name: BC-3 Type: Displacement/Rotation
*Boundary, amplitude=Amp-1
_PickedSet39, 2, 2, 0.881345
** Name: BC-4 Type: Displacement/Rotation
*Boundary, amplitude=Amp-1
_PickedSet46, 1, 1
** Name: BC-5 Type: Displacement/Rotation
*Boundary, amplitude=Amp-1
_PickedSet47, 3, 3
** Name: BC-6 Type: Displacement/Rotation
*Boundary, amplitude=Amp-1
_PickedSet48, 4, 4
** Name: BC-7 Type: Displacement/Rotation
*Boundary, amplitude=Amp-1
_PickedSet49, 5, 5
** Name: BC-8 Type: Displacement/Rotation
*Boundary, amplitude=Amp-1
_PickedSet50, 6, 6
** Name: BC-9 Type: Displacement/Rotation
*Boundary, amplitude=Amp-1
+--  6 lines: _PickedSet45, 1, 1--------------
```

```
** PREDEFINED FIELDS
**
** Name: Predefined Field-1   Type: Temperature
*Temperature
_PickedSet56, 25.
**
** OUTPUT REQUESTS
**
*Restart, write, frequency=0
**
** FIELD OUTPUT: F-Output-1
**
*Output, field, variable=PRESELECT
**
** HISTORY OUTPUT: H-Output-1
**
*Output, history
*Element Output, elset=Wire-1-Set-1
IRF1, IRF2, IRF3, IRM1, IRM2, IRM3
**
** HISTORY OUTPUT: H-Output-2
**
*Output, history, variable=PRESELECT
*End Step
```

Figure 3.21: ABAQUS input of monotonic loading step sequence for 25°C at R3

3.4.2 Iso-thermal Cyclic Loading Specimen Model Simulation

Iso-thermal Cyclic Loading Specimen Model Geometry and Mesh

The iso-thermal cyclic loading specimen was initially created in CATIA V5 to the dimensions of the ASTM E606 standards for a cyclic loading specimen, shown in Figure 3.2. Next, the model specimen was imported into HyperMesh for pre-processing (mesh creation). The mesh created using HyperMesh is shown in Figure 3.22. This mesh is comprised of HEX8 (C3D8 ABAQUS equivalent) elements: 1972 nodes and 1482 elements. After the meshing process was completed, the model was exported to ABAQUS.

Figure 3.22: Iso-thermal cyclic loading meshed specimen model.

Iso-thermal Cyclic Loading Specimen Model ABAQUS Processing

This section outlines each of the main components of the cyclic loading ABAQUS simulation model (similarly to the presentation of the monotonic simulation model presented earlier), and concludes by presenting examples of the ABAQUS input files to enhance understanding.

Iso-thermal Cyclic Loading Specimen Model: Material Properties

The material properties entered into ABAQUS are those that were calculated from the cyclic iso-thermal fatigue experiments, which represent isotropic and kinematic hardening. For the cyclic tests this requires the entry of the following components: *Density, *Elastic, *Plastic, and *Cyclic Hardening. The model used here is the combined type of hardening model. The *Density input command represents the density of the material in kg/mm^3, the *Elastic input command contains the modulus of elasticity (MPa) and the Poisson's ratio of the material, and the *Plastic input command contains the kinematic properties of the material, the true stress (MPa) and the plastic strain (mm/mm) of the material. The *Cyclic Hardening input command includes the true stress (MPa) of each cyclic hardening cycle and the equivalent plastic strain (mm/mm). The "datatype" used is "STABILIZED", which means that the *Plastic material properties were created using the ABAQUS stabilized calculation method. A stabilized cycle is a state in which the hysteresis loop no longer shows the effects of cyclic hardening and softening, thus each continuous cycle is approximately the same. Figure 3.23 shows an example of the input data for material properties taken from the ABAQUS input file for the cyclic loading simulation condition of 25°C at R1.

```
** MATERIALS
**
*Material, name=AL319
*Density
 2.3e-09,
*Elastic
73852., 0.33
*Plastic, dependencies=1, hardening=COMBINED, datatype=STABILIZED
 52.2959,          0., ,         25.,       5e-05
 98.6655, 0.000388073, ,         25.,       5e-05
 119.649, 0.000596407, ,         25.,       5e-05
 131.266, 0.000726965, ,         25.,       5e-05
 149.543, 0.000984584, ,         25.,       5e-05
 163.019,  0.00119773, ,         25.,       5e-05
 173.051,  0.00136336, ,         25.,       5e-05
 182.436,  0.00154649, ,         25.,       5e-05
 194.163,  0.00178819, ,         25.,       5e-05
 235.853,  0.00320883, ,         25.,       5e-05
*Cyclic Hardening, dependencies=1
  52.295,          0.,        25.,      5e-05
  134.16, 0.00166227,         25.,      5e-05
 145.865, 0.00831137,         25.,      5e-05
 148.595,  0.0149543,         25.,      5e-05
```

Figure 3.23: ABAQUS input of cyclic loading material properties for 25°C at R1

Iso-thermal Cyclic Loading Specimen Model Coupling Constraints

To simulate the isothermal cyclic loading experiments, the specimen needs to have one end fixed and the other end free to move along the vertical axis, as in the monotonic loading simulations. In order to do this, a coupling constraint was applied to each end with two different reference points (RP). These reference points are coupled to nodes, which means that any boundary condition applied to the reference point will cause all of the coupled nodes to act in the same way. Figure 3.24 displays these two reference points (RP-1 and RP-2) for the cyclic loading specimen model.

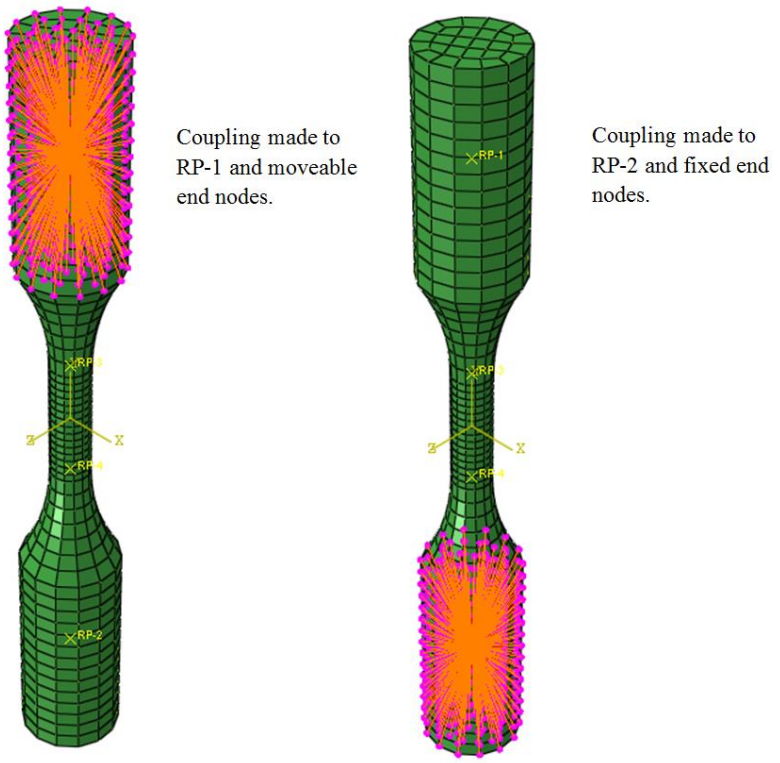

Figure 3.24: Cyclic loading specimen model coupling reference points.

The ABAQUS input file that describes these coupling constraints is shown in Figure 3.25. RP-1 is linked to the nodes associated with the upper moveable end of the specimen (_PickedSet7_CNS_), RP-2 is linked to the nodes associated with the lower fixed end of the specimen (_PickedSet9_CNS). This means that each RP is linked to a defined node set.

```
** Constraint: Constraint-1
*Coupling, constraint name=Constraint-1, ref node=_PickedSet8, surface=_PickedSet7_CNS_
*Kinematic
** Constraint: Constraint-2
*Coupling, constraint name=Constraint-2, ref node=_PickedSet10, surface=_PickedSet9_CNS_
*Kinematic
```

Figure 3.25: ABAQUS input of the cyclic coupling constraints for 25°C at R1.

Iso-thermal Cyclic Loading Specimen Model: Boundary Conditions

The experimental conditions for the cyclic loading specimen simulations are emulated with defined boundary conditions. The cyclic loading simulation has seven boundary conditions, and the cyclic loading simulation input file (Figure 3.26) defines these boundary conditions as

follows: BC-1is linked to RP-1 coupling and prevents displacement in the x-direction; BC-2 is linked to RP-1 and allows displacement in the y-direction by a predetermined amount, as shown in Figure 3.26; BC-3 is linked to RP-1 coupling and prevents displacement in the z direction; BC-4 is linked to RP-1coupling and prevents rotation about the x-axis; BC-5 is linked to RP-1 coupling and prevents rotation about the y-axis; BC-6 is linked to RP-1 coupling and prevents rotation about the z-axis; and BC-7 is linked to RP-2 and prevents all displacements and rotations.

```
** BOUNDARY CONDITIONS
**
** Name: BC-1 Type: Displacement/Rotation
*Boundary, amplitude=Amp-1
_PickedSet11, 1, 1
** Name: BC-2 Type: Displacement/Rotation
*Boundary, amplitude=Amp-1
_PickedSet12, 2, 2, 0.095
** Name: BC-3 Type: Displacement/Rotation
*Boundary, amplitude=Amp-1
_PickedSet13, 3, 3
** Name: BC-4 Type: Displacement/Rotation
*Boundary, amplitude=Amp-1
_PickedSet14, 4, 4
** Name: BC-5 Type: Displacement/Rotation
*Boundary, amplitude=Amp-1
_PickedSet15, 5, 5
** Name: BC-6 Type: Displacement/Rotation
*Boundary, amplitude=Amp-1
_PickedSet16, 6, 6
** Name: BC-7 Type: Symmetry/Antisymmetry/Encastre
*Boundary
_PickedSet17, ENCASTRE
```

Figure 3.26: ABAQUS input of the cyclic loading boundary conditions for 25°C at R1.

Iso-thermal Cyclic Loading Specimen Model: Amplitude

The amplitude applied in the boundary conditions described above simulates a cyclic loading experiment; the input file describing the application of amplitude along with a loading history graph is shown in Figure 3.27. Thus, the model specimen is displaced in two directions for one cycle. In this case (R1 at 25°C), the duration of a half cycle is about 200 seconds. The total time elapsed is 4090 seconds, which represents 10 stabilized cycles. The values in the first row include the latency (in seconds) to apply the boundary conditions; the values of -1 and 1

represent the negative and positive displacements relative to RP-1. The stress and strains are calculated for each increment of 0.1 seconds until the final time condition is met.

```
*Amplitude, name=Amp-1, time=TOTAL TIME
          0.,           0.,          90.,           1.,         288.,          -1.,         490.,           1.
        688.,          -1.,         890.,           1.,        1088.,          -1.,        1290.,           1.
       1488.,          -1.,        1690.,           1.,        1888.,          -1.,        2090.,           1.
       2288.,          -1.,        2490.,           1.,        2688.,          -1.,        2890.,           1.
       3088.,          -1.,        3290.,           1.,        3488.,          -1.,        3690.,           1.
       3888.,          -1.,        4090.,           1.
```

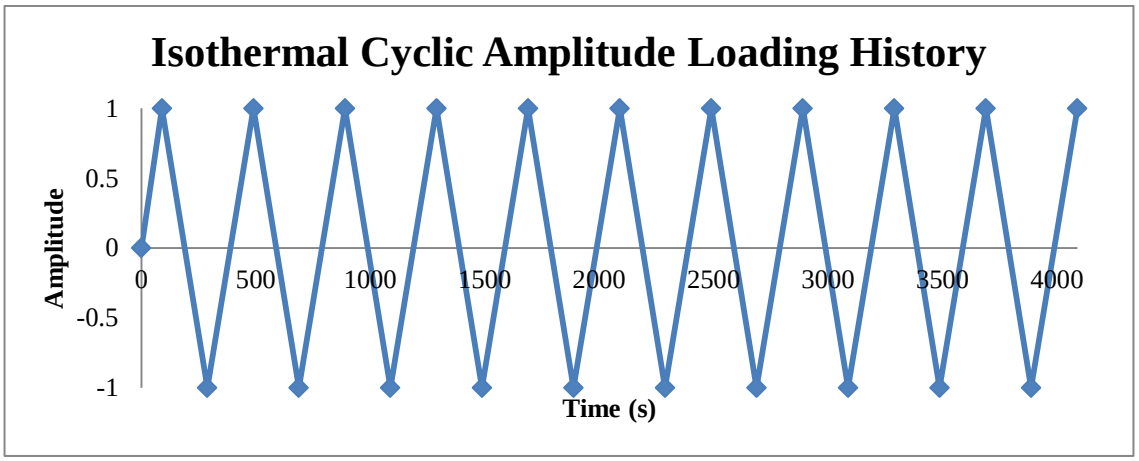

Figure 3.27: ABAQUS input of the cyclic loading amplitude for 25°C at R1.

Iso-thermal Cyclic Loading Specimen Model: Predefined Fields

A temperature field is applied to each node using a predefined field. Figure 3.28 shows that a temperature of 25°C was applied to _PickedSet25, which is comprised of all nodes in the cyclic loading specimen model; thus, this predefined field replicates an iso-thermal test.

```
** PREDEFINED FIELDS
**
** Name: Predefined Field-1   Type: Temperature
*Temperature
_PickedSet25,  25.
```

Figure 3.28: ABAQUS input of the cyclic loading predefined field for isothermal conditions (25°C at R1).

Iso-thermal Cyclic Loading Specimen Model: Procedural Steps

To ensure that the material model was stable, 10 stabilized cycles were simulated. Thus, there were 20 steps in total, plus one initial step. Each step represents a half-cycle of either the loading or the unloading condition, depending on the condition specified for that particular procedural

step. For example, if the latency for the completion of a half-cycle is 200 seconds during the experiment, then completion of one step of the simulations will also take 200 seconds. The amplitude applied to each step was coordinated with the appropriate time intervals, so that the proper loading and unloading displacements were applied at each step of the simulation. An example of the ABAQUS input file describing the procedures for step 8 is shown in Figure 3.29. ABAQUS records the data, such as logarithmic strain (LE) and the stress (S), necessary for post-processing analyses.

Time Period: 198

Max. # of Increments: 500

Initial Increment size: 0.1

Min. Increment Size: 5e-05

Maximum Increment Size: 50

```
** STEP: Step-8
**
*Step, name=Step-8, nlgeom=YES, inc=500
*Visco, cetol=0.01
0.1, 198., 5e-05, 50.
**
** OUTPUT REQUESTS
**
*Restart, write, frequency=0
**
** FIELD OUTPUT: F-Output-1, F-Output-2, F-Output-3, F-Output-4, F-Output-5
**
*Output, field, variable=PRESELECT
**
** HISTORY OUTPUT: H-Output-1
**
*Output, history, variable=PRESELECT
*End Step
```

Figure 3.29: ABAQUS input of the cyclic loading step sequence for Step-8 at 25°C at R1.

3.4.3 TMF Cyclic Loading Specimen Simulation

TMF Cyclic Loading Specimen Model: Geometry and Mesh

The TMF cyclic loading specimen model is identical in every way to the iso-thermal cyclic loading specimen model described in Section 3.4.2. The model specimen was initially created in CATIA V5 to the dimensions of the ASTM E606 standards for a cyclic specimen, and was then imported into HyperMesh for pre-processing. The mesh created with HyperMesh is shown in Figure 3.30, and is comprised of HEX8 (C3D8 ABAQUS equivalent) elements (1972 nodes and 1482 elements). After the meshing of the model specimen was complete, it was exported for processing with ABAQUS.

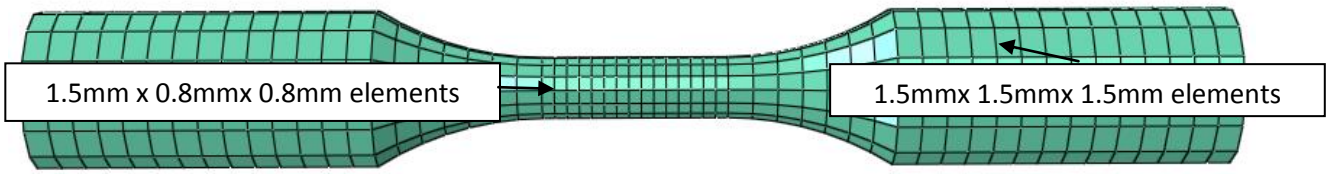

Figure 3.30: TMF cyclic loading meshed specimen model.

TMF Cyclic Loading Specimen Model: ABAQUS Processing

This section outlines each of the main components of the TMF cyclic loading ABAQUS simulation model, and will conclude with an example of the ABAQUS input file for clarification.

TMF Cyclic Loading Specimen Model: Material Properties

The material properties entered into ABAQUS to simulate TMF cyclic loading are the same as the properties used in the isothermal cyclic loading simulation. To review, the cyclic loading test requires the entry of the following components: *Density, *Elastic, *Plastic, and *Cyclic Hardening (as defined in Sections 3.4.2 for the iso-thermal cyclic loading specimen simulation). Figure 3.31 shows an example of the material properties for the TMF simulation taken from an ABAQUS input file. For the TMF cyclic loading specimen simulation, however, the *Elastic and *Plastic commands contain the material properties for each temperature condition, so that ABAQUS can interpolate material properties through thermal loading cycles.

```
** MATERIALS
**
*Material, name=AL319
*Density
 2.3e-09,
*Depvar
      5,
*Elastic
73852., 0.33,  25.
77553., 0.33, 150.
75657., 0.33, 200.
68498., 0.33, 250.
54717., 0.33, 300.
*Expansion, zero=25.
+--  4 lines: 2.2e-05,150.----------------------------------------------------------------------
*Plastic, dependencies=1, hardening=COMBINED, datatype=STABILIZED, number backstresses=2
+-- 81 lines: 52.2959,          0., ,         25.,       5e-05----------------------------------
*Cyclic Hardening, dependencies=1
+-- 18 lines: 52.295,         0.,        25.,      5e-05----------------------------------------
**
```

Figure 3.31: ABAQUS input for the TMF cyclic loading simulation's material properties.

TMF Cyclic Loading Specimen Model: Coupling Constraints

To replicate the TMF cyclic loading experiments, the model specimen has one fixed end and the other end is free to move along the vertical axis. Consequently, the same coupling constraints were used in this simulation as were used in the iso-thermal cyclic loading simulations. Figure 3.32 displays the reference points for the simulation of TMF cyclic loading; these are the same as the reference points for the simulations of iso-thermal cyclic loading specimens.

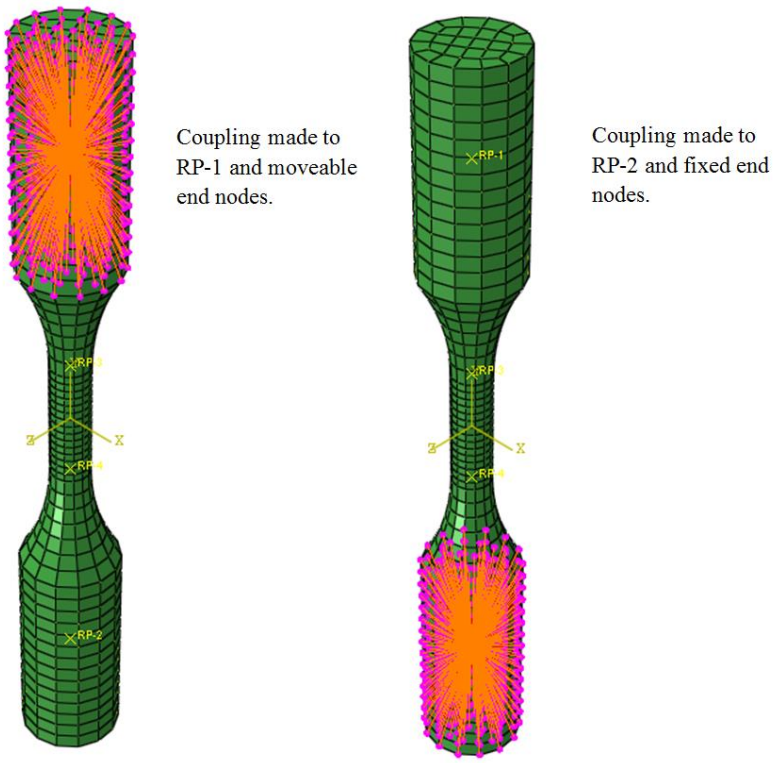

Figure 3.32: TMF cyclic loading model specimen's coupling reference points.

TMF Cyclic Loading Specimen Model: Boundary Conditions

Defined boundary conditions were also used to simulate the effects of the TMF cyclic loading experimental conditions on the test specimens. The TMF cyclic loading simulation had seven boundary conditions, as was also the case for the iso-thermal cyclic loading simulation (Figure 3.33). The boundary conditions described in the TMF cyclic loading simulation input file are similar to those for the iso-thermal cyclic loading simulations: BC-1is linked to RP-1 coupling and prevents displacement in the x-direction, BC-2 is linked to RP-1 and allows displacement in the y-direction by a predetermined amount (defined by the amplitude "newbcamp" as shown in Figure 3.33), BC-3 is linked to RP-1 coupling and prevents displacement in the z direction, BC-4 is linked to RP-1coupling and prevents rotation about the x-axis, BC-5 is linked to RP-1 coupling and prevents rotation about the y-axis, BC-6 is linked to RP-1 coupling and prevents rotation about the z-axis, and BC-7 is linked to RP-2 and prevents all displacements and rotations.

```
** BOUNDARY CONDITIONS
**
** Name: BC-1 Type: Displacement/Rotation
*Boundary, amplitude=Amp-1
_PickedSet11, 1, 1
** Name: BC-2 Type: Displacement/Rotation
*Boundary, amplitude=newbcamp
_PickedSet12, 2, 2, 0.426
** Name: BC-3 Type: Displacement/Rotation
*Boundary, amplitude=Amp-1
_PickedSet13, 3, 3
** Name: BC-4 Type: Displacement/Rotation
*Boundary, amplitude=Amp-1
_PickedSet14, 4, 4
** Name: BC-5 Type: Displacement/Rotation
*Boundary, amplitude=Amp-1
_PickedSet15, 5, 5
** Name: BC-6 Type: Displacement/Rotation
*Boundary, amplitude=Amp-1
_PickedSet16, 6, 6
** Name: BC-7 Type: Symmetry/Antisymmetry/Encastre
*Boundary
_PickedSet17, ENCASTRE
```

Figure 3.33: ABAQUS input of the TMF cyclic loading boundary conditions.

TMF Cyclic Loading Specimen Model Amplitude

The TMF cyclic loading experiment was simulated by applying the specified amplitude to the boundary conditions above. Thus, in TMF cyclic loading tests, the specimen is displaced in two directions for one cycle. In this case, the strain rate is R1, and the duration of a half-cycle is approximately 280 seconds; Figure 3.34 describes the amplitude applied to simulate this cyclic loading experiment. The total duration of the simulations is 4900 seconds, and represents nine stabilized cycles. The values in the first row include the latency (in seconds) to apply the boundary conditions. The values of -1 and .28 represent the maximum negative and positive displacements in relation to RP-1. The actual displacement is determined using a ramp function in which the displacement value is multiplied by a percentage derived from the minimum to maximum conditions of the “newbcamp” amplitude. The stress and strains are calculated for each increment of 0.1 seconds until the final time condition is met.

```
*Amplitude, name=newbcamp, time=TOTAL TIME
        0.,          0.,        140.,       0.28,        420.,         -1.,        700.,       0.28
      980.,         -1.,       1260.,       0.28,       1540.,         -1.,       1820.,       0.28
     2100.,         -1.,       2380.,       0.28,       2660.,         -1.,       2940.,       0.28
     3220.,         -1.,       3500.,       0.28,       3780.,         -1.,       4060.,       0.28
     4340.,         -1.,       4620.,       0.28,       4900.,         -1.
*Amplitude, name=newtempamp, time=TOTAL TIME
```

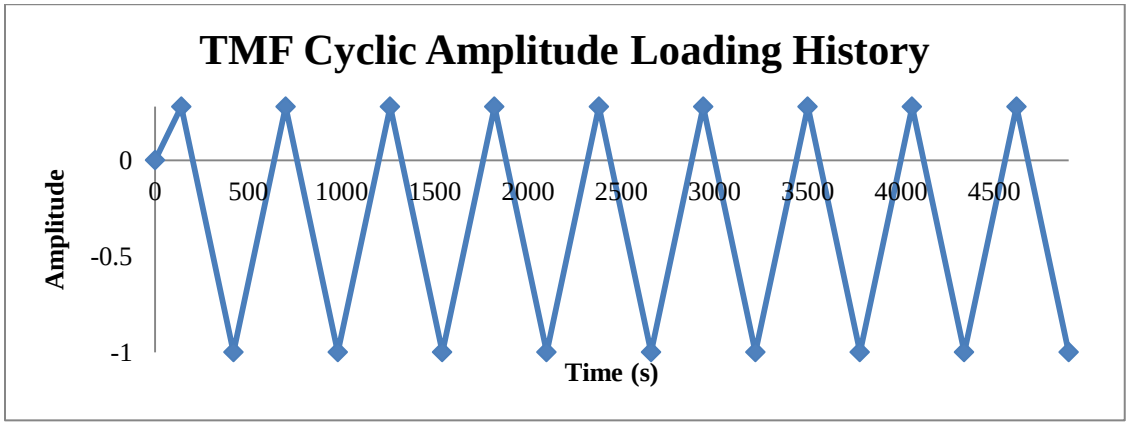

Figure 3.34: ABAQUS input for the TMF cyclic loading boundary condition amplitude.

TMF Cyclic Loading Specimen Model: Predefined Fields

A predefined field was used to apply a temperature field to each node as was also the case in the iso-thermal cyclic loading specimen simulations. A temperature of 300°C was applied to _PickedSet28, which comprises all nodes of the specimen model (Figure 3.35). The temperature was then multiplied using a ramp function defined by the amplitude function "newtempamp" (Figure 3.35), to vary the temperature between 150°C and 300°C, and replicate the TMF test.

```
** PREDEFINED FIELDS
**
** Name: Predefined Field-2   Type: Temperature
*Temperature, amplitude=newtempamp
_PickedSet28, 300.
```

Figure 3.35: ABAQUS input of the TMF cyclic loading predefined field for temperature variation.

TMF Cyclic Loading Specimen Model: Steps

To ensure that the material model was indeed stable, nine stabilized cycles were simulated. Consequently, there are 19 steps in the simulation of TMF cyclic loading plus one initial step. Each step represents a half-cycle of either the loading or unloading condition (depending on the specific step at that point in the simulation). For example, if a half-cycle lasted for 280 seconds

during the TMF cyclic loading experiment, the duration of one step of the simulation will also be 280 seconds. The processes (e.g. amplitude during each step) for the procedural steps are coordinated with specific time intervals, so that the appropriate loading and unloading displacements can be applied properly throughout the simulation. For example, the ABAQUS input file for step 2 is shown in Figure 3.36 to illustrate the simulation set-up procedure; necessary data for post-processing analyses, such as the logarithmic strain (LE) and the stress (S), are recorded.

Time Period: 280

Max. # of Increments: 10000

Initial Increment Size: 0.0001

Min. Increment Size: $1e^{-05}$

Maximum Increments Size:10

```
** ----------------------------------------------------------------
**
** STEP: Step-2
**
*Step, name=Step-2, nlgeom=YES, inc=10000
*Visco, cetol=0.01
0.0001, 280., 1e-05, 10.
**
** BOUNDARY CONDITIONS
**
** Name: BC-2 Type: Displacement/Rotation
*Boundary, amplitude=newbcamp
_PickedSet12, 2, 2, 0.18
**
** OUTPUT REQUESTS
**
*Restart, write, frequency=0
**
** FIELD OUTPUT: F-Output-1
**
*Output, field
*Node Output
NT, UT
*Element Output, directions=YES
EE, LE, PE, S, THE, PEEQ
**
** HISTORY OUTPUT: H-Output-1
**
*Output, history, variable=PRESELECT
*End Step
** ----------------------------------------------------------------
```

Figure 3.36: ABAQUS input of the TMF cyclic loading step sequence (Step 2).

3.5 Material Model Validation

3.5.1 Monotonic Loading Material Model Validation

The methods used to determine the mechanical material properties were presented in previous sections of this chapter; in this section the experimental results obtained during testing of actual specimens are compared to the results obtained from the simulation of these experimental conditions applied to model specimens in order to validate the material models for monotonic loading, isothermal cyclic loading, and TMF cyclic loading conditions. In this section,

comparisons of the σ–ε curves obtained from testing and simulation are presented for all temperatures and strain rates. In general, the simulation σ and ε results did not emulate the experimental observations as well at higher temperatures (i.e., for temperatures ≥ 250°C), as at lower temperatures. Perhaps at higher temperatures viscous effects are becoming more predominate and the simulation material model does not capture this phenomenon. Alternatively, perhaps this apparent trend is due to sampling error, in which the experimental results were somewhat inconsistent for some tests, (e.g. transient or fluctuating readings).

Comparison of Monotonic Loading Experimental and Simulation Results for R1

Figure 3.37 through Figure 3.41 compare the simulation results to the experimental observations at the R1 strain rate at the indicated temperatures. In general, the model's findings are fairly accurate for the R1 strain rate; however, differences between the simulation results and experimental observations are evident under high temperature conditions (≥250°C; Figures 3.40 and 3.41). The validity of the monotonic loading material model for the conditions studied in this thesis is examined using a percent error comparison in Section 3.5.2.

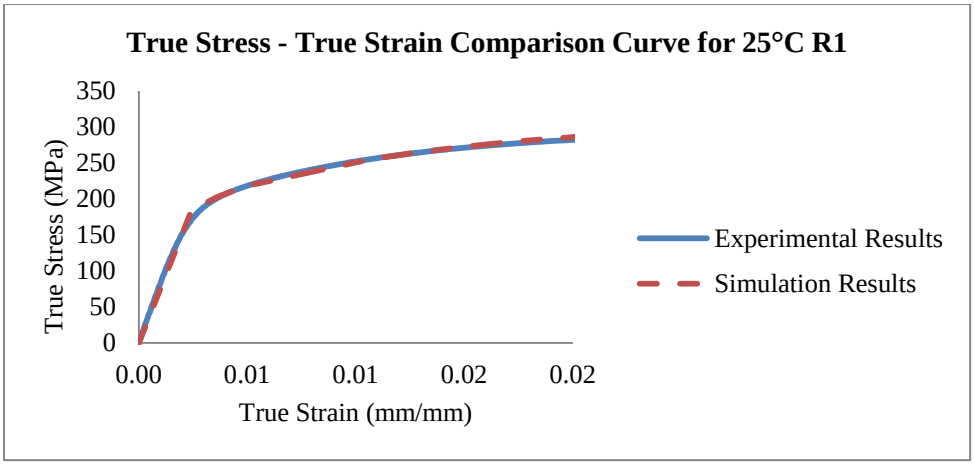

Figure 3.37: Comparison of monotonic loading experimental and simulation results for 25°C at R1.

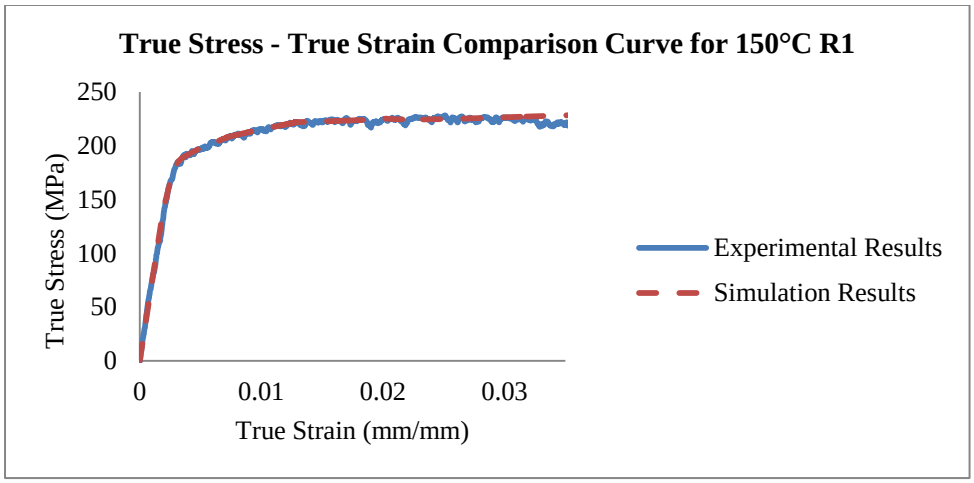

Figure 3.38: Comparison of monotonic loading experimental and simulation results for 150°C at R1.

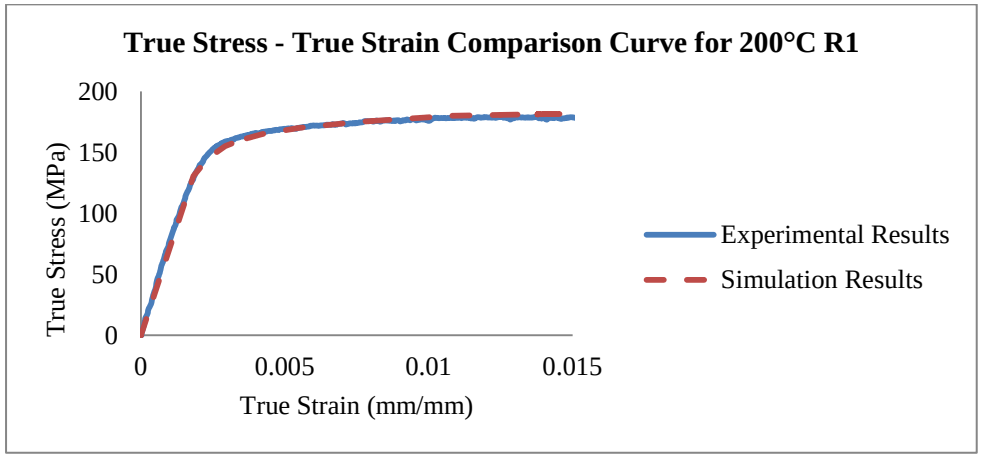

Figure 3.39: Comparison of monotonic loading experimental and simulation results for 200°C at R1.

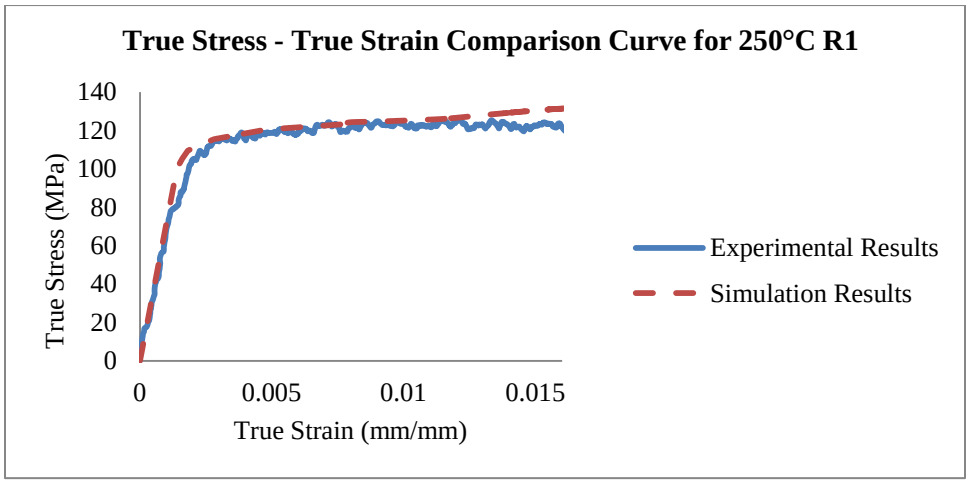

Figure 3.40: Comparison of monotonic loading experimental and simulation results for 250°C at R1.

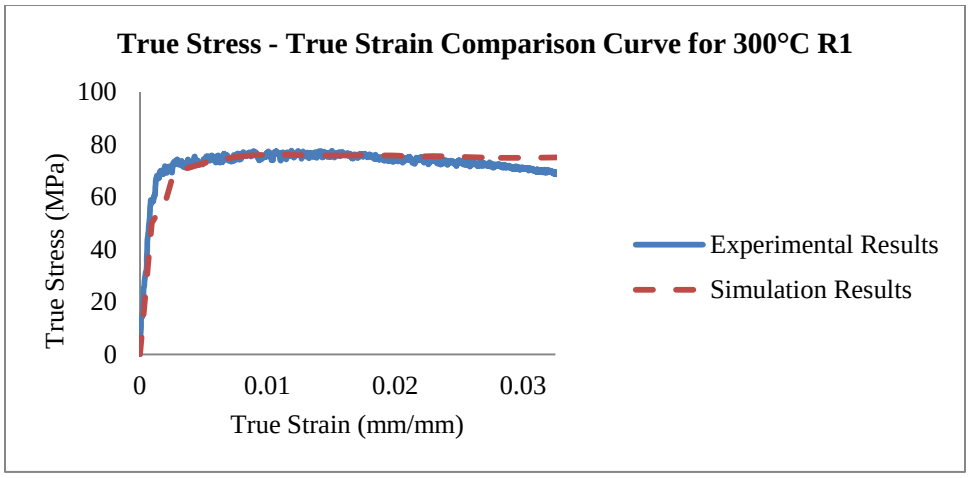

Figure 3.41: Comparison of monotonic loading experimental and simulation results for 300°C at R1.

Comparison of Monotonic Loading Experimental and Simulation Results for R2

Figure 3.42 through Figure 3.46 compare the simulation and the experimental results obtained for the R2 strain rate at various temperatures. The experimental results obtained under these conditions are highly consistent with the simulation model's outcomes; thus, the material model developed for monotonic loading at R2 appears to be acceptable for all of the temperatures considered.

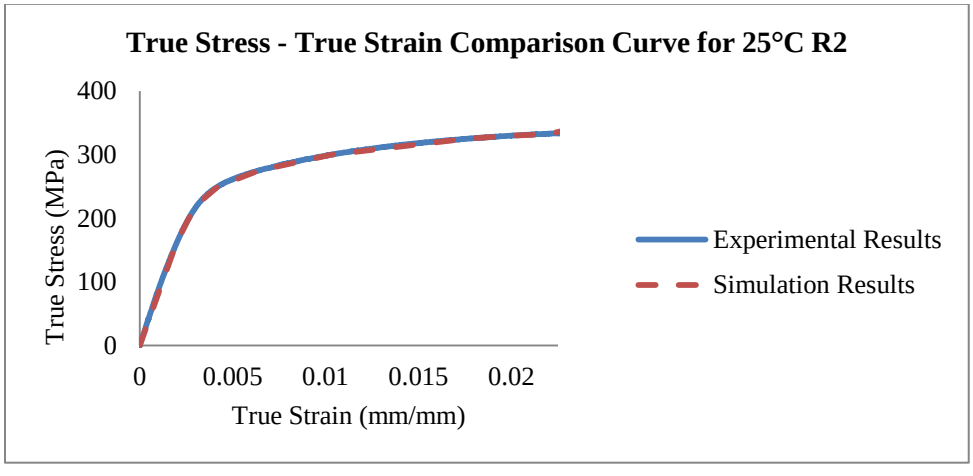

Figure 3.42: Comparison of monotonic loading experimental and simulation results for 25°C at R2.

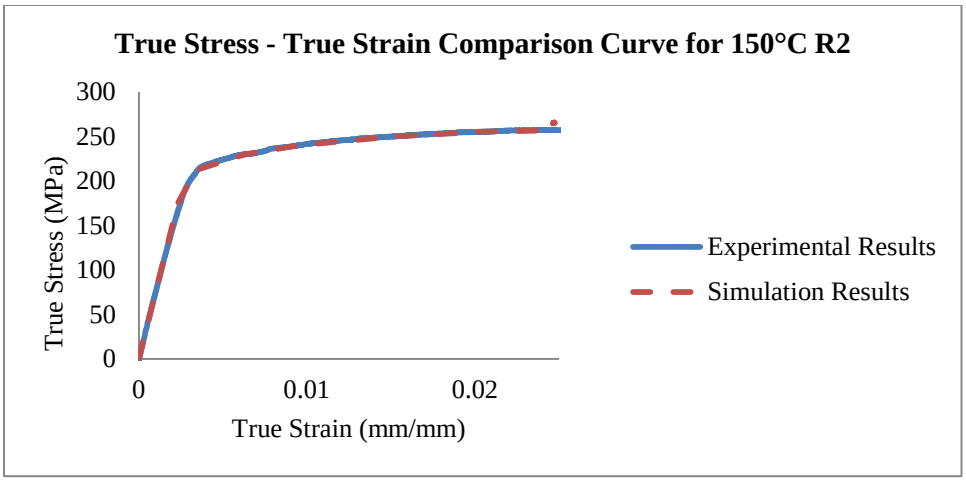

Figure 3.43: Comparison of monotonic loading experimental and simulation results for 150°C at R2.

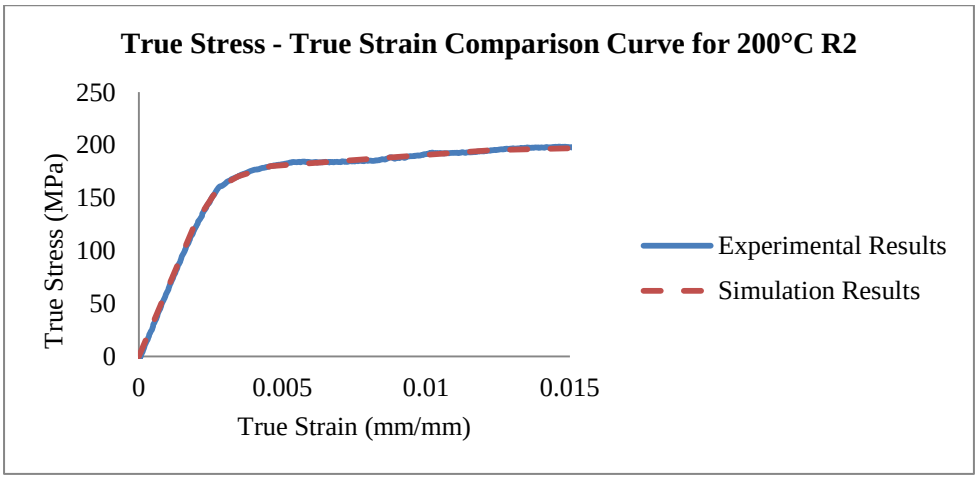

Figure 3.44: Comparison of monotonic loading experimental and simulation results for 200°C at R2.

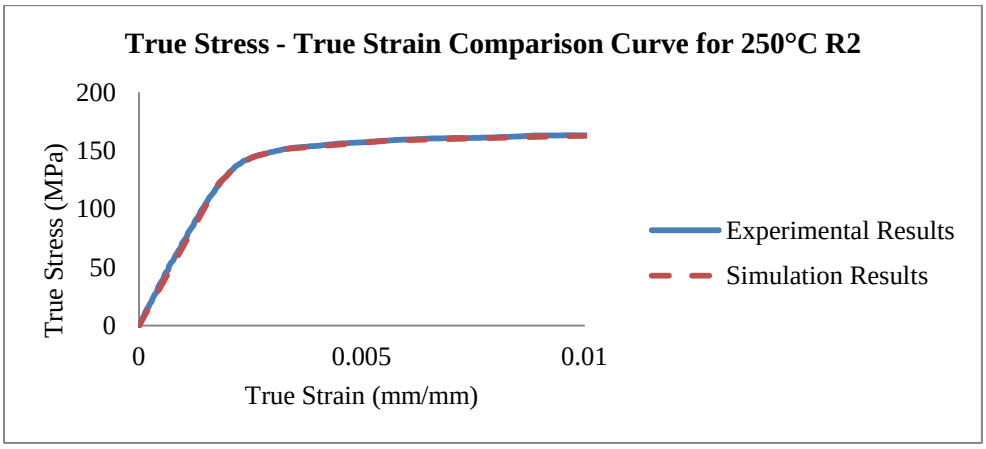

Figure 3.45: Comparison of Monotonic loading experimental and simulation results for 250°C at R2.

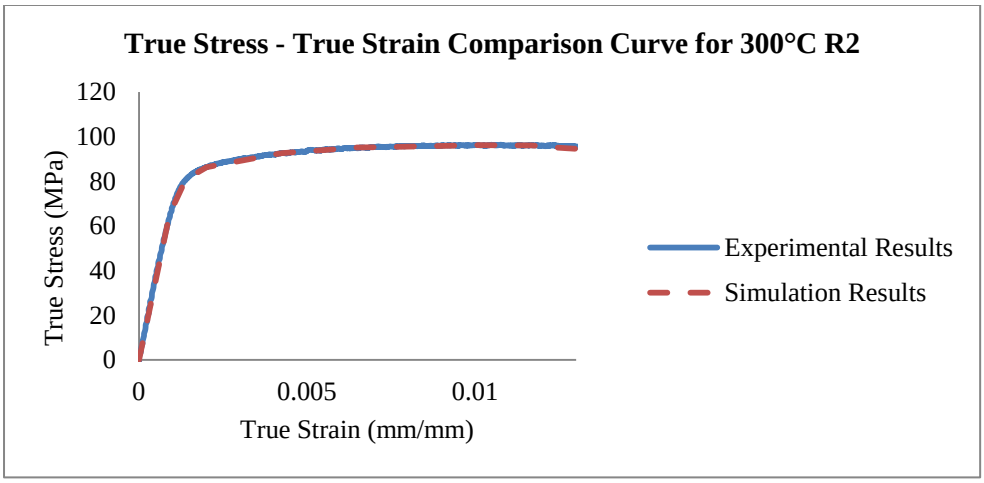

Figure 3.46: Comparison of monotonic loading experimental and simulation results for 300°C at R2.

Comparison of Monotonic Loading Experimental and Simulation Results for R3

Figure 3.47 through Figure 3.51 compare the simulation and the experimental results for the R3 strain rate at various temperatures. In this case (R3), the simulation results for the monotonic loading material model were consistent with the experimental observations, with the exception of the high temperature (300°C) condition (Figure 65). The experimental results obtained at this temperature fluctuated markedly, and measurements varied more than at lower temperatures.

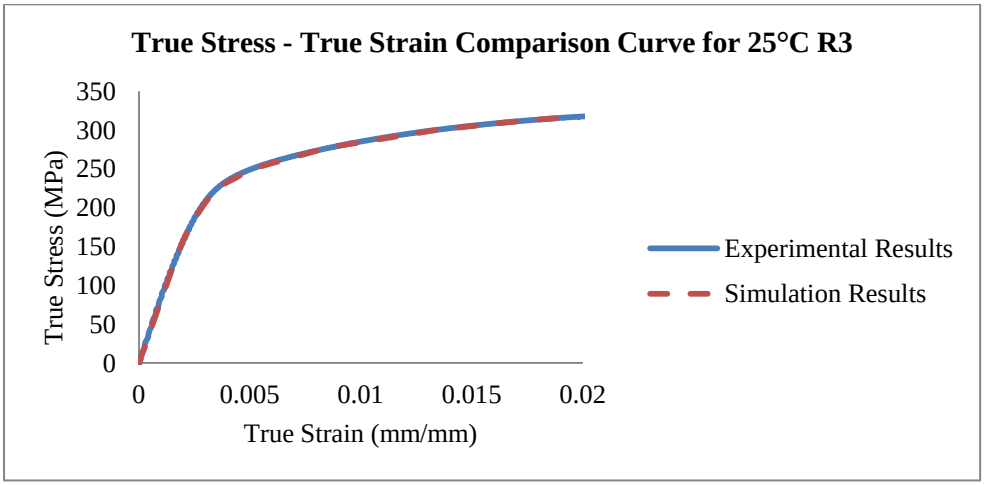

Figure 3.47: Comparison of monotonic loading experimental and simulation results for 25°C at R3.

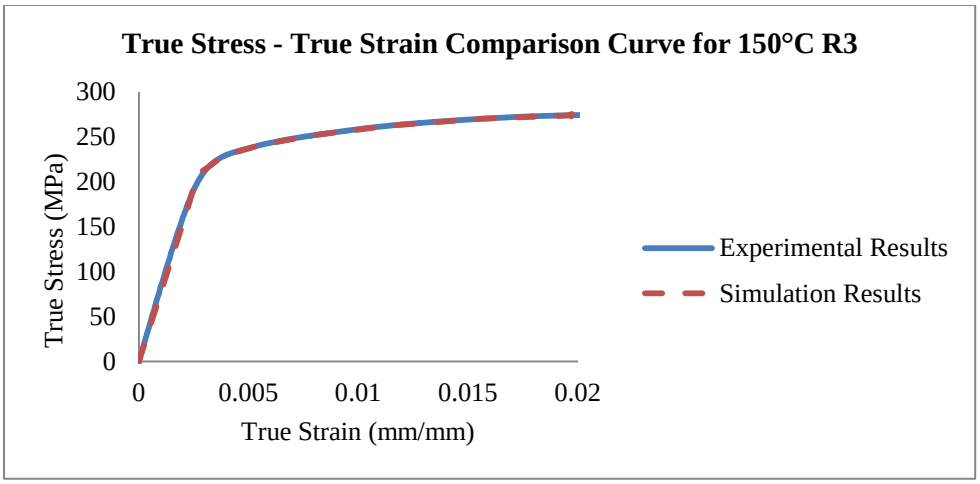

Figure 3.48: Comparison of monotonic loading experimental and simulation results for 150°C at R3.

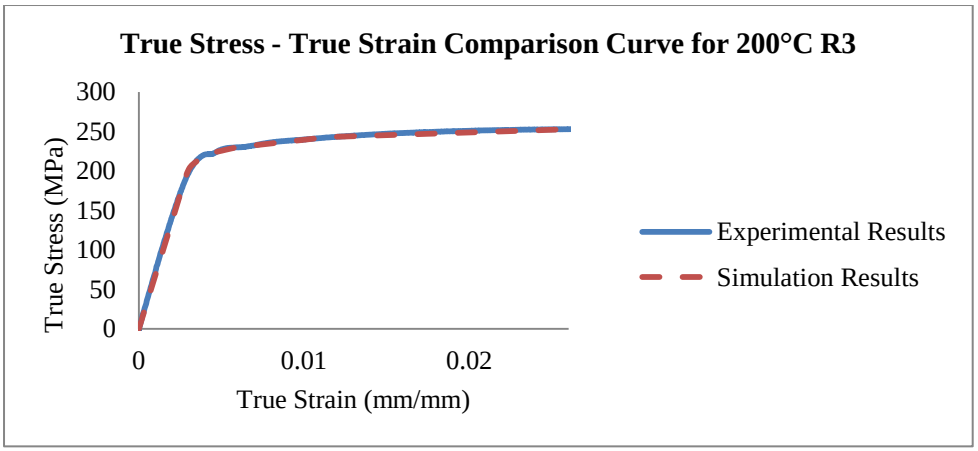

Figure 3.49: Comparison of monotonic loading experimental and simulation results for 200°C at R3.

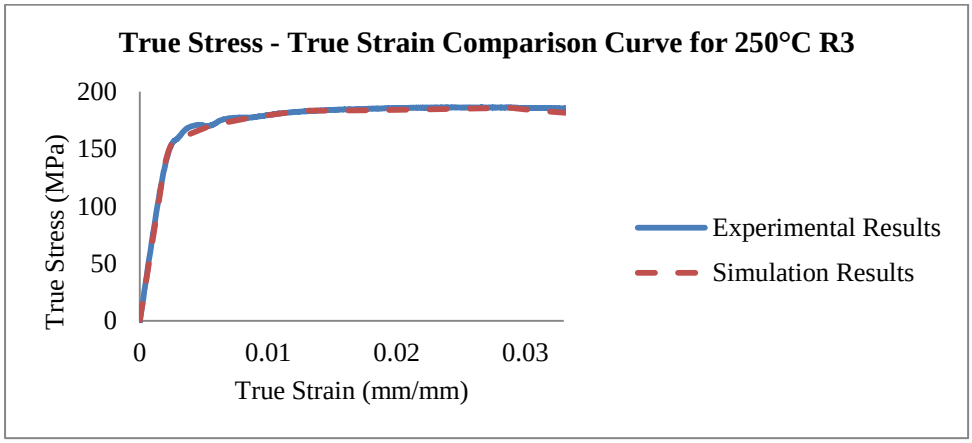

Figure 3.50: Comparison of monotonic loading experimental and simulation results for 250°C at R3.

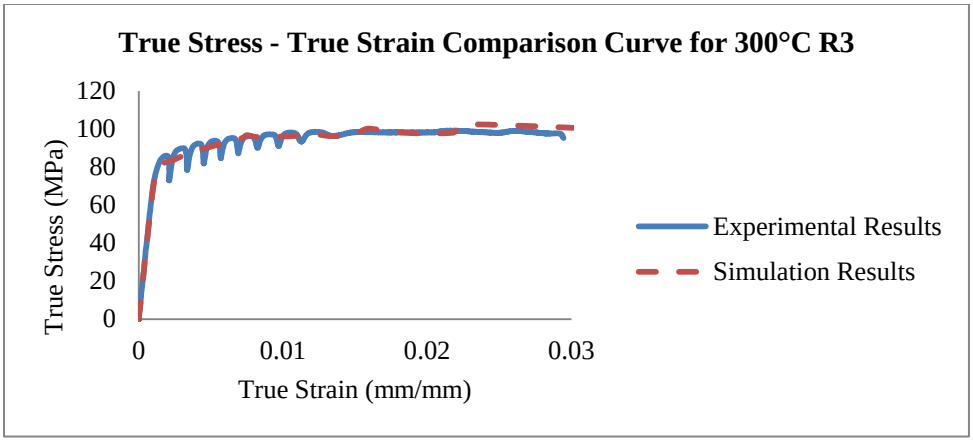

Figure 3.51: Comparison of monotonic loading experimental and simulation results for 300°C at R3.

3.5.2 Monotonic Loading Material Model Experimental and Simulation Comparison Results

The monotonic material model was validated by approximating the area under all of the monotonic loading σ-ε curves using the MATLAB trapezoidal rule function. The integrated increment was set to the MATLAB default (between each data point). In all conditions, the percent error due to discrepancies between the simulation results and the test results was low, which suggests that the monotonic loading material model accurately describes the actual material properties of the test specimens; in fact, the percent error was <5% for all conditions, including the high temperature conditions noted previously. The following tables (Table 3.7 - Table 3.9) contain information used to validate the monotonic loading material model. As noted previously, some high temperature conditions resulted in larger discrepancies between the monotonic σ-ε curves generated from test data or simulation results (Figures 3.37 to 3.51).

Table 3.7: Comparison of monotonic loading experimental and simulation outcomes (% error at R1 for various temperatures)

R1 Monotonic Loading % Error Comparison			
Temperature (°C)	**Simulation Area (J/mm^3)**	**Experimental Area (J/mm^3)**	**% Error**
25	4.6351	4.6339	0.026
150	7.3406	7.3013	0.538
200	2.3076	2.3072	0.017
250	1.7383	1.6648	4.415
300	2.4563	2.4465	0.401

Table 3.8: Comparison of monotonic loading experimental and simulation outcomes (% error at R2 for various temperatures)

R2 Monotonic Loading % Error Comparison			
Temperature (°C)	**Simulation Area (J/mm^3)**	**Experimental Area (J/mm^3)**	**% Error**
25	6.1732	6.2631	1.435
150	5.6298	5.7079	1.368
200	2.5315	2.5248	0.265
250	1.3903	1.3994	0.650
300	1.1511	1.1552	0.355

Table 3.9: Comparison of monotonic loading experimental and simulation outcomes (% error at R3 for various temperatures)

R3 Monotonic Loading % Error Comparison			
Temperature (°C)	**Simulation Area (J/mm^3)**	**Experimental Area (J/mm^3)**	**% Error**
25	5.2139	5.2081	0.111
150	4.6022	4.6064	0.091
200	5.8477	5.9049	0.969
250	5.6769	5.7685	1.588
300	2.6505	2.7608	3.995

3.5.3 Iso-thermal Cyclic Loading Material Model Validation

Comparing Stabilized Iso-thermal Cyclic Loading Hysteresis Loops

Validation of the combined hardening material model used to simulate isothermal cyclic loading test is described in this section. The validation procedures involve comparison of the amount of

energy dissipated during stabilized loading cycles based on experimental and simulated isotheral cyclic loading tests. The following figures (Figure 3.52 to Figure 3.66) compare the experimental and simulated outcomes (i.e., stabilized hysteresis loops at strain amplitudes of 0.005, 0.004, or 0.003mm/mm) obtained under several iso-thermal conditions (25 to 300°C); the applied strain rate was R1.

Iso-thermal Cyclic Loading Comparisons of stabilized hysteresis loops obtained for experimental and simulated tests of R1 for a strain amplitude of 0.005 mm/mm

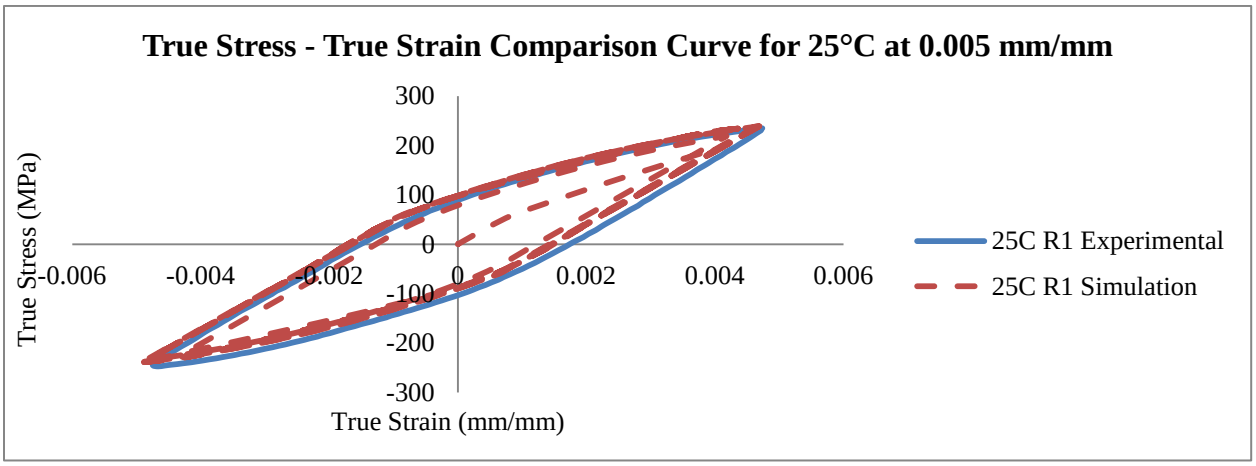

Figure 3.52: Comparison of cyclic loading experimental and simulation results for 25°C at 0.005 mm/mm

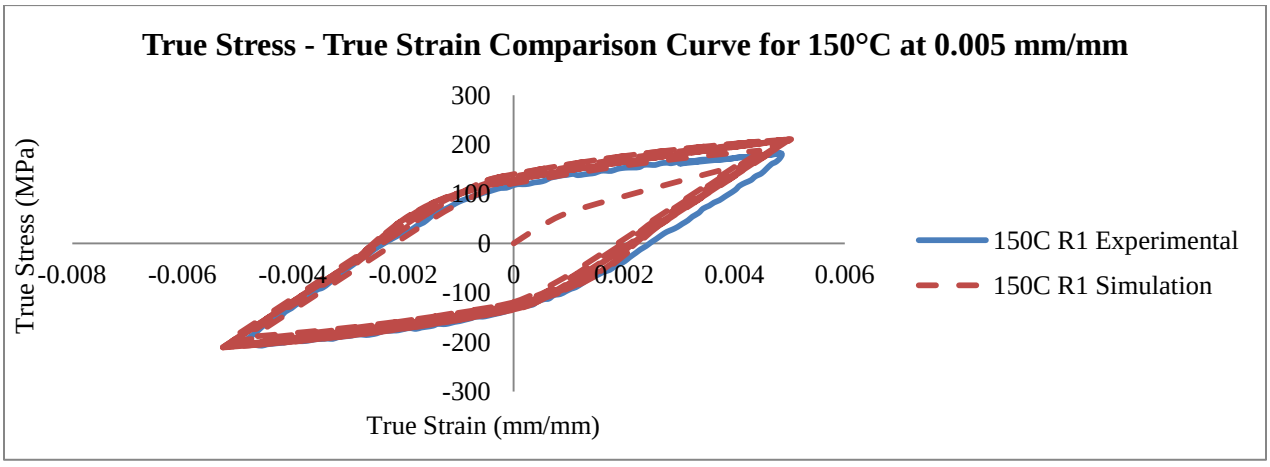

Figure 3.53: Comparison of cyclic loading experimental and simulation results for 150°C at 0.005 mm/mm

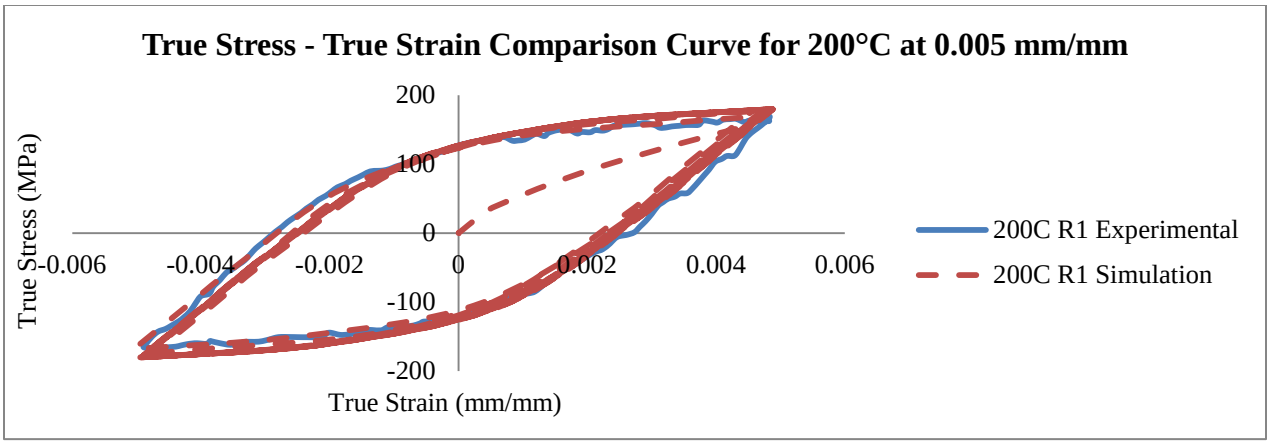

Figure 3.54: Comparison of cyclic loading experimental and simulation results for 200°C at 0.005 mm/mm

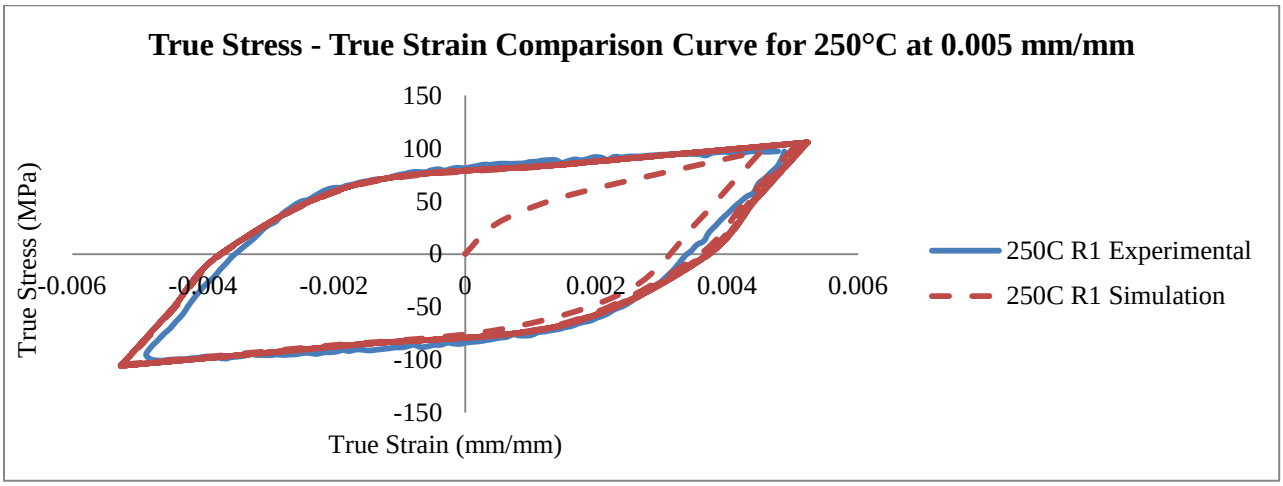

Figure 3.55: Comparison of cyclic experimental and simulation results for 250°C at 0.005 mm/mm

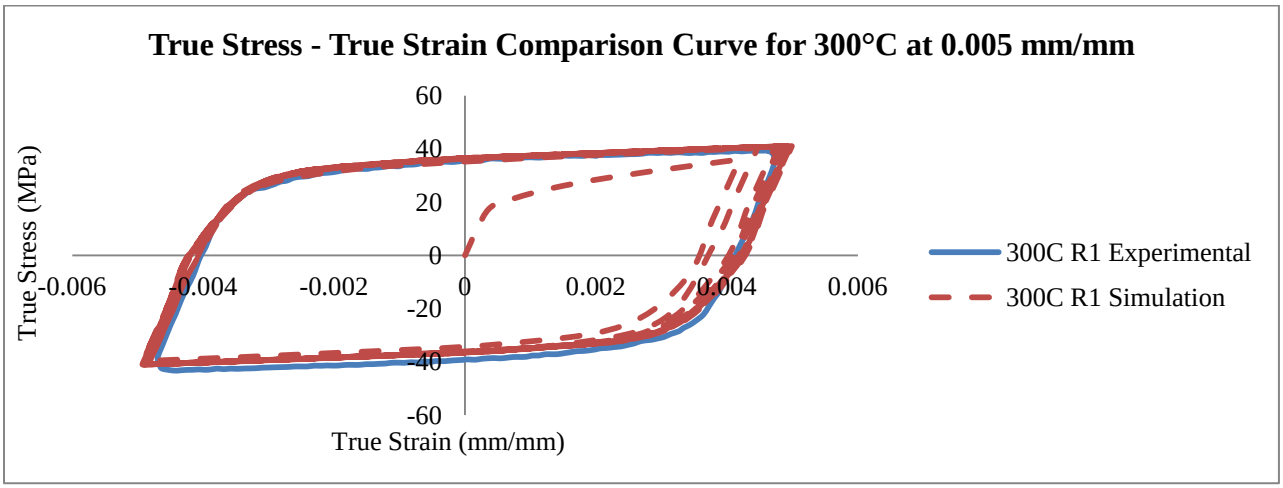

Figure 3.56: Comparison of cyclic experimental and simulation results for 300°C at 0.005 mm/mm

Iso-thermal Cyclic Loading Comparison Comparisons of stabilized hysteresis loops obtained for experimental and simulated tests of R1 for a strain amplitude of 0.004 mm/mm

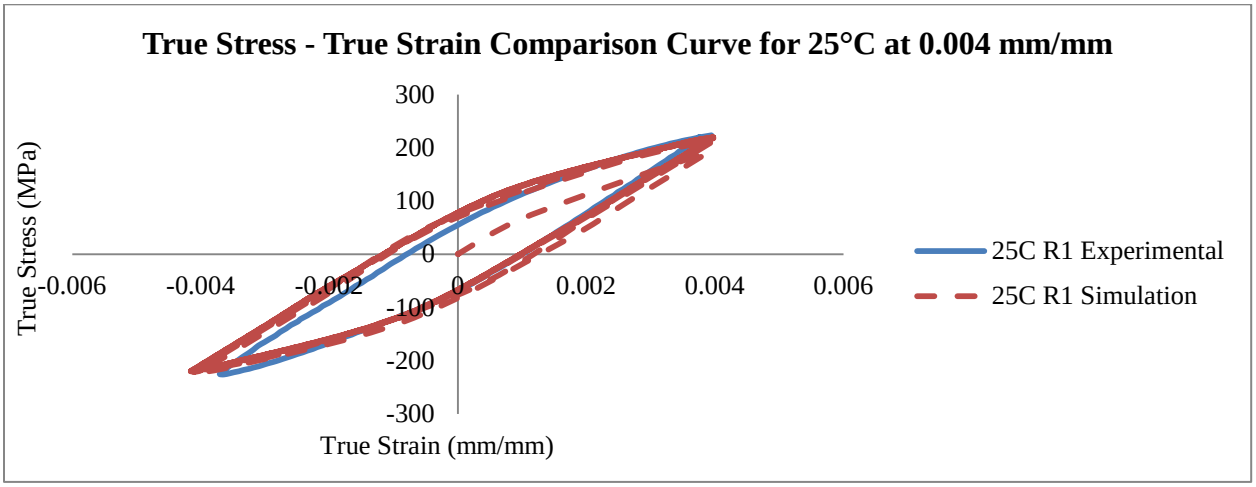

Figure 3.57: Comparison of cyclic loading experimental and simulation results for 25°C at 0.004 mm/mm

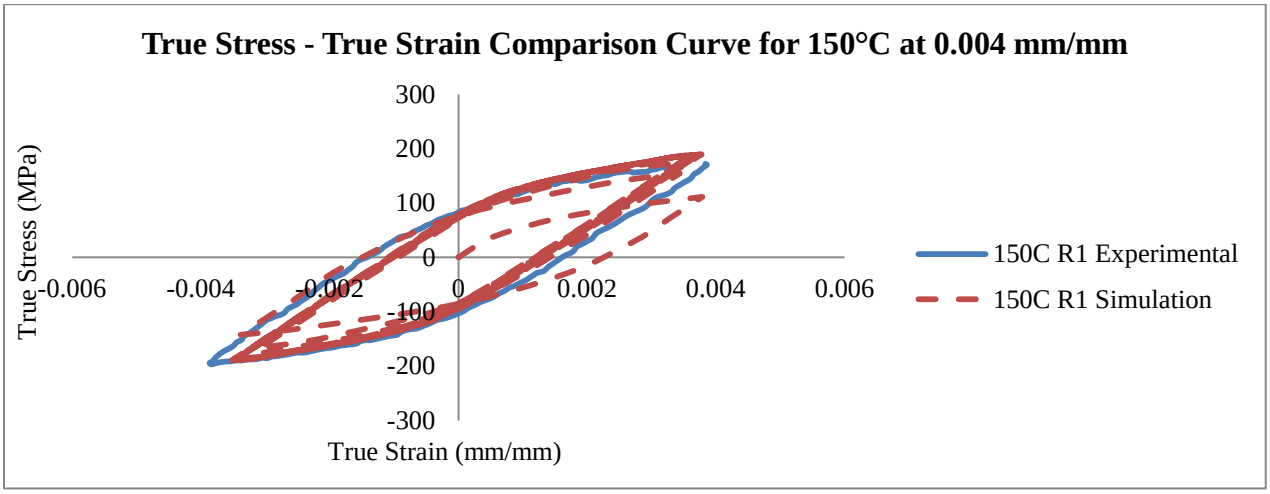

Figure 3.58: Comparison of cyclic loading experimental and simulation results for 150°C at 0.004 mm/mm

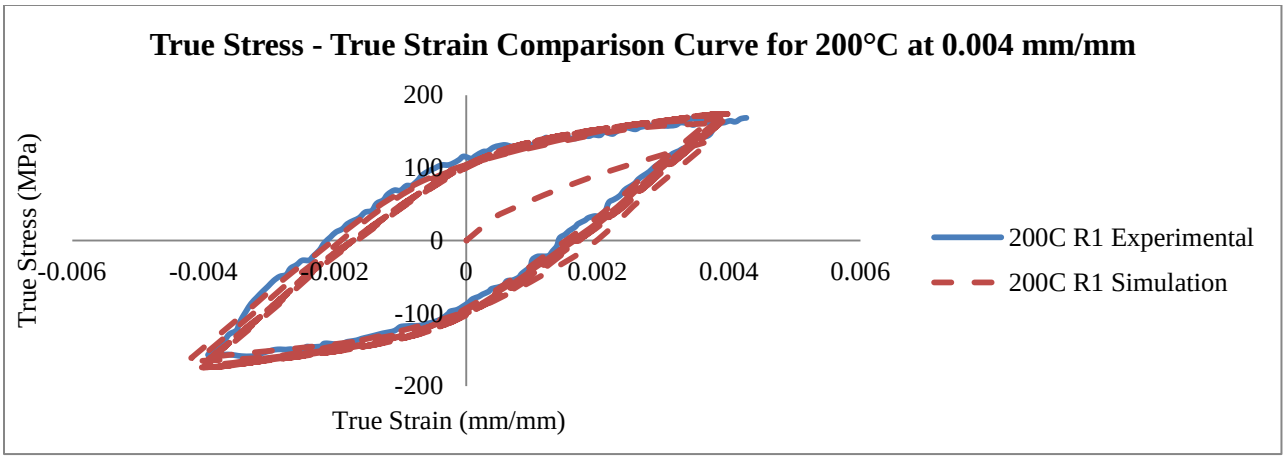

Figure 3.59: Comparison of cyclic loading experimental and simulation results for 200°C at 0.004 mm/mm

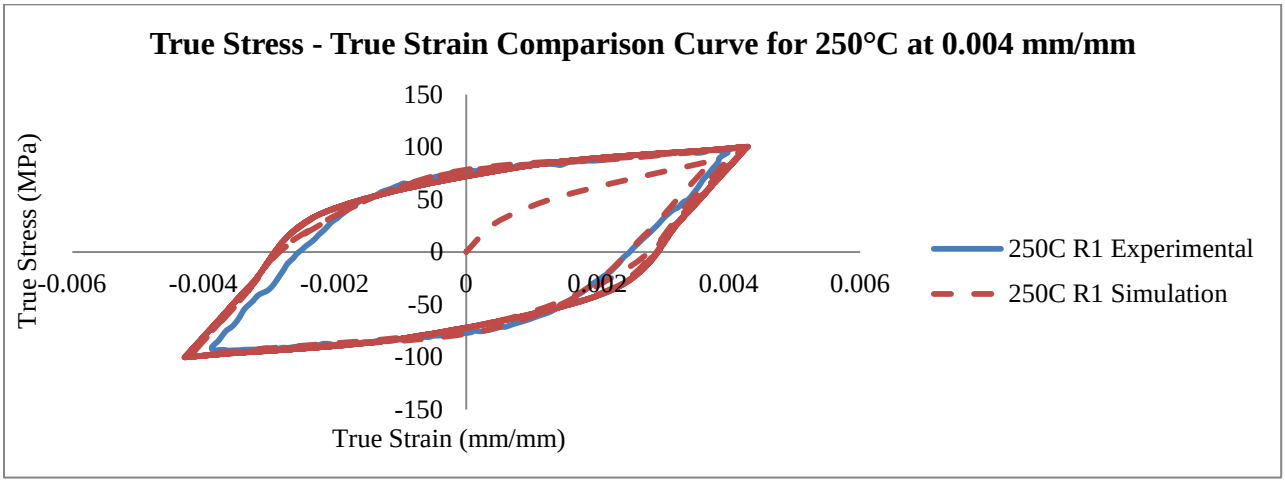

Figure 3.60: Comparison of cyclic loading experimental and simulation results for 250°C at 0.004 mm/mm

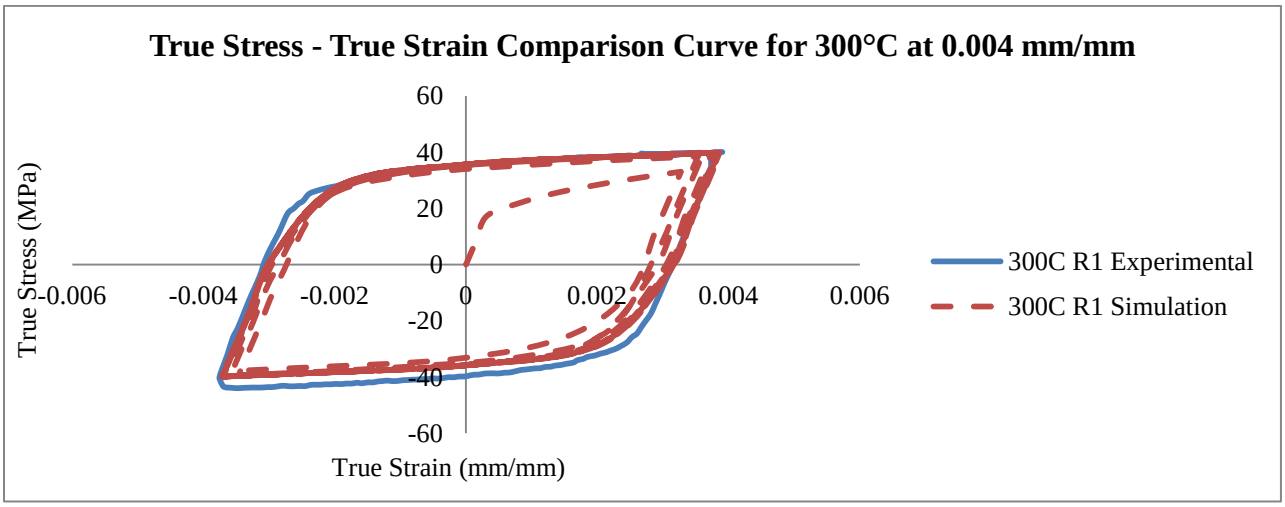

Figure 3.61: Comparison of cyclic loading experimental and simulation results for 300°C at 0.004 mm/mm

Iso-thermal Cyclic Loading Comparisons of stabilized hysteresis loops obtained for experimental and simulated tests of R1 for a strain amplitude of 0.003 mm/mm

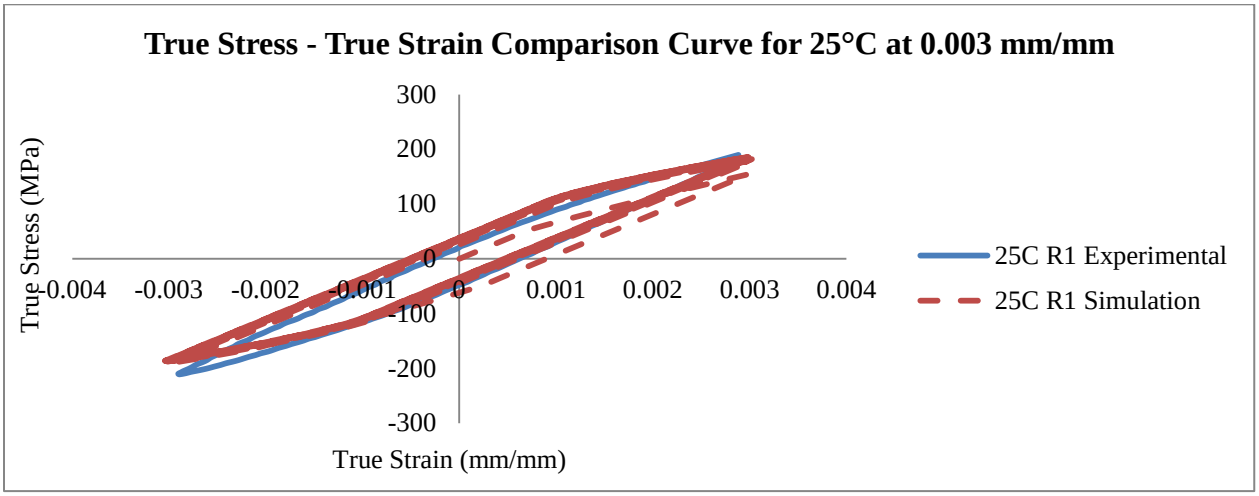

Figure 3.62: Comparison of cyclic loading experimental and simulation results for 25°C at 0.003 mm/mm

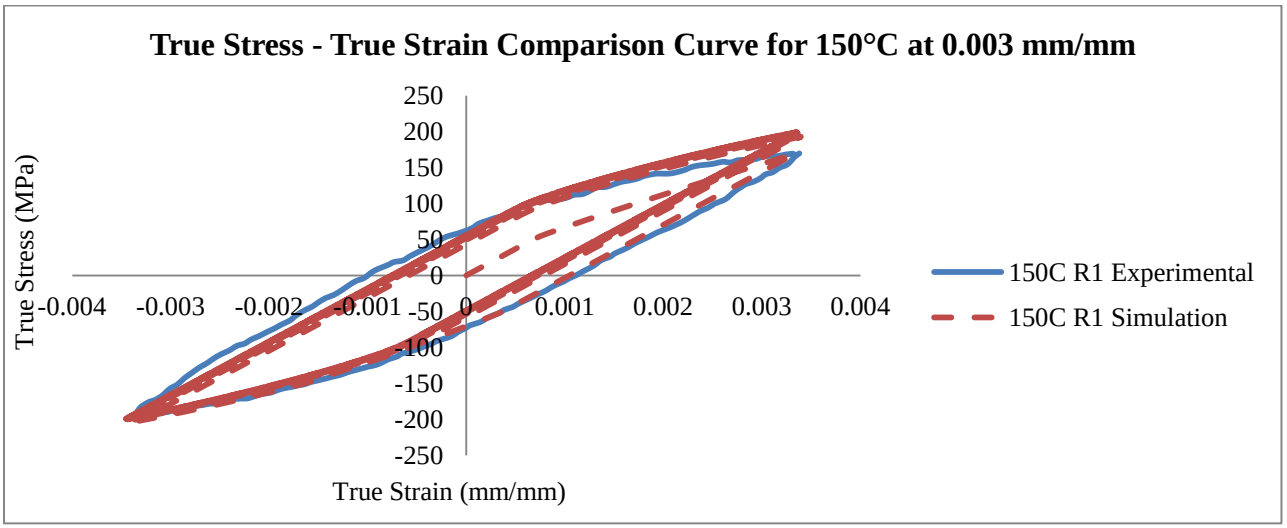

Figure 3.63: Comparison of cyclic loading experimental and simulation results for 150°C at 0.003 mm/mm

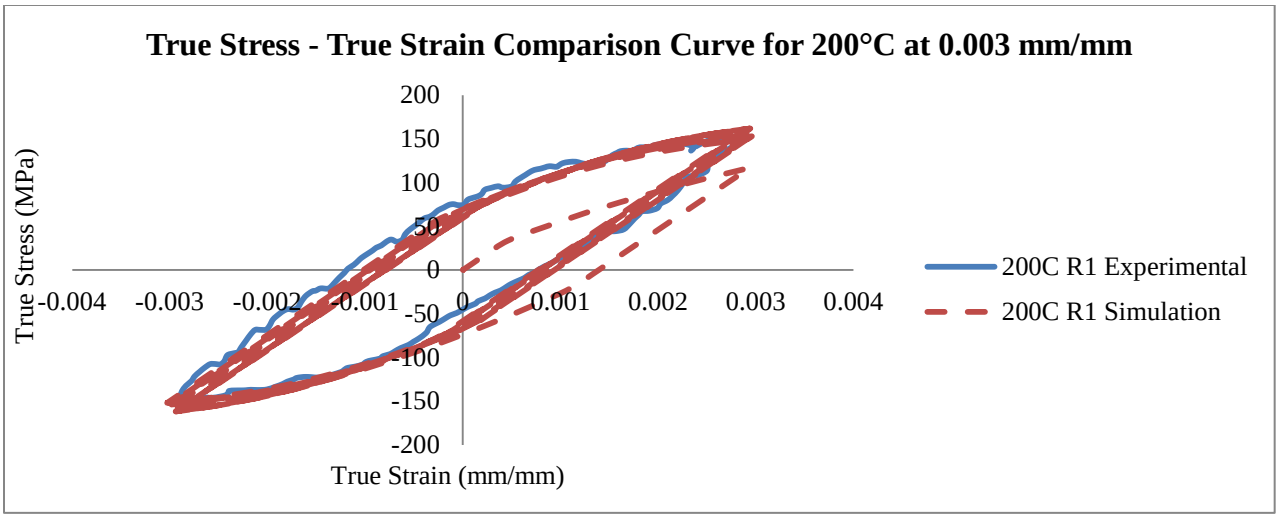

Figure 3.64: Comparison of cyclic loading experimental and simulation results for 200°C at 0.003 mm/mm

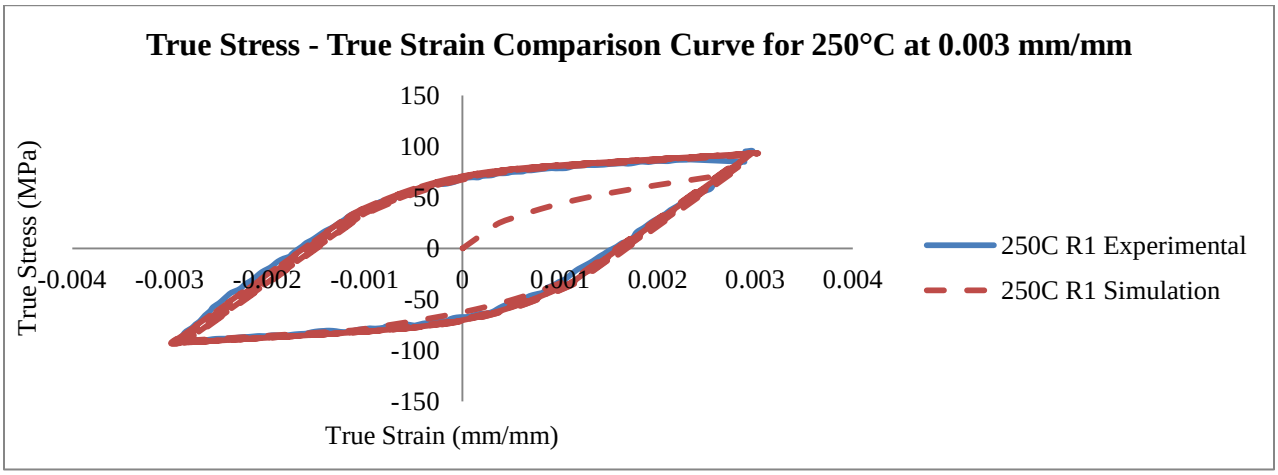

Figure 3.65: Comparison of cyclic loading experimental and simulation results for 250°C at 0.003 mm/mm

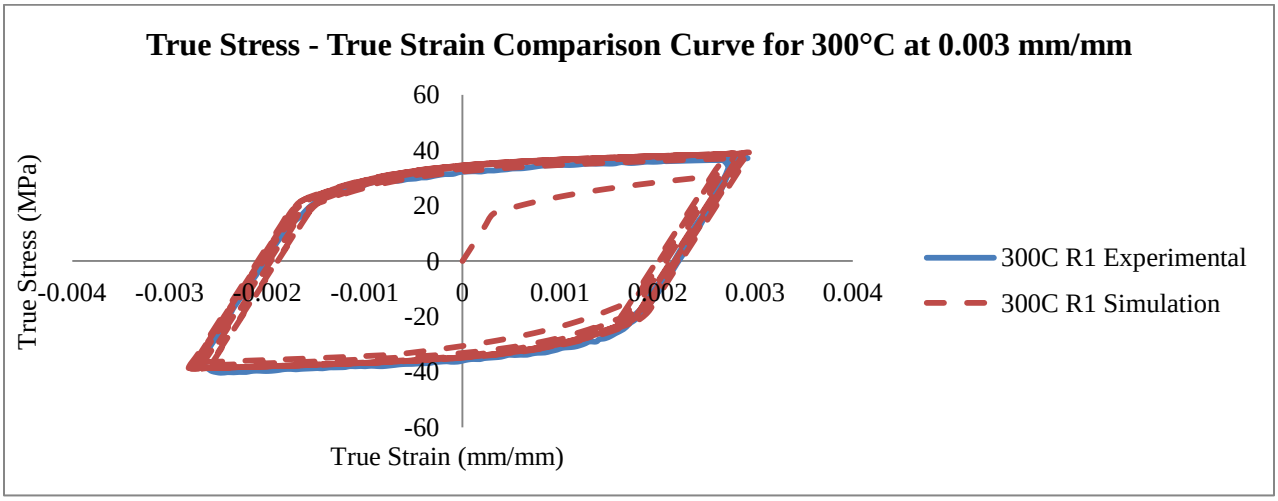

Figure 3.66: Comparison of cyclic loading experimental and simulation results for 300°C at 0.003 mm/mm

Iso-thermal Cyclic Loading Model Validation based on Hysteresis Loop Area

Visual comparisons of all of the hysteresis loops (generated from experimental and simulated tests) for the conditions studied in this thesis are presented above (Figure 3.52 to Figure 3.66); a comparison of the dissipated energy from these hysteresis loops follows. Comparing the dissipated energy of one stabilized hysteresis loop derived from experimental observations to the dissipated energy from the corresponding simulation allows for more precise validation of the combined hardening material model developed to emulate the isothermal cyclic loading tests presented in this thesis. The following tables (Table 3.10, Table 3.11, and Table 3.12) contain details about the parameters used to calculate the area of the stabilized cycle for each condition (experimental and simulated), including comparison of the magnitude of differences found between the experimental and simulated results (area % error) for the conditions examined. The area within a stabilized hysteresis loop was calculated using Equation 2.24.

In order to apply the dissipated energy approximation proposed by Skelton (Equation 2.24) the cyclic strength coefficient (*k'*) and cyclic strain hardening exponent (*n'*) must be calculated. These measures were determined in a similar fashion to the comparable monotonic loading calculations described previously (Equation 3.21); the function used to calculate these measures for isothermal cyclic loading conditions is shown in Equation 3.22.

$$\frac{\sigma}{2} = k'\left(\frac{\varepsilon}{2}\right)^{n'} \qquad \textit{Equation 3.22}$$

The variables in Equation 3.22 are defined as follows: σ is the cyclically stable true stress amplitude, *k'* is the cyclic strength hardening coefficient, ε is the cyclically stable true strain, and *n'* is the cyclic strain hardening exponent. The values calculated for *n'* at R1 for all temperature

conditions and strain amplitudes investigated are shown in Table 3.10, Table 3.11, and Table 3.12.

Table 3.10: Comparison of cyclic loading experimental and simulation stabilized hysteresis loops (area % error) at R1 for 0.005 mm/mm

Strain Amplitude									
0.005									
Temperature	Simulation				Experimental				Area % Error
	$\Delta\sigma$	$\Delta\varepsilon_p$	n'	Area (J/mm^3)	$\Delta\sigma$	$\Delta\varepsilon_p$	n'	Area (J/mm^3)	
25°C	480.49	0.0033	0.35	1.17	482.6	0.0032	0.36	1.13	3.54
150°C	404.6	0.0041	0.17	1.42	389.31	0.0047	0.16	1.58	10.13
200°C	359.93	0.005	0.13	1.58	338.03	0.0057	0.13	1.69	6.51
250°C	211.26	0.0072	0.25	1.22	197.88	0.0071	0.2	1.17	4.27
300°C	82.03	0.0081	0.13	0.59	82.59	0.0082	0.1	0.61	3.28

Table 3.11: Comparison of cyclic loading experimental and simulation stabilized hysteresis loops (area % error) at R1 for 0.004 mm/mm

Strain Amplitude									
0.004									
Temperature	Simulation				Experimental				Area % Error
	$\Delta\sigma$	$\Delta\varepsilon_p$	n'	Area (J/mm^3)	$\Delta\sigma$	$\Delta\varepsilon_p$	n'	Area (J/mm^3)	
25°C	439.29	0.0022	0.36	0.71	447.97	0.0021	0.3762	0.6884	3.14
150°C	378.43	0.0024	0.23	0.74	368.97	0.003	0.2369	0.8883	16.69
200°C	348.84	0.0036	0.15	1.1	327.74	0.0038	0.1452	1.0984	0.15
250°C	200.58	0.0055	0.13	0.98	190.65	0.0053	0.1206	0.8985	9.07
300°C	79.66	0.0061	0.08	0.45	83.96	0.0062	0.0792	0.4831	6.85

Table 3.12: Comparison of cyclic loading experimental and simulation stabilized hysteresis loops (area % error) at R1 for 0.003 mm/mm

Strain Amplitude									
0.003									
Temperature	**Simulation**				**Experimental**				**Area % Error**
	$\Delta\sigma$	**$\Delta\varepsilon_p$**	***n'***	**Area (J/mm^3)**	**$\Delta\sigma$**	**$\Delta\varepsilon_p$**	***n'***	**Area (J/mm^3)**	
25°C	371.97	0.00098	0.5	0.24	400.59	0.00088	0.5251	0.23	4.35
150°C	398.22	0.0016	0.25	0.51	362.19	0.0021	0.2365	0.61	16.39
200°C	304.89	0.0019	0.19	0.5	297.63	0.002	0.2055	0.48	4.17
250°C	186.3	0.0032	0.08	0.56	185.19	0.0033	0.0874	0.55	1.82
300°C	77.64	0.0043	0.04	0.32	77.43	0.0042	0.0434	0.31	3.23

The discrepancy between the experimental outcomes and the outcomes of the model simulation (area percent error) is relatively low (<10%) for most of the conditions. However, for the 150°C condition the area percent error was higher (ranging from 10.13 to 16.69%) than the level of error observed for the other temperature conditions; this was the case for all of the strain amplitudes examined. This indicates that the material model does not reliably replicate the results for this isothermal temperature condition, but the model does seem to simulate the findings for the other temperature conditions examined (i.e., for temperatures lower and higher than 150°C) quite well. This is most evident in Table 3.12 (strain amplitude of 0.003 mm/mm), which shows that the amount of error at 150°C (16.39%) is markedly greater (3.8 to 9 times larger) than the area percent error found for other temperatures (error levels ranging from 1.82 to 4.35%). Nevertheless, for all of the other isothermal temperature and amplitude conditions examined, the percent error is low (ranging from 0.15 to 9.07%), and is considered to fall within acceptable limits. Thus, the isothermal cyclic loading material model for R1 is considered to be acceptable, and can now be used for fatigue life predictions.

In-Phase (IP) TMF Cyclic Loading Material Model Validation

The same procedures were used to validate the IP TMF cyclic loading material model (using hysteresis loops) as were employed for validation of the isothermal cyclic loading material model. The hysteresis loop obtained for experimental results for R1 was compared to the corresponding simulated hysteresis loop visually (using a σ-ε plot), and by determining the percent error between the energy dissipation calculations for these loops. Figure 3.67 presents the visual comparison of the experimental and simulated hysteresis loops. The thermal load applied to the experimental and simulated specimens ranged between 150°C and 300°C. The temperature was 300°C at the location of maximum strain, and was 150°C at the location of minimum strain.

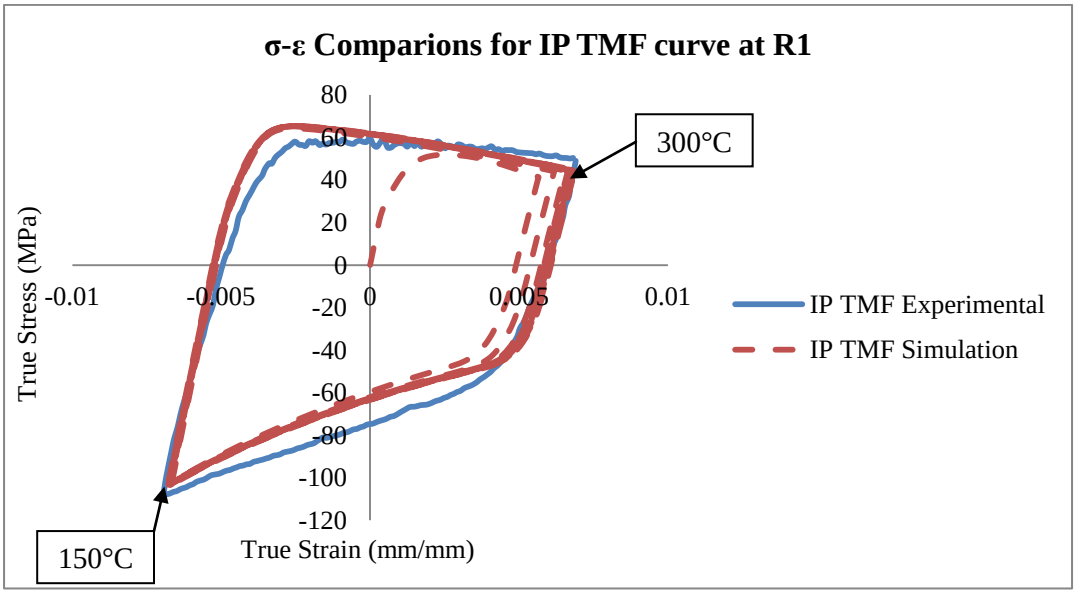

Figure 3.67: Comparison of IP TMF cyclic loading experimental and simulation results at R1

To determine the amount of energy dissipated by the hysteresis loops, the same method developed by Skelton was used as in the isothermal cyclic loading studies. The cyclic strain hardening exponent (n) is required for the calculation of the area within the hysteresis loop that represents dissipated energy. After the cyclic strain hardening exponents (n) for the

experimental and simulation findings were calculated as 0.249 and 0.245 for the experimental and simulation curves, respectively, the area representing energy dissipated by the hysteresis loops was determined (Table 3.13). Table 3.13 also shows the percent error difference found for the energy dissipated by the experimental and simulated hysteresis loops. The percent error difference between the two curves is low (1.28%), indicating that the simulation results from the IP TMF material model are consistent with the experimental observations.

Table 3.13: Comparison of experimental and simulated IP TMF energy dissipation values and % error material model validation

IP TMF % Error Material Model Validation	
Experimental Area (J/mm^3)	1.481
Simulated Area (J/mm^3)	1.462
Percent Error (%)	
1.28	

3.6 Calibration of Damage Model Parameters

3.6.1 Calibration of Basquin-Manson-Coffin Parameters

In order to apply the Basquin-Manson-Coffin damage model, the following parameters need to be determined: fatigue strength coefficient (σ'_f), fatigue ductility coefficient (ε'_f), fatigue strength coefficient (*b*), and fatigue ductility coefficient (*c*). The σ'_f , ε'_f , *b*, and *c* parameters were determined by experimentation (trial and error). In other words, a set of Basquin-Manson-Coffin parameters was calculated for each strain amplitude studied (0.005, 0.004, and 0.003 mm/mm). Using the experimental data obtained for the stabilized cycles at these strain amplitudes, the values for *b* and *c* were estimated using Equations 2.5 and 2.6, respectively. The parameters, σ'_f and ε'_f , were then approximated with Equation 2.3 and Equation 2.4 (representing the linear plastic and elastic curves, respectively).

The values for *b* and *c* for the Basquin-Manson-Coffin curve were approximated using the relevant cyclic strain hardening exponent for all temperature conditions (Equation 2.5 and 2.6). The parameters, σ'_f and ε'_f , were then determined using the failure life measures from the experimental tests. The values for elastic strain range, plastic strain range, and the modulus of elasticity were determined from the experimental results.

A summary of the results obtained for each strain amplitude at the temperature conditions examined are presented in Table 3.14, Table 3.15, and Table 3.16.

Table 3.14: Approximated experimental Basquin-Manson-Coffin parameters for 0.005 mm/mm

	0.005 mm/mm - Experimental				
	25°C	**150°C**	**200°C**	**250°C**	**300°C**
σ'_f	407.85	286.17	227.37	121.74	53.13
ε'_f	0.0075	0.0378	0.057	0.015	0.347
b	-0.129	-0.089	-0.079	-0.100	-0.067
c	-0.355	-0.556	-0.606	-0.499	-0.664

Table 3.15: Approximated experimental Basquin-Manson-Coffin parameters for 0.004 mm/mm

	0.004 mm/mm - Experimental				
	25°C	**150°C**	**200°C**	**250°C**	**300°C**
σ'_f	433.54	307.73	263.92	123.64	59.33
ε'_f	0.0069	0.0143	0.0781	0.0382	0.373
b	-0.131	-0.108	-0.084	-0.075	-0.057
c	-0.347	-0.458	-0.579	-0.624	-0.716

Table 3.16: Approximated experimental Basquin-Manson-Coffin parameters for 0.003 mm/mm

	0.003 mm/mm - Experimental				
	25°C	**150°C**	**200°C**	**250°C**	**300°C**
σ'_f	601.45	347.34	305.83	133.67	46.91
ε'_f	0.0043	0.0186	0.0401	0.4135	0.514
b	-0.144	-0.108	-0.084	-0.061	-0.036
c	-0.276	-0.458	-0.579	-0.696	-0.822

Using these parameters, three Basquin-Manson-Coffin curves can be generated for each temperature condition. Furthermore, with the parameters for each state (strain amplitude vs. failure), a range of the actual values for parameters representing the experimentally-derived curves can be generated. Using this range of values, and implementing a trial and error approach, the curves for these parameters can be approximated. The values for the parameters are determined by modifying the values within the calculated range until the estimated curve is approximately equal to the experimental S-N curve. The final values for the Basquin-Manson-Coffin parameters obtained using this approach are presented in Table 3.17.

Table 3.17: Final Approximation of Basquin-Manson-Coffin parameters

Complete Manson-Coffin Parameters					
	25°C	**150°C**	**200°C**	**250°C**	**300°C**
σ'_f	575.84	231.65	380.45	284.89	53.13
ε'_f	0.0072	0.0256	0.0154	0.0076	0.3474
b	-0.1105	-0.1084	-0.0854	-0.049	-0.067
c	-0.9019	-0.4582	-0.4432	-0.5994	-0.664

The following figures (Figure 3.68 to Figure 3.72) compare the experimentally derived Basquin-Manson-Coffin curves to the Basquin-Manson-Coffin curves approximated from the calibrated parameters in Table 3.17.

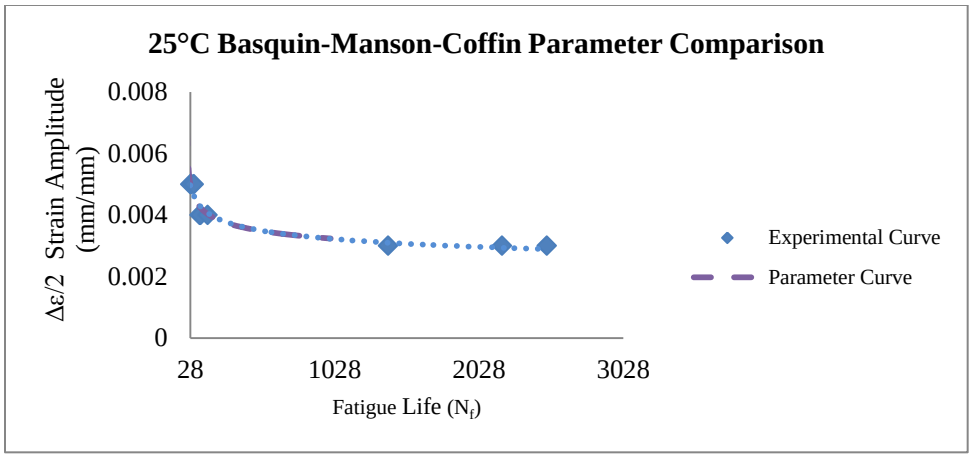

Figure 3.68: Comparison of experimental and approximated Basquin-Manson-Coffin parameter curve for 25℃ at R1

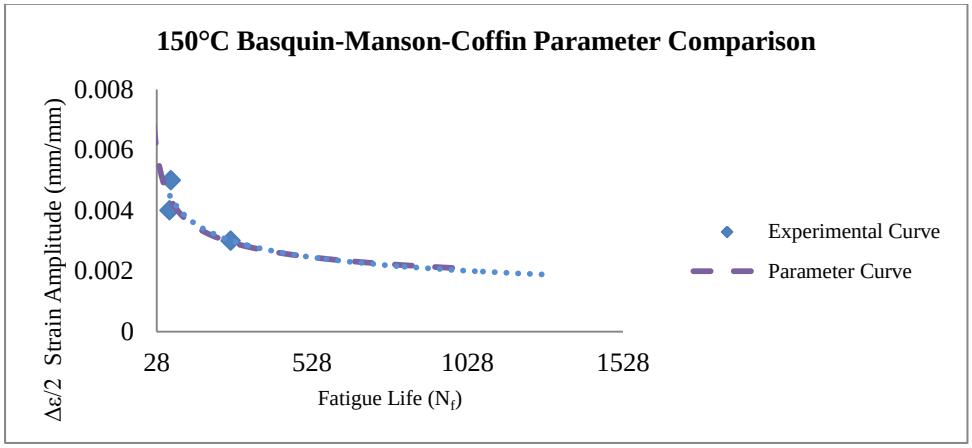

Figure 3.69: Comparison of experimental and approximated Basquin-Manson-Coffin parameter curve for 150℃ at R1

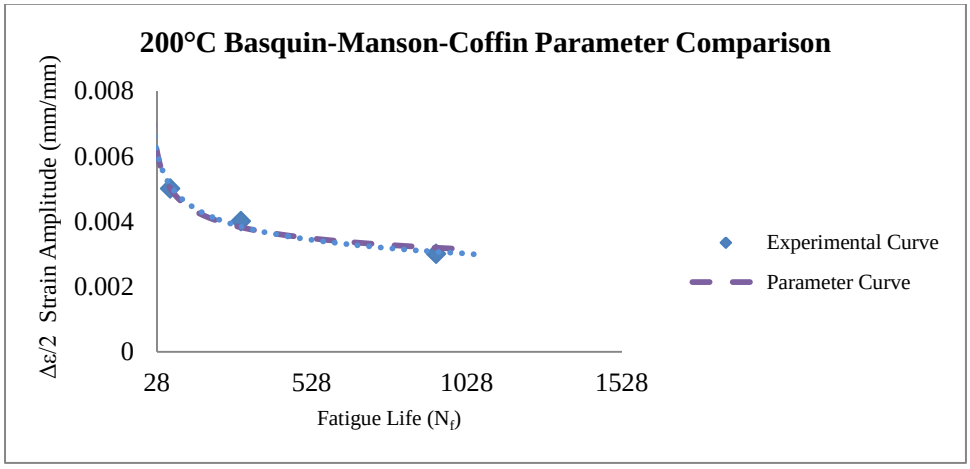

Figure 3.70: Comparison of experimental and approximated Basquin-Manson-Coffin parameter curve for 200℃ at R1

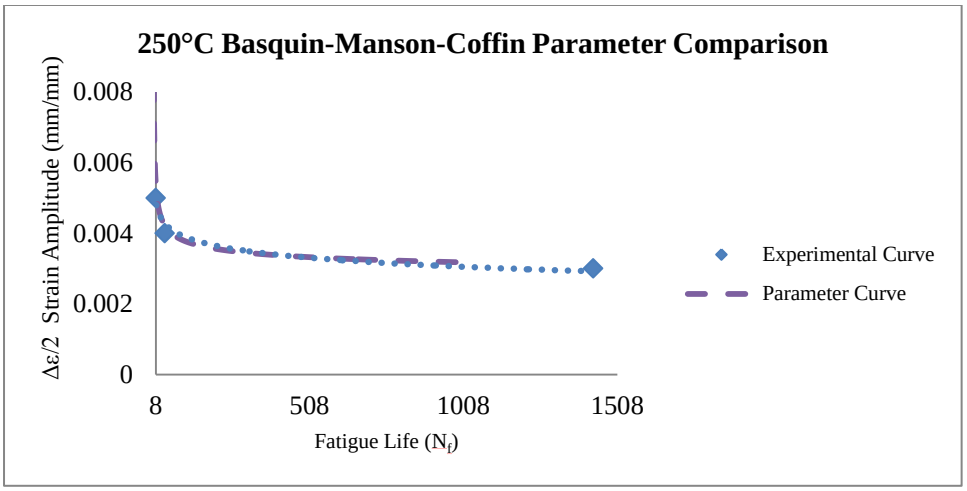

Figure 3.71: Comparison of experimental and approximated Basquin-Manson-Coffin parameter curve for 250°C at R1

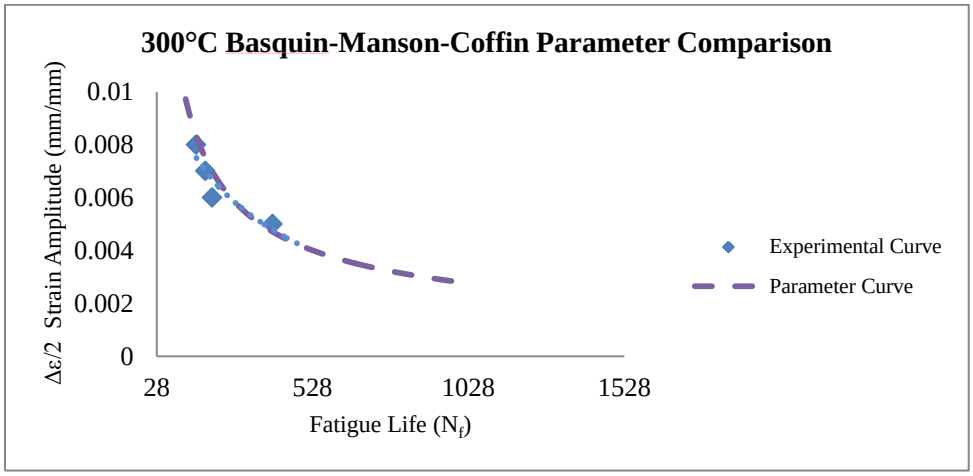

Figure 3.72: Comparison of experimental and Basquin-Manson-Coffin parameter curve for 300°C at R1

The approximated Basquin-Manson-Coffin parameter curves parameters were validated by comparing them to the experimental curves (above figures). The fit of the approximated curves to those obtained experimentally is considered to be acceptable, and so these parameters were used for fatigue life predictions in this thesis.

3.6.2 Calibration of Smith-Watson-Topper (SWT) Parameters

The SWT method uses the same parameters as the Basquin-Manson-Coffin method; however, it takes the maximum stress (σ_{max}) into consideration. Table 3.18 presents the required parameters in the SWT model. The mean stress value is determined from the average of the maximum and

minimum stresses of the hysteresis loop. The maximum stress is then calculated using Equation 3.22; the approximated SWT curves for each temperature condition are shown in Figures 3.73 to 3.77.

$$\sigma_{max} = \sigma_f^{'} \left(2N_f\right)^b \qquad \textit{Equation 3.22}$$

Table 3.18: Maximum stress parameters required for the SWT Model

	SWT Parameters				
	25°C	**150°C**	**200°C**	**250°C**	**300°C**
σ_{max} (MPa)	356.60	134.73	249.02	247.38	33.90

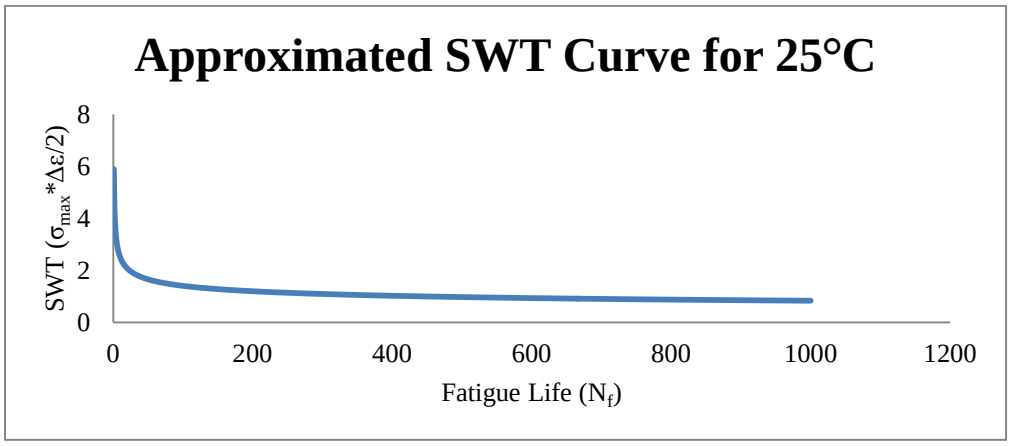

Figure 3.73: Approximated SWT curve for 25℃ at R1

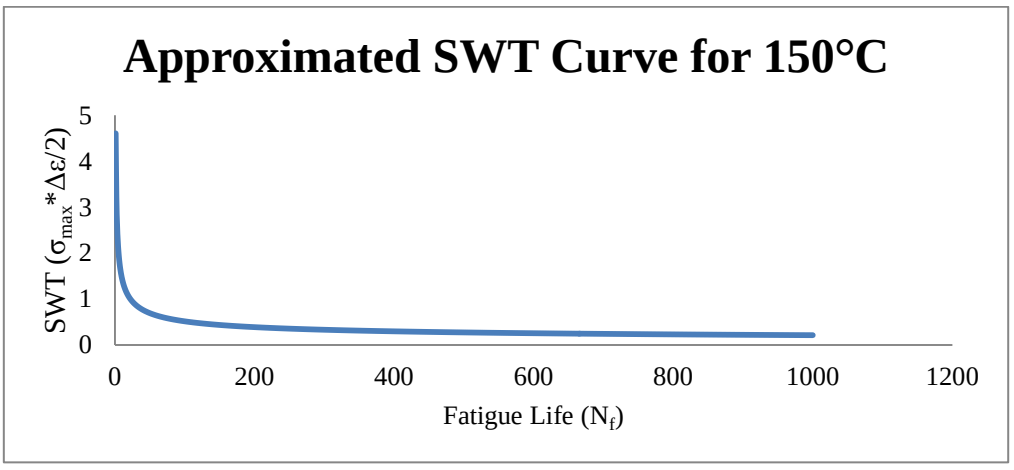

Figure 3.74: Approximated SWT curve for 150°C at R1

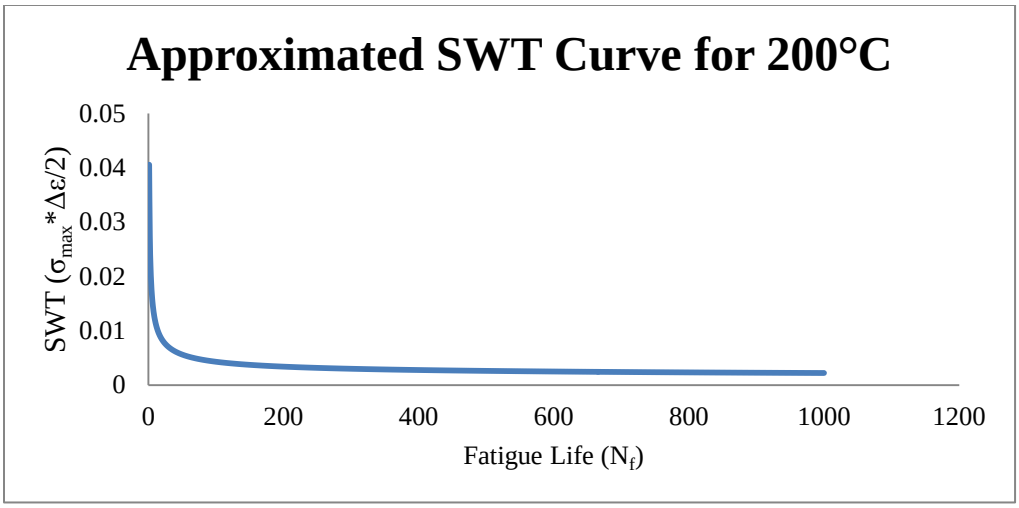

Figure 3.75: Approximated SWT curve for 200°C at R1

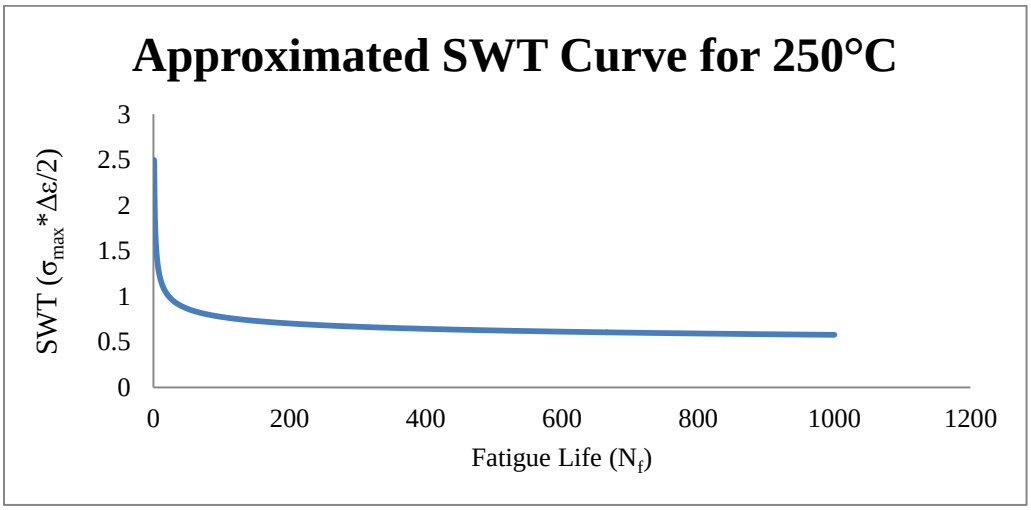

Figure 3.76: Approximated SWT curve for 250°C at R1

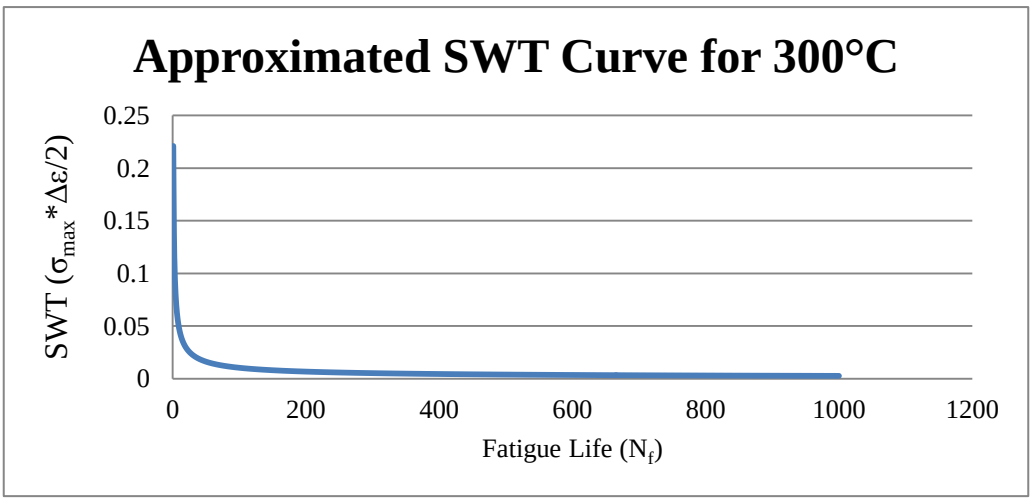

Figure 3.77: Approximated SWT curve for 300°C at R1

3.6.3 Calibration of Morrow Parameters

The Morrow equation requires calculation of the parameter, mean stress (σ_m), the average of σ_{min} and σ_{max}. The values calculated for the Morrow parameters for each temperature condition are shown in Table 3.19. Although the mean stress is very small, and almost negligible, its value must be considered for fatigue life predictions involving the Morrow model.

Table 3.19: Mean stress parameters required for the Morrow model

	Morrow Parameters				
	25°C	**150°C**	**200°C**	**250°C**	**300°C**
σ_m (MPa)	-2.23	0.11	-0.33	-0.13	0.04

3.6.4 Calibration of Taira's Model Parameters

The parameters that need to be calculated for Taira's model are the temperature damage factor ($\lambda(T)$), material constant independent of temperature (C_1), and a material exponent (n). In most cases, the material exponent is approximately two. The temperature damage factor can be determined for either isothermal or TMF conditions.

Isothermal temperature damage factor $\lambda(T)$:

The temperature damage factor for isothermal loading can be determined by comparing the fatigue life at room temperature ($N(T_0)$) to the fatigue life at an elevated temperature ($N(T)$) as shown in Equation 3.23.

$$\lambda(T) = \frac{N(T_0)}{N(T)} \qquad \textit{Equation 3.23}$$

Thermal Mechanical Fatigue:

The first step is to determine the equivalent temperature (T_e). The equivalent temperature is the average of the various temperatures that the material experienced over a period of time, as shown in Figure 3.78.

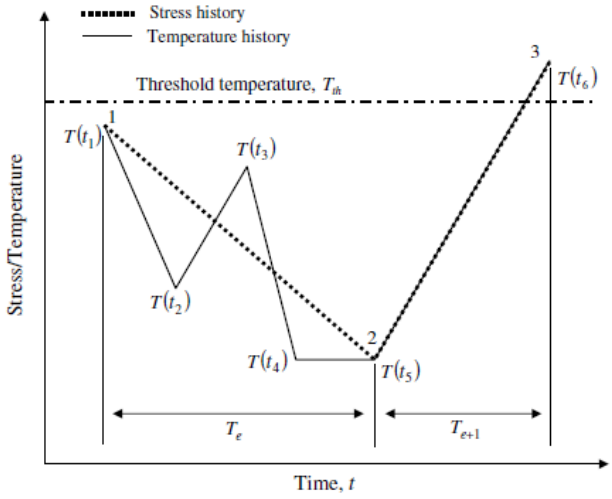

Figure 3.78: Equivalent Temperature at different times [13]

The equivalent temperature (T_e) can be calculated as shown in Equation 3.23.

$$T_e = \frac{T(t_1)+T(t_2)+T(t_3)+T(t_4)+T(t_5)}{5} \qquad \textit{Equation 3.23}$$

Depending on whether the T_e is close to the mean temperature (Tm) or the upper limit temperature (T_2), the temperature damage factor ($\lambda(T_e)$ can be calculated using Equations 3.24 or 3.25, respectively (see Figure 2.12 for further information).

$$\lambda(T_e) = \frac{1}{T_2 - T_1}\int_{T_1}^{T_2} \lambda(T)dT \qquad \textit{Equation 3.24}$$

$$\lambda(T_e) = \frac{1}{T_2^{'} - T_1}\int_{T_1}^{T_2^{'}} \lambda(T)dT + \frac{\lambda(T_2)}{2} \qquad \textit{Equation 3.25}$$

Results of the calculations of the parameters for Taira's iso-thermal damage model are shown in Table 3.20, Table 3.21, and Table 3.22.

Table 3.20: Calculated iso-thermal parameters for Taira's damage model for 0.005 mm/mm

Strain Amplitude - 0.005 mm/mm							
Iso-thermal							
N_f	Temp. (°C)	$(\lambda(T))$	N_f	$\Delta\varepsilon_p$	c	C_1	n
40	25	1.00	40	0.0032	0.020	0.00040	2
74	150	1.85	74	0.0047	0.041	0.00164	2.1
72	200	1.80	72	0.0056	0.048	0.00229	2.1
9	250	0.23	9	0.0071	0.021	0.00045	1.7
400	300	10.00	400	0.0082	0.164	0.02678	2.5

Table 3.21: Calculated iso-thermal parameters for Taira's damage model for 0.004 mm/mm

Strain Amplitude - 0.004 mm/mm							
Iso-thermal							
N_f	Temp. (°C)	$(\lambda(T))$	N_f	$\Delta\varepsilon_p$	c	C_1	n
113	25	1.00	113	0.0021	0.022	0.0005	2.0
70	150	0.62	70	0.0030	0.025	0.0006	1.9
300	200	2.65	300	0.0038	0.067	0.0044	2.2
38	250	0.34	38	0.0051	0.032	0.0010	1.8
709	300	6.27	709	0.0062	0.165	0.0273	2.4

Table 3.22: Calculated iso-thermal parameters for Taira's damage model for 0.003 mm/mm

Strain Amplitude - 0.003 mm/mm							
Iso-thermal							
N_f	Temp. (°C)	$(\lambda(T))$	N_f	$\Delta\varepsilon_p$	c	C_1	n
2029	25	1.00	2029	0.0009	0.040	0.0016	2.0
267	150	0.13	267	0.0021	0.034	0.0012	1.7
930	200	0.46	930	0.0020	0.060	0.0036	1.9
1430	250	0.70	1430	0.0033	0.123	0.0151	1.9
709	300	0.35	709	0.0042	0.113	0.0127	1.8

For the TMF experiments, the T_e (225°C) was equal to the T_m (225°C). For this reason, the equivalent temperature damage factor was determined using Equation 3.24. Table 3.23 shows the calculated parameters for IP TMF according to Taira's damage model.

Table 3.23: Calculated model parameters for IP TMF according to Taira's damage model

IP TMF					
Nf	$\Delta\varepsilon_p$	$(\lambda(Te))$	C	C_1	n
107	0.012	2.25	0.120	0.0082	2.3

3.6.5 Calibration of Skelton Model Parameters

In order to apply the Skelton model, two parameters must be determined: λ and C. The parameter, λ, is a material constant that can be determined by creating a log-log plot of the total strain versus plastic strain for the respective hysteresis loop. The value of λ will be positive for a cyclic hardening material and negative for a cyclic softening material. Figure 3.79 illustrates the determination of λ at 25°C; the process is the same for all temperatures. The parameter, C, is the initial material strength constant for a given plastic strain, which can be calculated using Equation 3.26.

$$\Delta\sigma = CN^{\lambda} \qquad \textit{Equation 3.26}$$

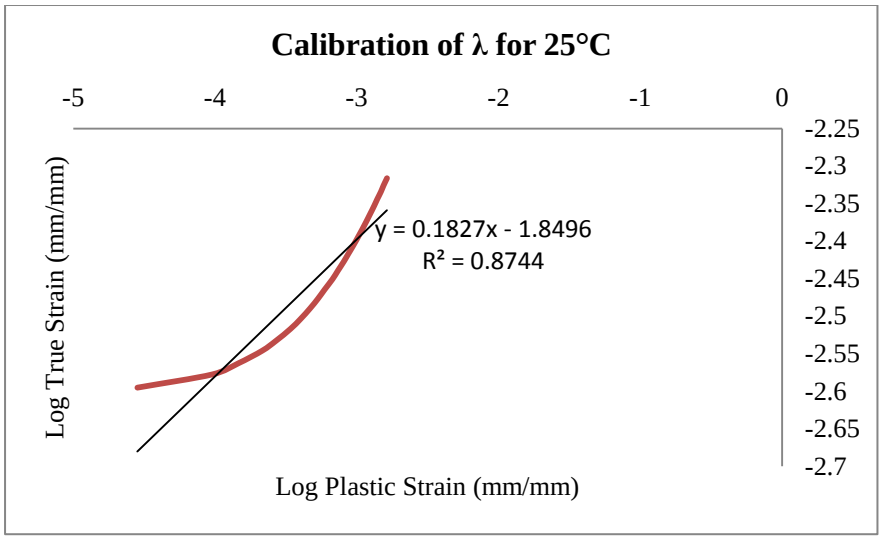

Figure 3.79: Skelton model parameter calibration for λ for 25°C

The final Skelton model damage parameters for all strain amplitudes and temperatures are summarized in For the 0.003 mm/mm strain amplitude, no parameters were determined for 300°C because no experimental data was obtained for this temperature.

*Table 3.24*Table 3.24, Table 3.25, and Table 3.26. For the 0.003 mm/mm strain amplitude, no parameters were determined for 300°C because no experimental data was obtained for this temperature.

Table 3.24: Skelton damage model parameter calculations for 0.005 mm/mm

Strain Amplitude - 0.005 mm/mm			
N_f	**Temperature (°C)**	**λ**	***C***
40	25	0.183	291.4
74	150	0.296	141.3
72	200	0.293	129.9
9	250	0.405	119.2
400	300	0.571	4.2

Table 3.25: Skelton damage model parameter calculations for 0.004 mm/mm

Strain Amplitude - 0.004 mm/mm			
N_f	**Temperature (°C)**	**λ**	***C***
113	25	0.152	255.4
70	150	0.186	198.7
300	200	0.186	134.8
38	250	0.425	59.9
709	300	0.636	3.05

Table 3.26: Skelton damage model parameter calculations for 0.003 mm/mm

Strain Amplitude - 0.003 mm/mm			
N_f	**Temperature (°C)**	**λ**	***C***
2029	25	0.181	118.9
267	150	0.196	144.7
930	200	0.132	136.8
1430	250	0.31	25.5
-	300	-	-

An Example of Applying the Skelton Model to Predict Fatigue Life

The Skelton model was applied to the findings obtained for the 0.005, 0.004, and 0.003 mm/mm strain amplitude experiments. In order to predict the fatigue life of the simulation specimens

using the Skelton model, a rather complex approach had to be taken. The sequence of steps that were used to predict the fatigue life of a simulation specimen is described below.

Step 1

In the first step the energy dissipated per unit volume for only one cycle is determined using Equation 2.24. This calculation was performed for all 5 temperatures.

Step 2

Using the critical accumulation energy can be determined using the energy dissipated for a stabilized cycle with Equation 2.29 and the fatigue life known from experimental testing. This value was calculated for all temperatures.

Step 3

Using Equation 2.28, the accumulated energy was determined from 1 to 1000 cycles, and then the critical accumulated energy (W_c) was interpolated from the resulting curve in a similar fashion to that described for the Basquin-Manson-Coffin and SWT methods.

3.7 Discussion for Calibration of the Fatigue Damage Model Parameters

In order to apply the damage models studied in this thesis, reliable and valid parameter measures are required to calculate accurate and consistent predictions of fatigue life. Accurate and repeatable experimental data is required in order to derive reliable and valid damage model parameters.

Replication of experimental data was more problematic than anticipated for some stages of this study; the lack of consistent and complete data for all of the planned experimental conditions had

to be managed for the calibration of the damage model parameters. The Basquin-Manson-Coffin parameters are included in many of the damage models examined in this thesis; thus, obtaining accurate, reliable, and valid experimental data is required in order to derive more accurate damage model parameters and improve the outcomes from many of these damage models. Unfortunately, at this point, the calibrated parameters for the material models are the best experimental data currently available.

The Basquin-Manson-Coffin curve for room temperature conditions is considered reliable because it is based on three sets of data (three specimens for each set) corresponding to N_f at each of the three studied $\Delta\varepsilon/2$. However, for all of the other temperature conditions studied, only one data point is available for N_f that corresponds to $\Delta\varepsilon/2$. Although this is not best practice in the design of comprehensive research studies, this is the data available at this time, and the findings are informative, and may prove useful in planning future studies. Nevertheless, until more experimental data are collected, these particular findings should be considered as the preliminary results obtained from a pilot study.

Chapter 4 Fatigue Life Prediction Results

This section includes three sub-sections explaining the procedural steps that were followed in order to predict fatigue life for the specimens examined in this thesis.

4.1 Fortran Post Processing Routine

A Fortran post-processing routine, "Fatigue Life Calculator" (FLC), was developed. This post-processing tool allows the user to easily predict the fatigue life of any FEA model solved with ABAQUS; when ABAQUS processes a simulation, the user can create a node-based result file in which the FLC program can predict the fatigue life at each node. The user can select one of the seven damage models implemented in the FLC to predict fatigue life: the Basquin-Manson-Coffin, SWT, Skelton, von Mises, Morrow, ASME, and Taira's models. After the fatigue life has been predicted for each node, an output file is generated. This output file is in a format that is readable by MSC Patran, so that a contour map of the fatigue life for each node of the part geometry can be plotted to identify the critical areas of failure.

4.1.1 Implementation of the Fortran Routine for Fatigue Life Predictions

The structure in which the routine operates is relatively simple. After the input file has been read and the user has selected their desired damage model, repetitive iterations of the routine begin. As the fatigue damage model is always a function of fatigue life, the iteration begins at N_f=1and is then repeated again and again; this continues until N_f satisfies the damage models equation. When this occurs, the iteration number is recorded and stored as the fatigue life measure. The condition that needs to be satisfied in order to complete the routine is that the damage model equation must equal zero; this happens when the value of N_f satisfies the equation. The flowchart in Figure 4.1 explains the processes of the FLC routine.

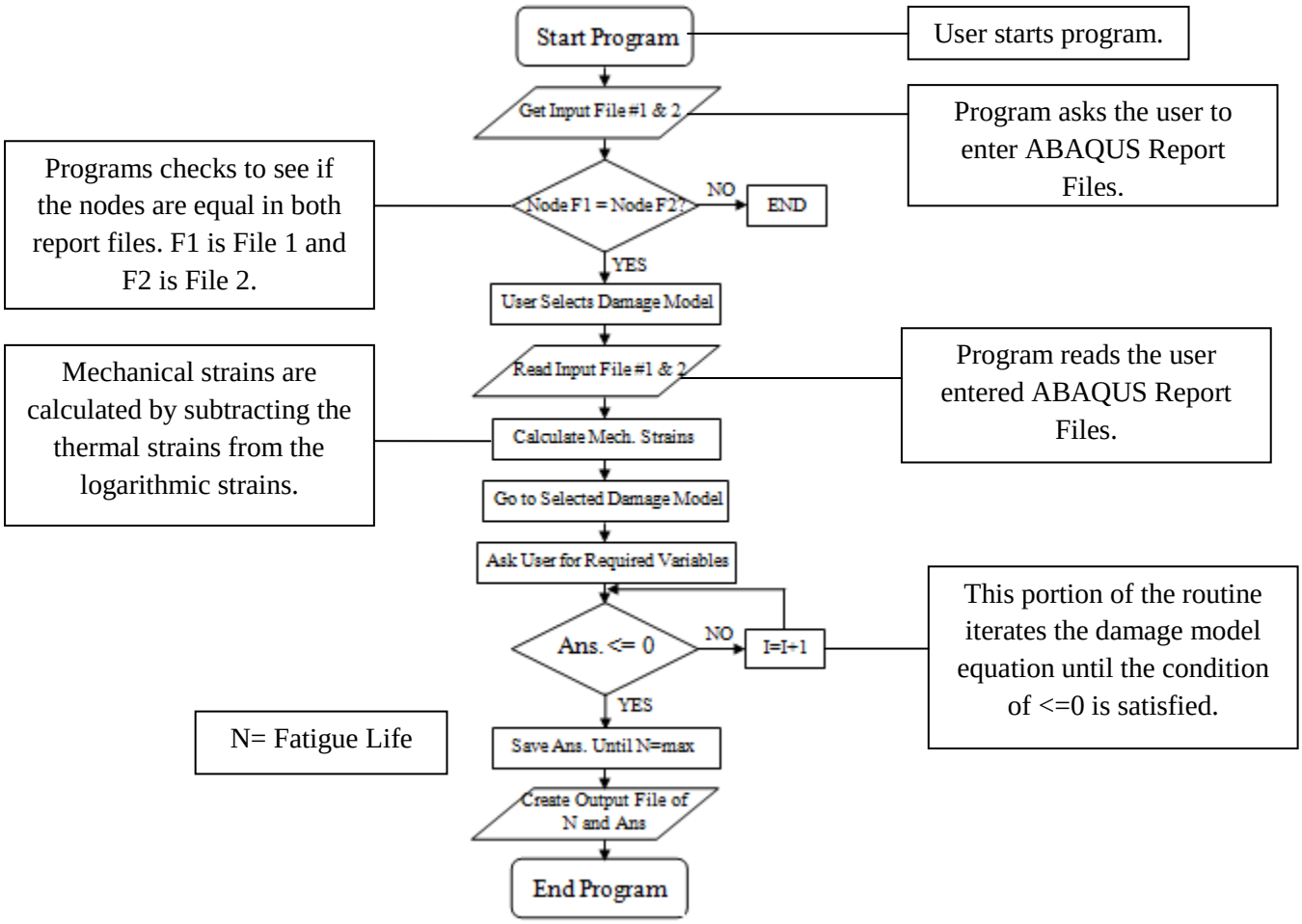

Figure 4.1: Flow Chart of FLC Fortran routine showing step by step the operations by which the FLC program performs the calculations necessary to predict fatigue life.

4.1.2 Implementation of the ABAQUS Report File for FLC Program Calculations

This is an important step because if the incorrect field outputs are requested in ABAQUS, the results obtained from the FLC program will not be correct. The FLC program reads each column in a specific order, so if the order of field outputs differs from the order that the program expects, certain variables will be assigned the incorrect values, and result in inaccurate fatigue life predictions.

Thus, the first step is to ensure that the ABAQUS simulation input requests the following field outputs, PE,EE,LE,THE, and S (defined below).

PE –Plastic Strains

EE – Elastic Strains

LE – Logarithmic Strains

THE – Thermal Strains

S –Stresses

The next step is to generate the report file; the procedural steps that the user would follow are presented in the following section.

4.1.3 Procedure for Creating the Report File

Step 1

Open the ABAQUS viewer or CAE and open the .ODB results file with the module set to visualization as shown in Figure 4.2.

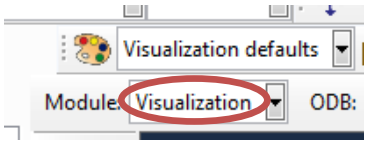

Figure 4.2: Setting the module to visualization setting.

Step 2

Click on the tab titled ‘Report’, and then select ‘Field Output’ from the dropdown menu, as shown in Figure 4.3.

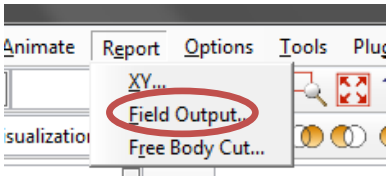

Figure 4.3: Required operation to generate a field output report.

Step 3

Figure 4.4 shows the window that opens. At this stage, a few changes to the default selections are required in order to generate the report file correctly.

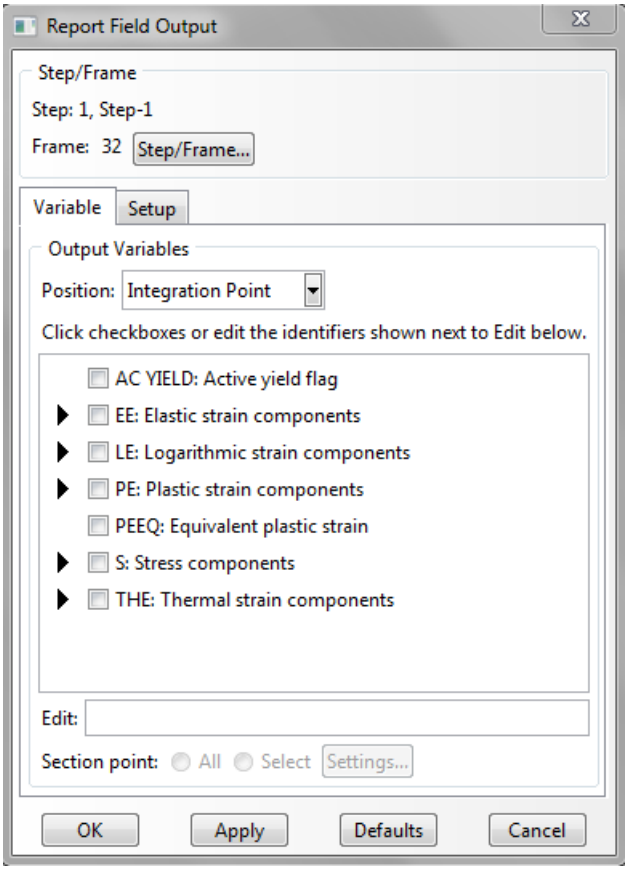

Figure 4.4: Report field output window.

Step 4

In order to select the output variables, the position should be switched from 'Integration Point' to 'Unique Nodal', and the appropriate field output variables (SE, LE, PE, S, and THE) should be selected as shown in Figure 4.5. If using ABAQUS CAE or Viewer2012, unselect the absolute variable for all of the selected field outputs as this will affect the way in which the variables are read.

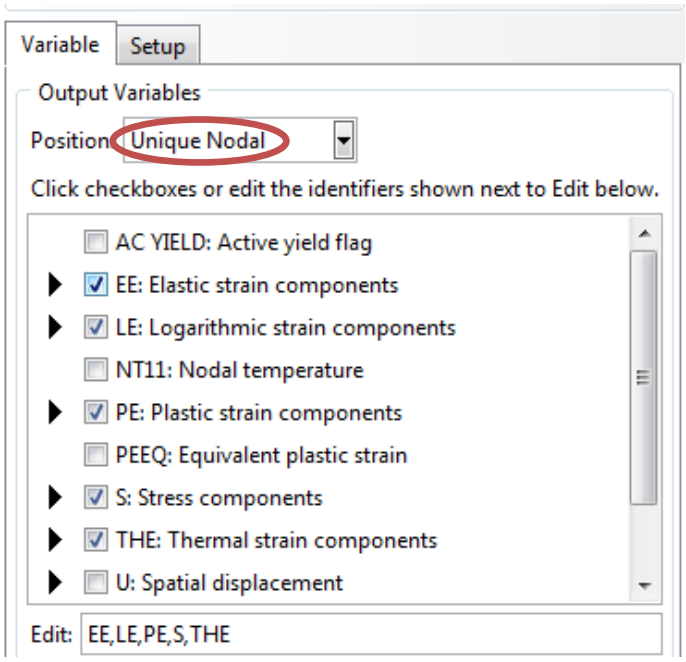

Figure 4.5: Field output variable selection.

Step 5

In this step, the format of the output file is specified as the format required by the FLC program. After naming the report file, select the output format characteristics as "Single table for all field output variables". The values should be sorted by "Node Label", and in ascending order. Set the page width to "No limit". The number of significant digits should be 6, and the number format should be "Engineering". In the data section, selection "Write"; this is the only option selected, and the "Field Output", "Column totals", and "Column max/min" options are unchecked (see Figure 4.6 for an example of the appropriate setup).

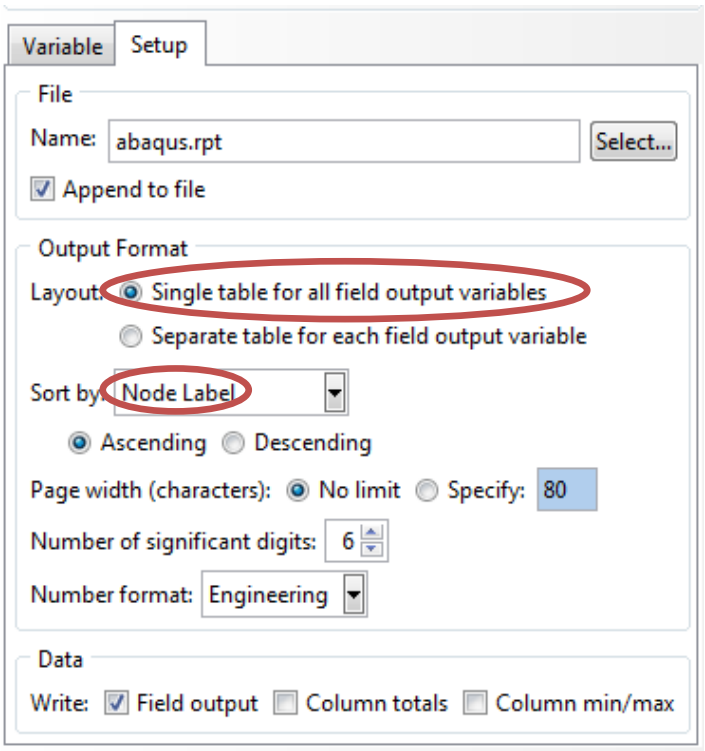

Figure 4.6: ABAQUS report file setup. It is critical that the proper operations are selected for correct file formatting.

Step 6

This is the final step in the procedure required to generate the FLC report file. Select the calculation step for which the report file will be generated, as shown in Figure 4.7. For example, if step 1 is selected, the report file will be generated for the field outputs calculated in Step.1 Two reports need to be generated (one representing the loaded condition and the other representing the unloaded condition), so that the FLC can determine the proper hysteresis loops.

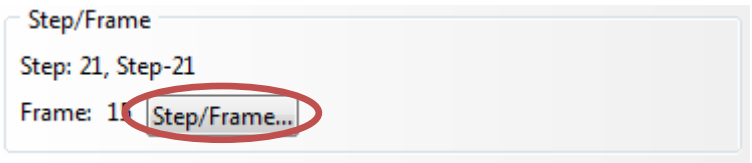

Figure 4.7: Step selection. Clicking the "Step/Frame" button allows the selection of the step that the report file of field outputs will include.

4.1.4 Application of the Fatigue Life Calculator

This section describes the procedures (step by step) for the use of the FLC program. In order to use the FLC, the operating system must be capable of running command prompts (cmd.exe), which are part of all Windows operating systems. It is also essential that the FLC executable file is located in the same folder as the ABAQUS report files in order for the program to read the files containing the data used in the fatigue life calculations.

Step 1

To launch the FLC, either click the executable file directly or launch it through the cmd.exe window. The initial start-up screen is shown in Figure 4.8.

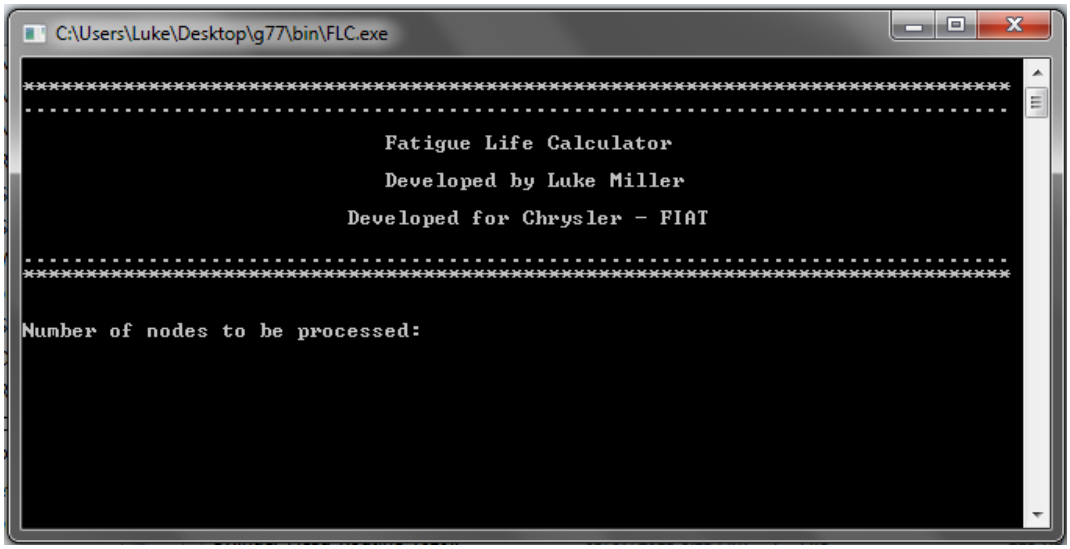

Figure 4.8: Fatigue life calculator start-up screen.

Step 2

Enter the desired number of nodes to be used in the calculations, as shown in Figure 4.9. The specified number of nodes to be processed can be less than the total number of nodes within the meshed model specimen, thus reducing calculation times. The maximum number of nodes that

can be processed is 2,000,000; if a value >2,000,000 is entered, a warning prompt is displayed and a new number is requested.

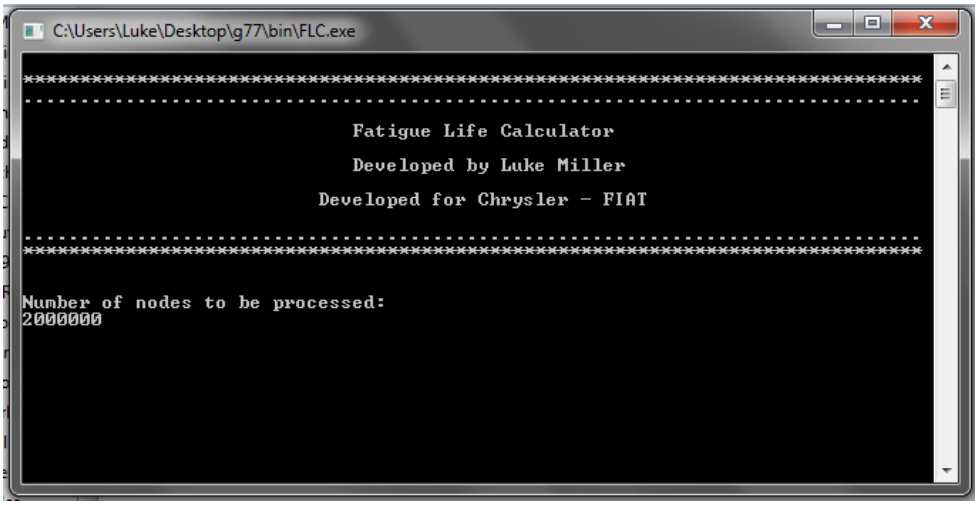

Figure 4.9: Entering the choice for number of nodes to process.

Step 3

At this point, the name of the file that contains the data for the loading condition must be entered. This is the report file for the loading condition that was previously created using ABAQUS (described in Section 4.1.3). For example, Figure 4.10 indicates that a file named "load.rpt" was specified. The file "load.rpt" contains stress and strain data that represents a loading condition. Note that the file name is limited to 30 characters.

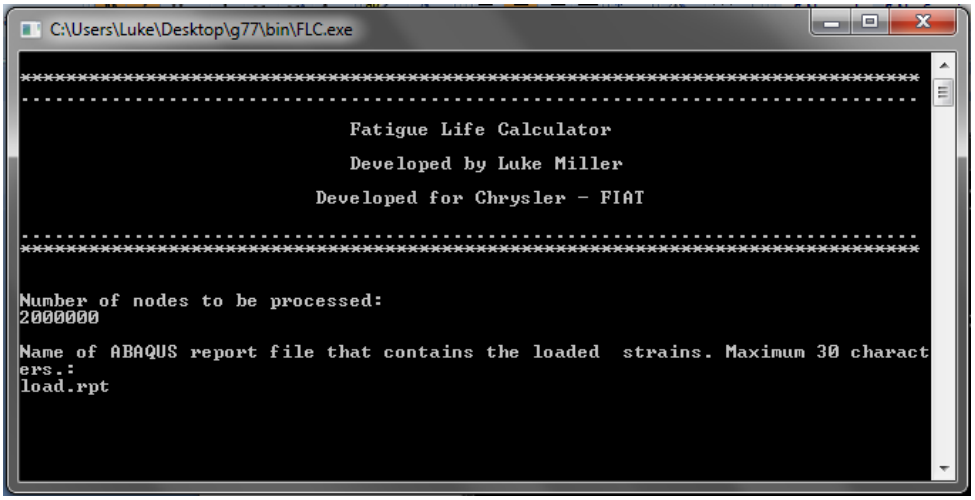

Figure 4.10: Specifying the report file containing data for loading conditions.

Step 4

This step resembles the previous step; in this case, a file containing the data for an unloading condition is entered; for example, in Figure 4.11 a file named "unload.rpt" was entered. This is the report file for the unloading condition that was previously created using ABAQUS (as described in Section 4.1.3). Note that the file name entered at this step is also limited to 30 characters.

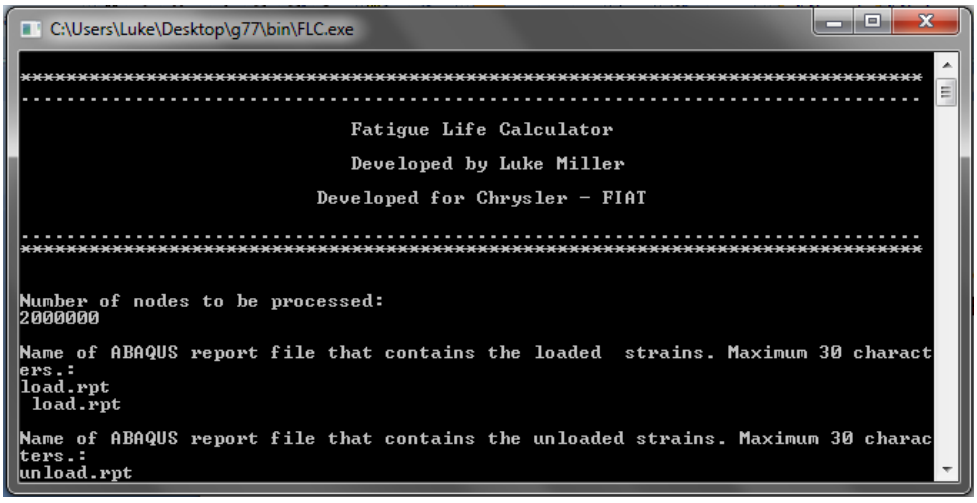

Figure 4.11: Entering the report file containing the data for the unloading condition.

Step 5

The fatigue damage model to be used for the calculation of fatigue life is selected in this step; however, before this is done, a node check needs to be performed. The node check is used to verify that associated loading and unloading data were selected (i.e., to confirm that the first node of each report file matches). If these nodes are not equivalent, then the report files that have been selected by the user are incorrect, and should be checked for errors.

The user has the choice of seven damage models to calculate fatigue life. These damage models are the Basquin-Manson-Coffin, SWT, Skelton, von Mises, Morrow, ASME, and Taira's models. Each one of these damage models has its own unique characteristics and requires specific input variables (see Sections 2.3.1 and 2.3.2 for details). Figure 4.12 illustrates the selection process for the fatigue criteria; the user enters the appropriate numeric code for the desired fatigue criteria at the prompt.

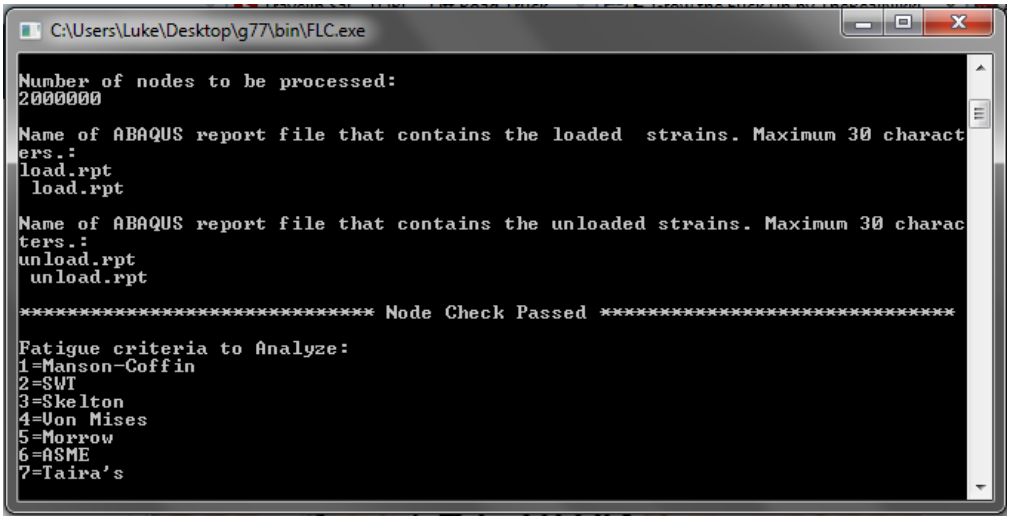

Figure 4.12: Fatigue criteria selection process.

Step 6

The remaining steps are illustrated with an example based on the selection of the Basquin-Manson-Coffin fatigue criteria. At this point, options for the determination of fatigue life are

selected by entering the numeric code (1 to 7) for the desired components. For example, if calculations in all directions are desired, then option 7 is selected, which produces six output files. Figure 4.13 shows the component selection process for the direction of loading in the FLC program, and includes the following options:

11 – x-direction (Option 1)

22 – y-direction (Option 2)

33 – z-direction (Option 3)

MIN PR – Minimum Principal (Option 4)

MID PR – Middle Principal (Option 5)

MAX PR – Maximum Principal (Option 6)

All Directions – (Option 7)

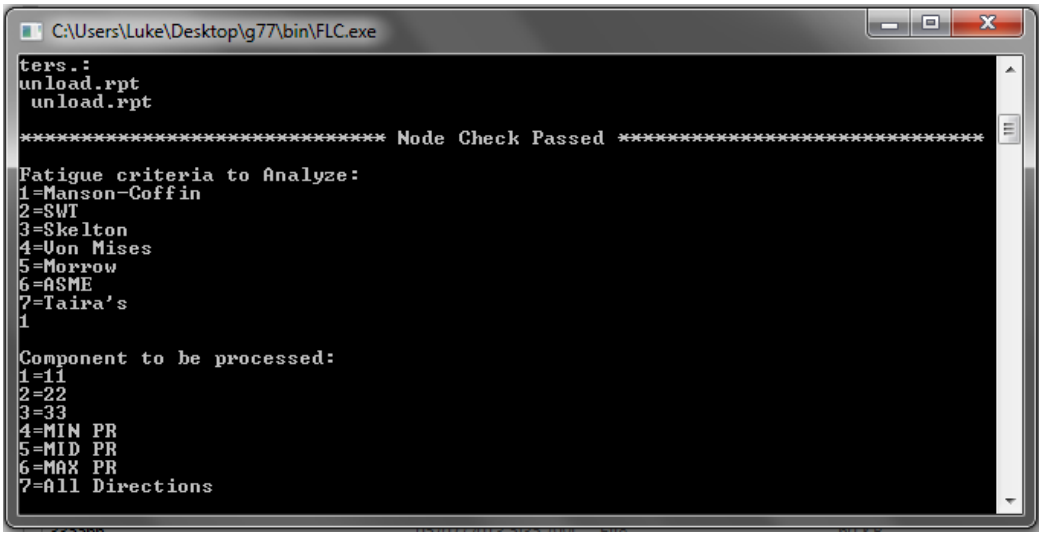

Figure 4.13: Selection process for direction of loading component.

Step 7

After selecting the direction component upon which to base the calculations, the user enters the specific parameters (coefficients) required for the selected fatigue damage model. Some damage

models require different parameters than others, so the user must be prepared to enter the values of the coefficients determined for the damage model's parameters before using this program. Figure 4.14 presents an example of the entry of the coefficient values for the required Basquin-Manson-Coffin parameters. The methods for determining these parameters for the damage models included in the FLC application are described in Sections 2.3.1 and 2.3.2.

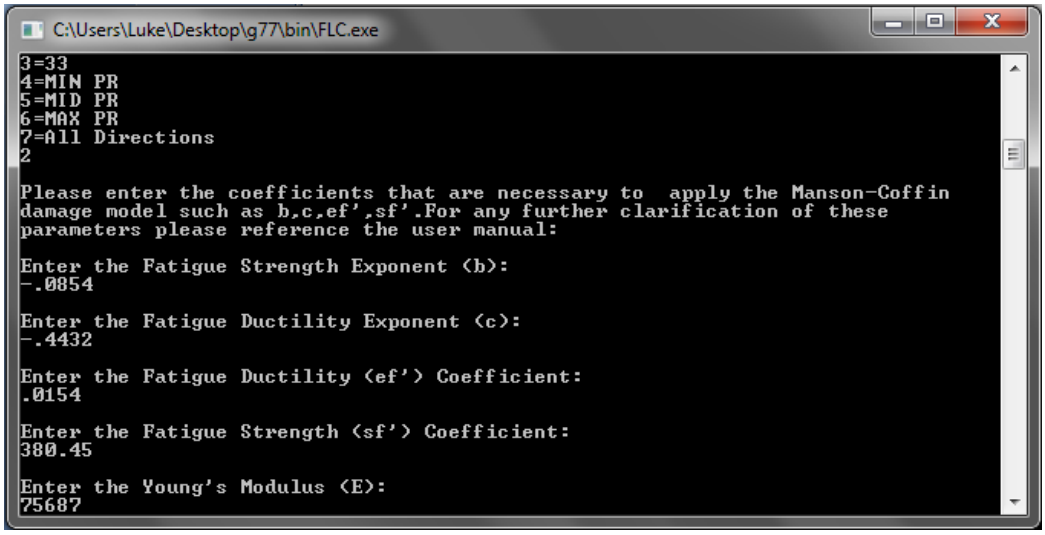

Figure 4.14: Entering the values determined for the Basquin-Manson-Coffin parameters into the FLC program.

Step 8

This is the final step required to use the FLC; the designated name for the MSC Patran output file is entered, as shown in Figure 4.15, and the program calculates the predicted fatigue life accordingly.

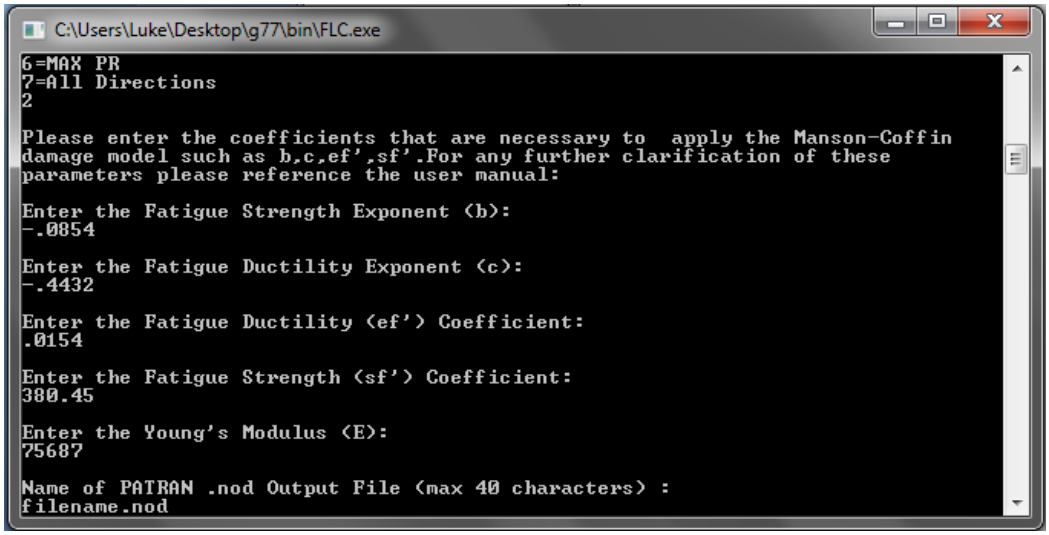

Figure 4.15: Entering the MSC Patran output filename.

When the calculations are complete a message will be displayed, as shown in Figure 4.16.

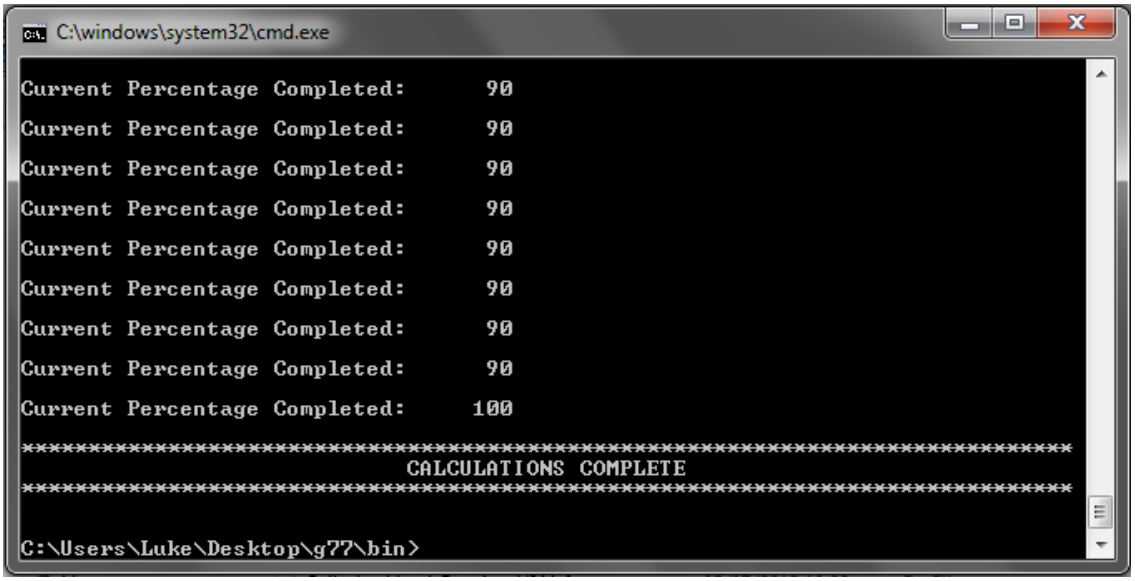

Figure 4.16: FLC Program calculations complete message.

4.1.5 Implementation of FLC Results with MSC Patran

This portion of the thesis describes the procedure required to open the output of the FLC program (the file containing the results of the fatigue life calculations) in ABAQUS. To illustrate, an example of the results obtained for a simple fatigue test specimen will be presented; the steps for this procedure follow:

Step 1

The first step is to open the model specimen in MSC Patran. To do this, the import geometry is required from a file that is in MSC Nastran format (.bdf). To import this file, open MSC Patran, select the appropriate file, and then click 'Import'. This will open the window shown in Figure 4.17; note that the "Source:" option must be set to "MSC.Nastran.Input". Although other file types may be imported into MSC Nastran; the method relevant to the import of files containing FLC results for the research in this thesis pertains to importing files from MSC Nastran.

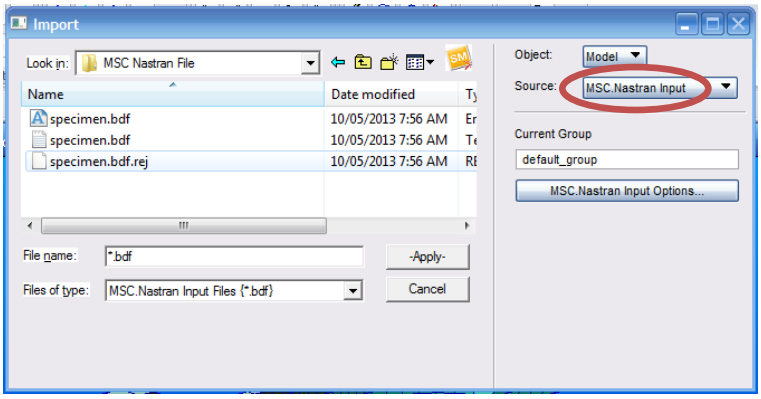

Figure 4.17: MSC Patran model import process.

Once the MSC Patran file containing the appropriate geometry has been imported, the MSC Patran application can use the coordinates to locate all of the nodes describing the model's geometry to assemble the model specimen. Figure 4.18 shows the imported model of the simple fatigue test specimen used in this example.

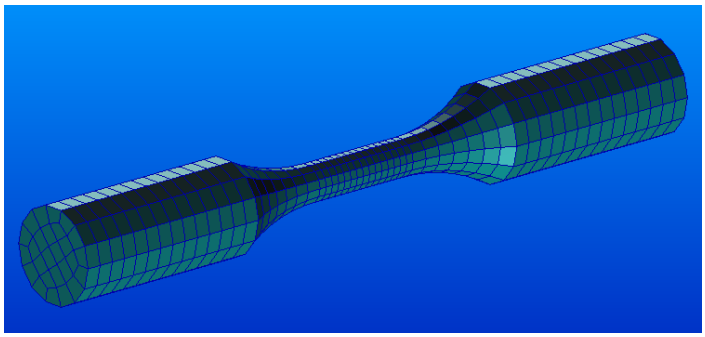

Figure 4.18: Imported MSC Patran specimen model.

Step 2

With The FLC result files can be imported into MSC Patran now that the model has been opened; the process is similar to importing the MSC Nastran (.bdf) file described in the first step. Select the file containing the FLC results, and then click 'Import'. When the Import window opens, change the default selections from "Object:" to "Results" and "Format:" to "PATRAN.2.nod" as illustrated in Figure 4.19. When changes are made to the "Format:" option, another window will open as shown in Figure 4.20; select "mscnastran_access_nod.res_tmpl" from the template options.

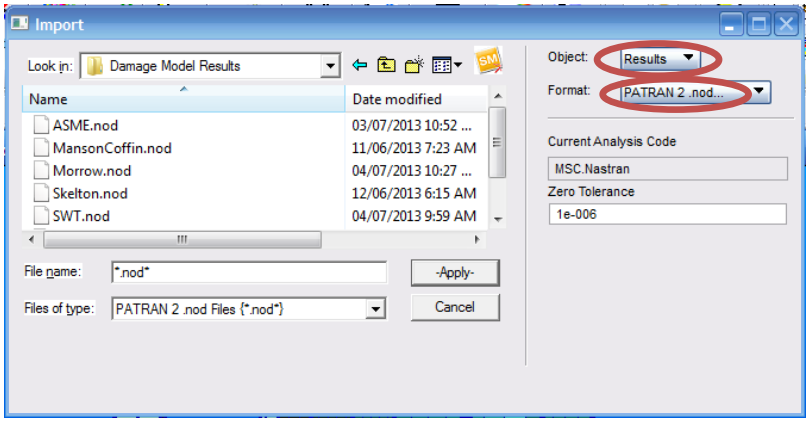

Figure 4.19: Import .nod files.

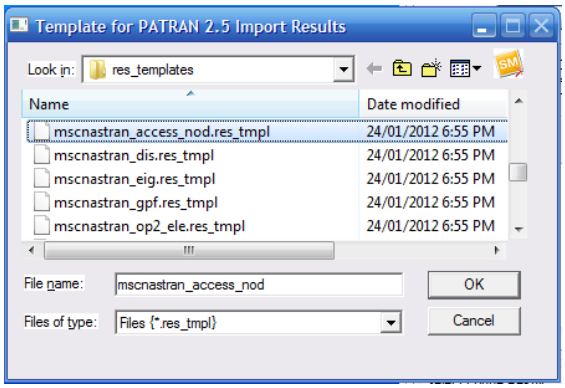

Figure 4.20: MSC Patran .nod template selection.

Step 3

Select the file containing the FLC results (.nod file) to import into MSC Patran, and click ‘Apply’. Select the ’Results’ menu tab, which is shown circled in red in Figure 4.21.

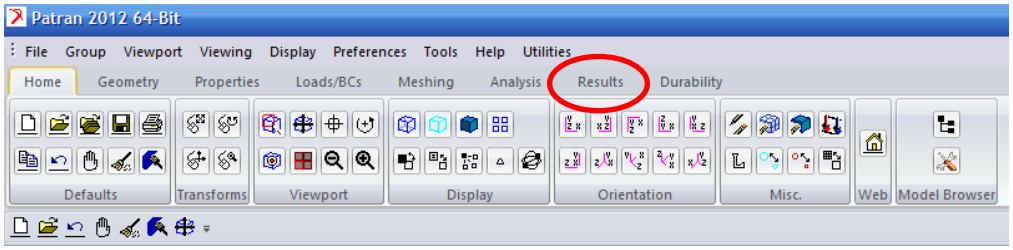

Figure 4.21: MSC Patran results tab location.

The “Results” workbench will open, as shown in Figure 4.22; set “Action:” to ‘Create’ and “Object:” to ‘Fringe’. Select the appropriate case from the imported ‘Result Cases’, and then select the ‘Fringe Result’ as shown in Figure 4.24.

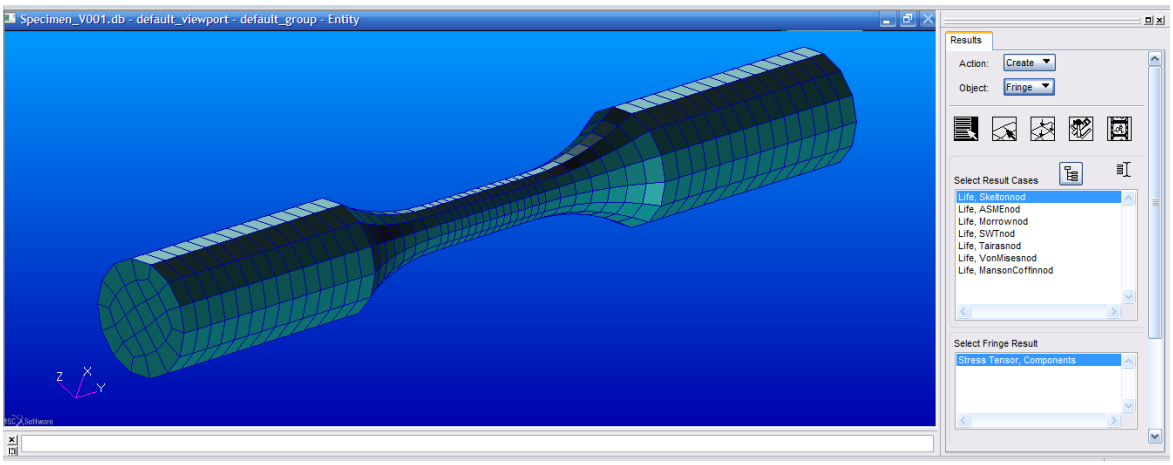

Figure 4.22:MSC Patran results workbench.

Scroll to the bottom of this workbench, and change the option for "Quantity:" to "X Component" as shown in Figure 4.23, and apply these selections.

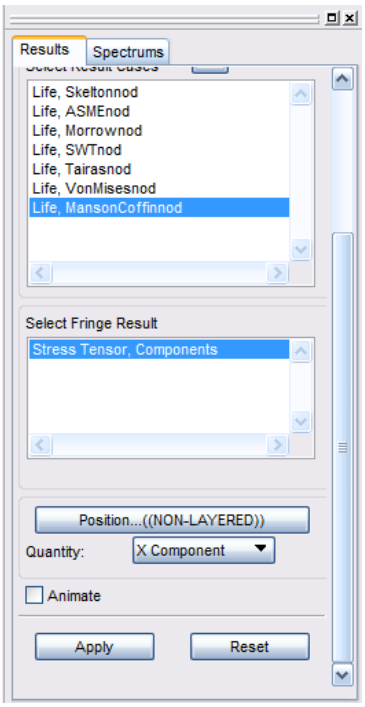

Figure 4.23: Results workbench quantity change.

A final contour map will be produced, similar to the example shown in Figure 4.24. This contour map can now be used to locate the critical areas of the part based on predicted fatigue life rather than locating critical areas based on stress or strain, which may be less accurate.

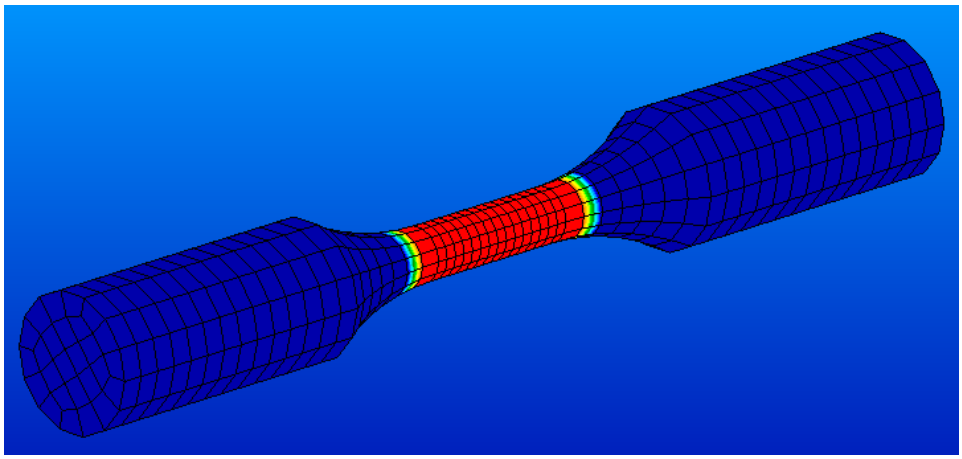

Figure 4.24: MSC Patran fatigue contour plot derived from FLC results file.

4.1.6 Discussion Fortran FLC Program Routine Implementation

The FLC program was developed with the objectives of providing flexibility and adaptability in assessing potential damage and durability concerns in component parts. This unique program is capable of determining critical areas of potential failure in a component based on the predicted fatigue life. This is likely to be a more accurate and valid approach than determining critical areas of probable failure due to fatigue based solely on maximum stresses or strains. Fatigue life predictions are usually based on the difference between two extreme states of loading ($\Delta\varepsilon$ or $\Delta\sigma$). This program offers the user the flexibility to choose the most appropriate model from several different damage models with their own unique applications and assumptions. Using the output file from the FLC program, the results can be imported into MSC Patran to produce a visual representation of the location of critical areas of potential failure in a model specimen.

There are some limitations to the FLC program in its current operational state. The most obvious of these is that it is currently limited to seven damage models (five uniaxial and two multi-axial damage models). In addition, this program is only functional with the applications, ABAQUS and MSC Patran, due to compatibility issues involving file format. Modifications can easily be introduced in the future to enable the FLC program to work with other FEA software

applications, such as MSC Nastran. The FLC program also requires that the user request the correct sequence of output parameters for the ABAQUS report file or else the FLC program will automatically enter the parameters and assign them to variables incorrectly; thus, the user must verify this step. It is also necessary that the user can identify all of the relevant damage model parameters associated with a particular damage model and with the studied material because the FLC program does not include a bank of pre-defined damage model parameters.

This is the first version of this software to be developed and implemented. In the future, it would be desirable to add more features to the program to make it more robust. For example, a useful addition would be the ability to apply different fatigue parameters to each node according to that node's temperature. This capability would enable more accurate predictions of fatigue life for the studied component to be developed. It would also be beneficial if the effects of accumulated damage could be incorporated by calculating the fatigue life at various stages throughout the temperature loading cycle of the component. This would also allow more accurate predictions of the fatigue life of the component. These changes would make the program more versatile. However, there is a drawback associated with these program upgrades; ultimately, the computational time needed to calculate the predicted fatigue life would increase substantially, perhaps to the point at which the time needed to obtain results may be uneconomical.

4.2 Results of Fatigue Life Prediction for the Test Specimen

4.2.1 Experimental Fatigue Life Results

The fatigue life experiments were performed at three strain amplitudes (0.005 mm/mm, 0.004 mm/mm, and 0.003 mm/mm) for all of the temperature conditions studied (25°C, 150°C, 200°C, and 250°C), except for the 300°C condition. For the 300°C condition, the strain amplitudes studied were 0.005 mm/mm, 0.006 mm/mm, 0.007 mm/mm, 0.008 mm/mm, and 0.009 mm/mm.

Due to the very high temperature of the 300°C condition, the material exhibits properties primarily within the plastic region; thus, the application of low strain amplitudes may not induce failure unless the test is performed over a very long period of time. The test duration required to induce failure at 300°C with strain amplitudes ranging from 0.003 to 0.005 mm/mm was not economically feasible for the research presented in this thesis; thus, the fatigue life tests for the high temperature condition of 300°C were conducted with higher strain amplitudes (from 0.005 to 0.009 mm/mm).

Figure 4.25 displays the strain amplitude trends observed in the test specimens under each temperature condition over the course of the corresponding fatigue life. The observed trends can be fit to a logarithmic curve in order to obtain the curve for the Basquin-Manson-Coffin damage model; the results obtained from the experimental tests are also shown in Table 4.1. The experimental data shown in Figure 4.25 were provided by the University of Michigan to determine the values of the parameters required for the damage models as well as for the comparison of fatigue life measures obtained under different conditions or with different methods.

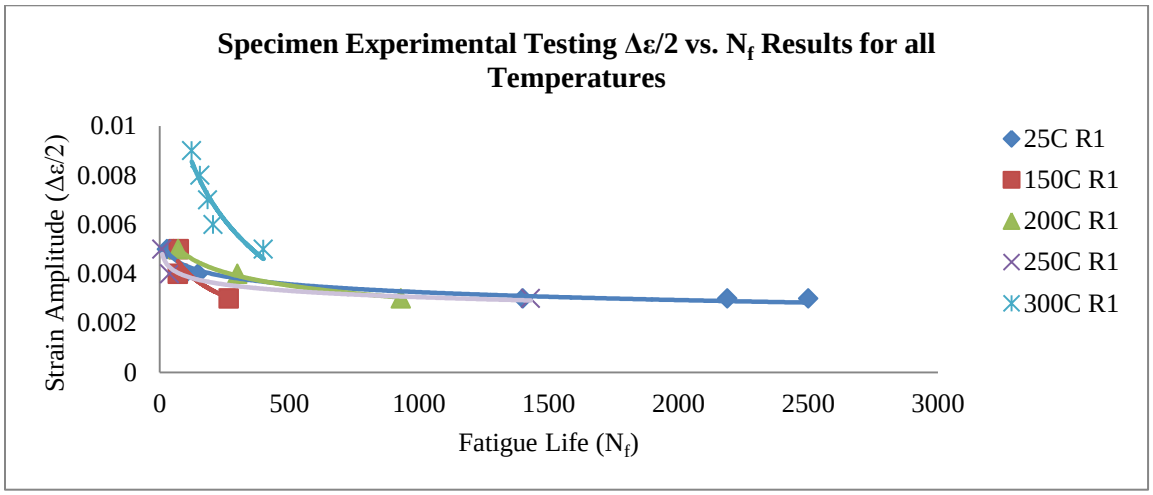

Figure 4.25: Strain Amplitude: Fatigue life trends observed during experimental testing of specimens for all temperatures at R1

Table 4.1: Summary of fatigue life findings based on experimental tests of specimens under various strain amplitude and temperature conditions.

Experimental Tests Fatigue Life Results									
25°C		**150°C**		**200°C**		**250°C**		**300°C**	
$\Delta\varepsilon$	**N_f**	**$\Delta\varepsilon$**	**N_f**	**$\Delta\varepsilon$**	**N_f**	**$\Delta\varepsilon$**	**N_f**	**$\Delta\varepsilon$**	**N_f**
0.005	28	0.005	74	0.005	72	0.005	9	0.009	123
0.005	37	0.004	70	0.004	300	0.004	38	0.008	155
0.005	54	0.003	267	0.003	930	0.003	1430	0.007	185
0.004	93							0.006	206
0.004	99							0.005	400
0.004	148							0.004	709
0.003	1400								
0.003	2188								
0.003	2500								

The number of data points for the 25°C conditions (n=3 for each strain amplitude tested at this temperature) is considered to be satisfactory for a first attempt in this thesis; however, more data points are required for the other four temperature conditions to demonstrate that the results are reliable. For this thesis, analysis and interpretation of this preliminary set of currently available fatigue data will be the focus of the research presentation, which can then be used to inform the design and interpretation of future research.

4.2.2 Results of Iso-thermal Specimen Simulation: Predicted Fatigue Life

To summarize the results obtained from the application of the damage models studied in this thesis, tables have been generated to compare the predicted fatigue life from model simulations of the test conditions with the experimental observations of fatigue life under these conditions; the experimental fatigue life values determined from physical testing of material specimens are compared to the predicted fatigue life of model specimens based on stabilized hysteresis loops derived from the ABAQUS simulation results (Table 4.2 to Table 4.4). Table 4.4 does not include results for the 300°C condition because no experimental data is currently available. The

Percent Error measures corresponding to each of the damage models examined are also displayed in the summary tables (Table 4.2 to Table 4.4).

Table 4.2: Comparison of experimental and predicted fatigue life for specimens at 0.005 mm/mm

Strain Amplitude (Δε/2)															
0.005															
Temp. (°C)	Exp.	Basquin-Manson-Coffin	% Error	SWT	% Error	Skelton	% Error	Von Mises	% Error	Morrow	% Error	ASME	% Error	Taira	% Error
25	40	52	30	51	28	39	3	38	5	52	30	98	145	43	8
150	74	63	15	64	14	83	12	54	27	63	15	78	5	108	46
200	72	96	33	56	22	86	19	71	1	97	35	129	79	106	47
250	9	7	22	7	22	10	11	5	44	7	22	8	11	9	0
300	400	360	10	360	10	393	2	303	24	360	10	371	7	361	10

Table 4.3: Comparison of experimental and predicted fatigue life for specimens at 0.004 mm/mm

Strain Amplitude (Δε/2)															
0.004															
Temp. (°C)	Exp.	Basquin-Manson-Coffin	% Error	SWT	% Error	Skelton	% Error	Von Mises	% Error	Morrow	% Error	ASME	% Error	Taira	% Error
25	113	198	75	194	72	91	19	149	32	200	77	420	272	109	4
150	70	153	119	155	121	74	6	134	91	153	119	202	189	131	87
200	300	262	13	257	14	401	34	196	35	263	12	393	31	435	45
250	38	21	45	21	45	43	13	13	66	21	45	27	29	32	16
300	709	582	18	581	18	651	8	490	31	581	18	604	15	730	3

Table 4.4: Comparison of experimental and predicted fatigue life for specimens at 0.003 mm/mm

Strain Amplitude (Δε/2)															
0.003															
Temp. (°C)	Exp.	Basquin Manson Coffin	% Err.	SWT	% Err.	Skelton	% Err.	Von Mises	% Err.	Morrow	% Err.	ASME	% Err.	Taira	% Err.
25	2029	2818	39	2618	29	1339	34	2338	15	2923	44	6913	241	1625	20
150	267	164	39	161	40	415	55	150	44	164	39	226	15	393	47
200	930	1707	84	1737	87	1511	62	1320	42	1694	82	3244	249	1253	35
250	1430	553	61	557	61	1474	3	224	84	552	61	1214	15	1321	8
300	-	-	-	-	-	-	-	-	-	-	-	-	-	-	-

Likewise, the following figures (Figure 4.26 through Figure 4.28) summarize the comparisons of the percent error found for all of the examined damage models for applied strain amplitudes of 0.005 mm/mm, 0.004 mm/mm, and 0.003 mm/mm, respectively. The closer that a bar in the graph is to a value of zero, the lower the percent error between the experimental and predicted fatigue life is for that condition. For some conditions, the percent error is high, and this high level of variation is associated with a lack of experimental data (very small sample size for some conditions). More experimental data (fatigue life and the corresponding strain amplitude) is required from specimens tested under the various experimental conditions. Increasing the sample size will enable the evaluation of more consistent and reliable damage model parameters, and improve the validity of damage models developed for the prediction of fatigue life for specimens constructed of various materials.

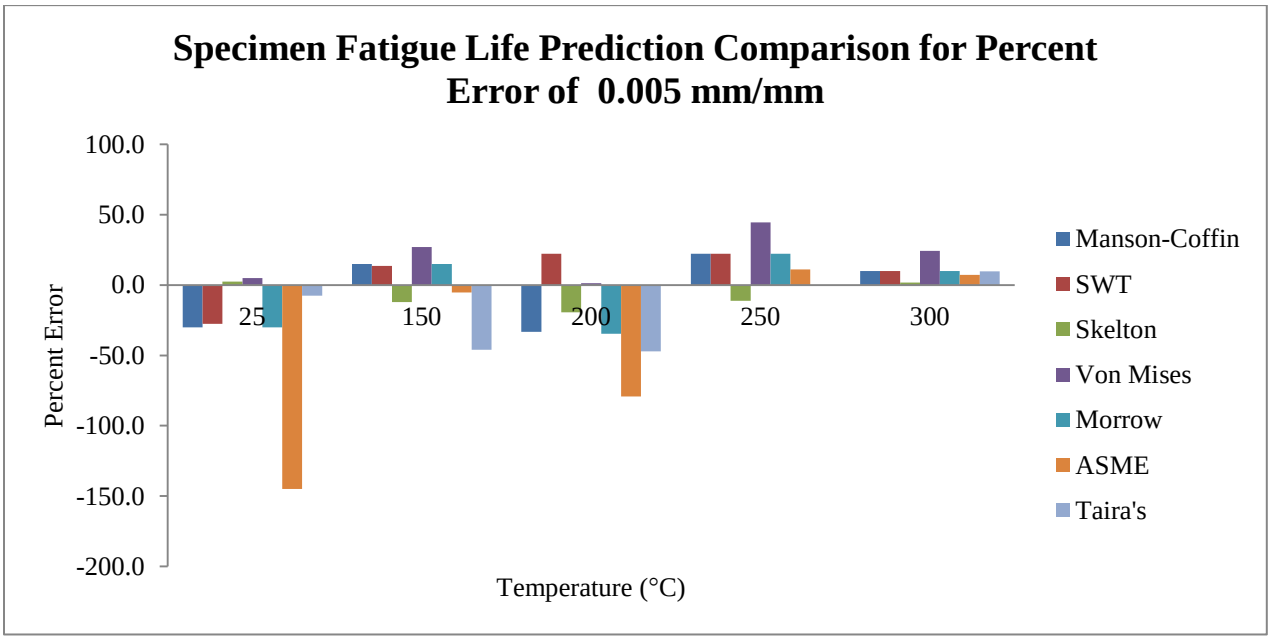

Figure 4.26: Iso-thermal specimen model fatigue life prediction percent error comparison of damage model predictions for R1 at 0.005 mm/mm

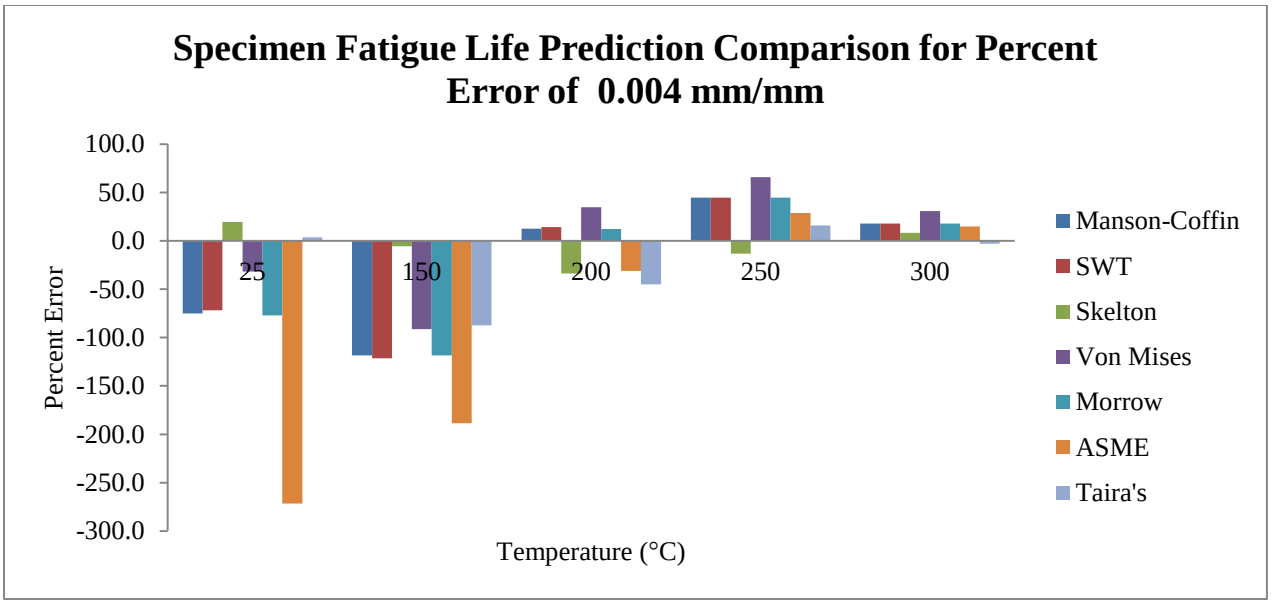

Figure 4.27: Iso-thermal specimen model fatigue life prediction percent error comparison of damage model predictions for R1 at 0.004 mm/mm

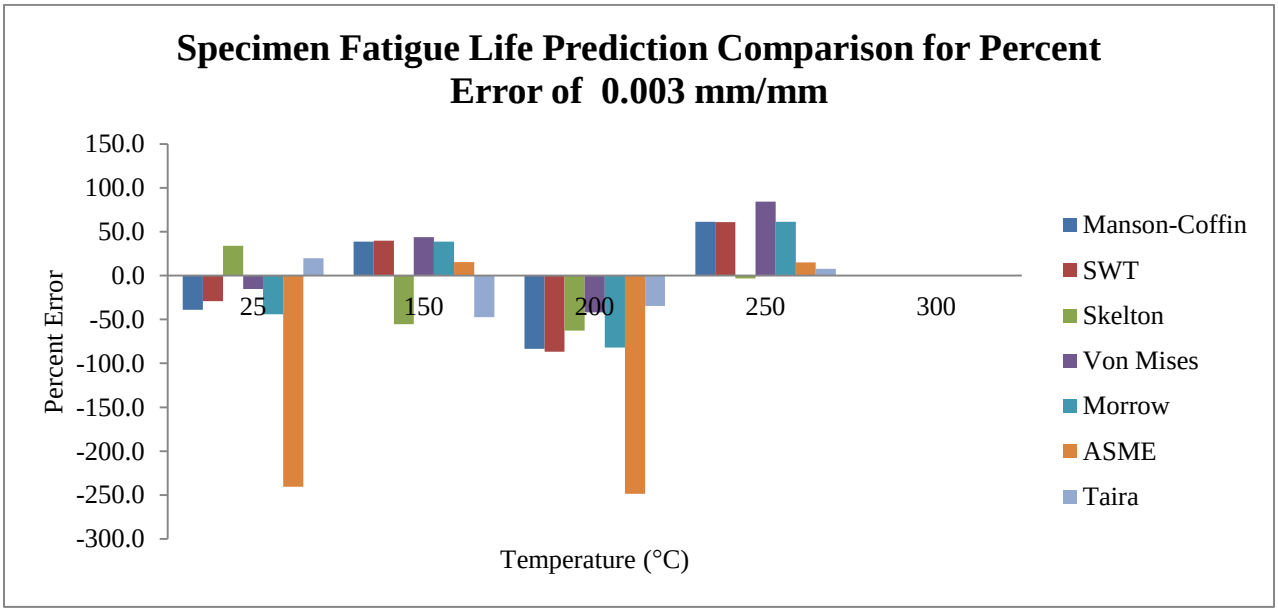

Figure 4.28: Iso-thermal specimen model fatigue life prediction percent error comparison of damage model predictions for R1 at 0.003 mm/mm

The most evident trend is that the fatigue life predictions of the ASME damage model are noteworthy in that they are excessively long for all strain amplitudes. The Basquin-Manson-Coffin, SWT, and Morrow models all provide relatively similar predictions for fatigue life; this was expected as there is almost zero σ_m. In cases where the Basquin-Manson-Coffin, SWT and

Morrow models provided overly long estimates of the fatigue life, the von Mises model generated a more accurate estimate of fatigue life. Conversely, the von Mises model produced inaccurate estimates of fatigue life when the predictions of the Basquin-Manson-Coffin, SWT, and Morrow models correlated strongly with the experimental results. The Skelton and Taira's models tended to produce predictions with relatively strong correlations to actual fatigue life observations for all temperature and strain amplitude conditions.

4.2.3 Results of In-Phase TMF Specimen Simulation Fatigue Life Predictions

Investigation of the predictions of the damage models for IP TMF loading conditions is similar to the examination of the fatigue life predictions for isothermal cyclic loading. Each of the damage models was applied to the IP TMF specimen simulation. Unlike the isothermal fatigue life predictions, which were based on parameters for a single temperature condition, the fatigue life predictions for IP TMF conditions were performed using both the 200°C and the 250°C damage model parameters. The fatigue life of specimens exposed to IP TMF was predicted using these two parameters because the average cycle temperature was 225°C. Developing a fatigue life prediction routine that incorporates fatigue life estimates based on multiple temperature conditions at various times during the test is complex, and would also require a large amount of processing power. The level of processing power and the complexity of the processes required to accomplish this task are currently unattainable. Thus, a simplified approach based on the damage model parameters for 200°C and 250°C (which approximate the average cycle temperature of 225°C) to represent a full IP TMF cycle will be followed in this thesis. show the predicted IP TMF fatigue life obtained from the various damage models and the percent error obtained when comparing the fatigue life observed experimentally to the estimates of fatigue life derived from simulation. The fatigue life for specimens experiencing TMF was determined using the FLC.

Table 4.5 and Table 4.6 show the predicted IP TMF fatigue life obtained from the various damage models and the percent error obtained when comparing the fatigue life observed experimentally to the estimates of fatigue life derived from simulation. The fatigue life for specimens experiencing TMF was determined using the FLC.

Table 4.5: IP TMF specimen simulation: Fatigue life predictions of various damage models using the 200°C damage model parameters.

IP TMF Specimen Model Life Predictions - 200°C Parameters		
Damage Model	**Fatigue Life (Cycles)**	**Percent Error (%)**
Experimental	107	-
Basquin-Manson-Coffin	16	85
SWT	9	92
Morrow	18	83
Skelton	5	95
Von-Mises	11	90
ASME	17	84
Taira's	93	13

Table 4.6: IP TMF specimen simulation: Fatigue life predictions of various damage models using the 250°C damage model parameters.

IP TMF Specimen Model Life Predictions - 250°C Parameters		
Damage Model	**Fatigue Life (Cycles)**	**Percent Error (%)**
Experimental	107	-
Basquin-Manson-Coffin	3	97
SWT	2	98
Morrow	3	97
Skelton	5	95
Von-Mises	2	98
ASME	3	97
Taira's	96	10

The fatigue life that was obtained for IP TMF from experimental testing was 107 cycles. Figure 4.29 shows the degree of deviation of the predicted fatigue life from the observed fatigue life during experimental tests. Comparison of the predicted results to the experimental observations

indicates that 6 of the 7 damage models examined were inaccurate (i.e., very high percent error). This inaccuracy is likely due to the fact that the estimates of fatigue life for these 6 damage models were based on isothermal criteria instead of IP TMF criteria (due to the high level of complexity and processing power required, as noted previously). These six damage models do not include a temperature damage factor, so the predicted fatigue life is based to a great extent on the Δε. This is not the case for the Taira's model, which is a TMF prediction application that includes a temperature damage factor. The Taira's model predicted the fatigue life conservatively, and underestimated fatigue life by approximately 10% when compared to the experimental observations of fatigue life.

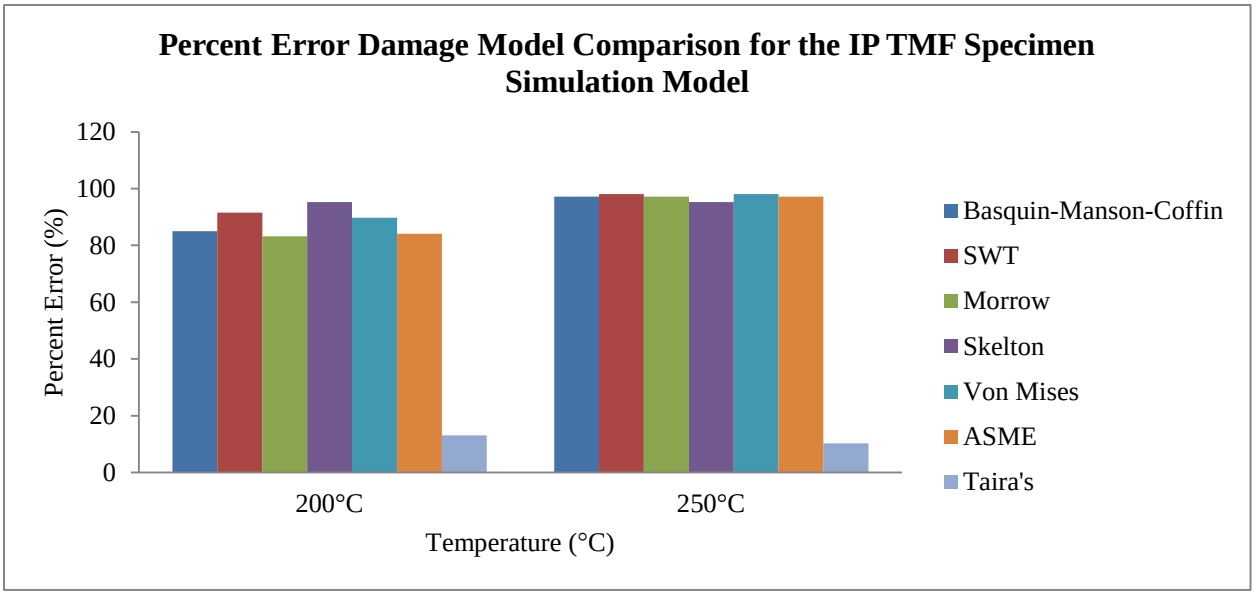

Figure 4.29: Percent error comparison of damage model predictions for the IP TMF specimen simulation.

4.2.4 Discussion of the Basquin-Manson-Coffin Fatigue Life Prediction Results

As mentioned earlier, the Basquin-Manson-Coffin approach is based entirely on the assumption that the Δε is the primary influence on fatigue life. This method is only applicable for uniaxial loading conditions. This model is one of the oldest damage models used to predict fatigue life, and a great deal of research has been reported that support its claims. However, there are some

other important influences that should also be considered when predicting fatigue life that are not included in the Basquin-Manson-Coffin approach. Some of the influences that should also be considered under different loading situations are the effects of applied stress and the effects associated with elevated temperatures. Although the Basquin-Manson-Coffin is a good starting point, its findings should be compared to other damage models that may better represent the impact of the experimental conditions on a particular specimen.

Fatigue life was predicted based on the value of the $\Delta\varepsilon/2$ obtained from the simulated hysteresis loops. Fatigue life estimates rely heavily on the damage model parameters, and thus, the reliability of these parameters is extremely important. With only limited data available, the reliability of the experimental data used to derive the damage model parameters and the associated predictions of fatigue life are not certain. However, the approach taken to determine the fatigue life follows sound engineering practice for limiting the potential for error in other areas of research. When comparing the predicted fatigue life for isothermal conditions with experimental results for the Basquin-Manson-Coffin approach, the results appear to correlate strongly with a slight reduction in accuracy as the strain amplitude is decreased. This discrepancy is due to the fact that as the strain amplitude becomes smaller, the Basquin-Manson-Coffin curve becomes more horizontally linear. A small change in the $\Delta\varepsilon/2$ can lead to a very large change in N_f. This can make it very difficult to accurately predict fatigue life associated with small $\Delta\varepsilon/2$ because the margin for error becomes much smaller. For TMF life predictions, the Basquin-Manson-Coffin model was inaccurate.

4.2.5 Discussion of Smith-Watson-Topper Fatigue Life Prediction Results

Another damage model that was investigated was the SWT approach, which is a modification of the Basquin-Manson-Coffin model that attempts to capture the effects of σ_{max}. In the case of the

specimens studied in this thesis, the effects of σ_{max} had very little effect on the predicted fatigue life. The fatigue life predictions of the SWT model for isothermal conditions were very similar to those predicted by the Basquin-Manson-Coffin model. Likewise, a similar pattern was evident for these two models with a decrease in the $\Delta\varepsilon/2$; in both cases, the accuracy of the fatigue life predictions declined. The SWT model was also inaccurate in its predictions of TMF life, usually predicting values for fatigue life for TMF conditions that were too low.

4.2.6 Discussion of Skelton Fatigue Life Prediction Results

The Skelton model is an energy-based approach; instead of using measures of the parameter, $\Delta\varepsilon$, to determine fatigue life, predictions of fatigue life with the Skelton model are based on measures of dissipated energy. The fatigue life predictions for isothermal cyclic loading conditions obtained with this damage model were consistent with the test measures of fatigue life obtained under experimental isothermal cyclic loading conditions. This improved level of accuracy is because the fatigue life is determined on with measures of energy dissipation rather than measures of $\Delta\varepsilon$. For example, if the simulated hysteresis loop involves a different level of $\Delta\varepsilon$ with a correlated and equivalent alteration in $\Delta\sigma$ during cyclic loading, the energy dispersed by the hysteresis loop will remain stable. Since the dispersed energy is stable, the corresponding predicted fatigue life will also remain stable despite the difference in the $\Delta\varepsilon$ level. There is one downfall to this approach; the value of *n'* is required, so a complete hysteresis loop must be assessed for the loading and unloading of the component. The Skelton model is less accurate for TMF conditions, and predicts values for fatigue life that are much lower than the predictions of other damage models.

4.2.7 Discussion of Morrow Fatigue Life Prediction Results

The Morrow damage model is a modification of the Basquin-Manson-Coffin model that captures any effects due to offset of the σ_m. The values obtained for the σ_m were presented in Chapter 3, and were almost negligible for the test specimens. Nevertheless, they were incorporated into the calculation of fatigue life using the Morrow model for comparison with other damage models. As would be expected, the fatigue life predictions of the Morrow model were very similar to those of the Basquin-Manson-Coffin and SWT models. All of these models are relatively the same, with only minor differences. Consequently, the amount of deviation (% error) from the isothermal experimental measures of N_f for the predictions of the Morrow model is approximately the same as the level of error observed for the predictions of the Basquin-Manson-Coffin and the SWT damage models. Likewise, a pattern of under-estimating the fatigue life for TMF conditions was observed for the Morrow model, which is consistent with the outcomes for other isothermal damage models.

4.2.8 Discussion of von Mises Fatigue Life Prediction Results

The von Mises model is one of the two multi-axial fatigue damage models studied in this thesis. A strong correlation between the $\Delta\varepsilon$ measure and the N_f was observed for isothermal cyclic loading conditions. For example, if the discrepancy (percent error) in the $\Delta\varepsilon$ between the experimental and simulated hysteresis loops was large, then the deviation (percent error) between the experimental and simulation fatigue life predictions was also large. This implies that, for isothermal cyclic loading conditions, the accuracy of the fatigue life predictions of the von Mises model is heavily dependent upon the accuracy of the material model. Accordingly, the results obtained from the application of this damage model are generally acceptable apart from a few conditions in which the predicted fatigue life varied from the experimental fatigue life. It is

expected that with the addition of more experimental testing more accurate damage model parameters can be obtained, increasing the accuracy of the studied damage models (von Mises included). For TMF conditions, the fatigue life predictions of the von Mises model were very conservative.

4.2.9 Discussion of ASME Fatigue Life Prediction Results

The remaining multi-axial damage model examined in this thesis is the ASME model, which tended to over-estimate fatigue life. If the accuracy of the material model is high, then using this approach will lead to overly optimistic results. For example, if the $\Delta\varepsilon$ measures for the isothermal experimental and the simulated hysteresis loops are approximately equal, then the ASME model will predict a higher fatigue life than the experimentally determined fatigue life. However, if the material model is flawed, so that the $\Delta\varepsilon$ of the simulated isothermal hysteresis loop is smaller than the experimental measure of $\Delta\varepsilon$, then the model's predicted fatigue life will be more similar to the experimental fatigue life. Thus, the accuracy of this model's fatigue life predictions depends on the input of erroneous information for the damage model parameters. Furthermore, extreme caution should be used when applying this damage model because when it produces incorrect fatigue life predictions, they tend to be wildly over-estimated as can be seen in the comparisons of the damage model predictions presented in Chapter 4 (Table 4.9).

4.2.10 Discussion of Taira's Fatigue Life Prediction Results

The final damage model studied was the Taira's model. Although this model is also a strain-based model, it includes the effects of temperature, which the other examined strain-based models do not include. The pattern of the results obtained from the application of this method appear to be among the most consistent outcomes of the methods studied. The fatigue life

predictions of Taira's model included some of the most accurate findings (lowest percent error) observed for any of the studied damage models, under both isothermal and TMF conditions.

4.3 Cylinder Head Simulation

This section summarizes the method employed to implement a TMF condition on a industry cylinder head. A discussion of each step of the simulation including the boundary conditions is included in this section. The cylinder head model that was used in this research is for a four cylinder engine, used in passenger car applications. The geometry is complex, shown in Figure 4.30, consisting of 1,060,558 nodes and 606,862 elements. The element used to mesh the cylinder head is C3D10M tetrahedral.

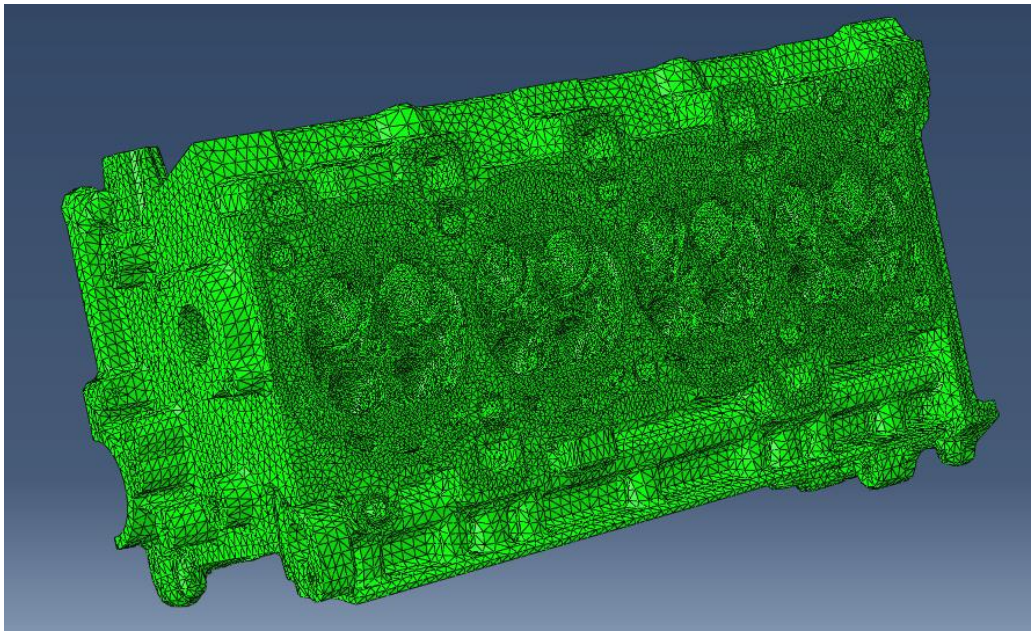

Figure 4.30: Meshed cylinder head: View is of the hot side (combustion chambers) of the cylinder head, which consists of 1,060,558 nodes and 606,862 elements.

The simulation was performed in 8 steps. Each step includes calculation of the stress and strains according to specific boundary conditions applied to the cylinder head.

Step 1

This is the pre-assembly step. In the pre-assembly step, contact constraints are applied to the model. The contact constraints are situated between the cylinder head itself and other foreign materials that are part of the final components assembly, such as the cylinder head bolts.

Step 2

This is the assembly step, in which the appropriate loads are applied to the cylinder head bolts.

Step 3

In this step, the thermal load is applied; a temperature field is applied on a nodal basis to the cylinder head model. This temperature field represents the temperature levels experienced by the cylinder head under operating conditions.

Steps 4 to 7

These steps include the application of cylinder pressure to each of the cylinders in the order of engine firing, and represent the combustion phenomena. During these steps, the temperature field is maintained at operating conditions.

Step 8

Thermal load removal occurs during this step. The temperature field is removed from the cylinder head model, and all nodes are then returned to room temperature (27°C) conditions.

4.3.1 Application of the Cylinder Head Temperature Field

A temperature field was applied to the cylinder head in order to replicate operating conditions. For each of the nodes that make up the cylinder head model, a unique temperature value was assigned. The temperature field was determined by performing a finite element thermal analysis

using boundary conditions evaluated at Centro Ricerche FIAT. This analysis was performed using GT POWER for the temperature distribution due to air flow and three dimensional computational fluid dynamics analysis for the temperatures in the cooling channels. Temperature distributions from the application of the thermal loading step at various locations in the cylinder head are illustrated in the following figures (Figure 4.31 to Figure 4.34). The highest temperatures (approximately 242°C) are located in the exhaust runner.

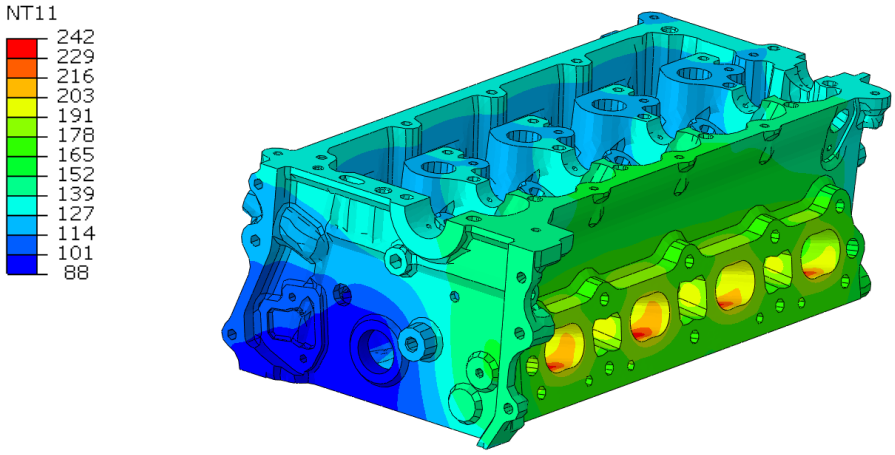

Figure 4.31: Temperature field distribution throughout the cylinder head. The dark blue region represents the coldest temperature and the red region represents the hottest temperature. Maximum operating temperature is approximately 242°C.

The temperature distribution in the exhaust runner (where maximum temperatures occur) is shown in Figure 4.32.

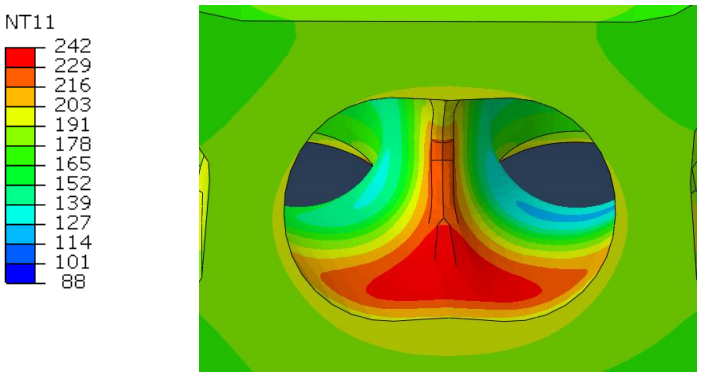

Figure 4.32: Cylinder head exhaust runner temperature field distribution. Maximum temperature of 242°C occurs at the base of the runner.

The section view in Figure 4.33 shows the temperature distribution found in the cooling channels of the cylinder head. This region experiences some of the coolest operating temperatures due to the engine coolant.

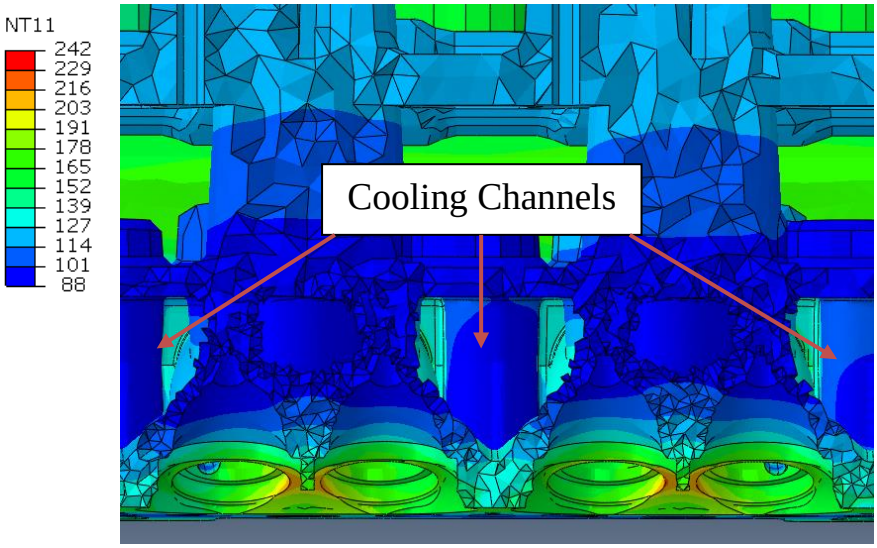

Figure 4.33: Cylinder head cooling channel temperature field distribution. In this figure, the cylinder head has been sectioned in half. This shows cooling channels used to cool the combustion chambers of the cylinder head.

Combustion chamber temperature distribution is shown in Figure 4.34. The highest temperature (approximately 220°C) in the combustion chamber occurs on the valve bridge connecting the two exhaust runners.

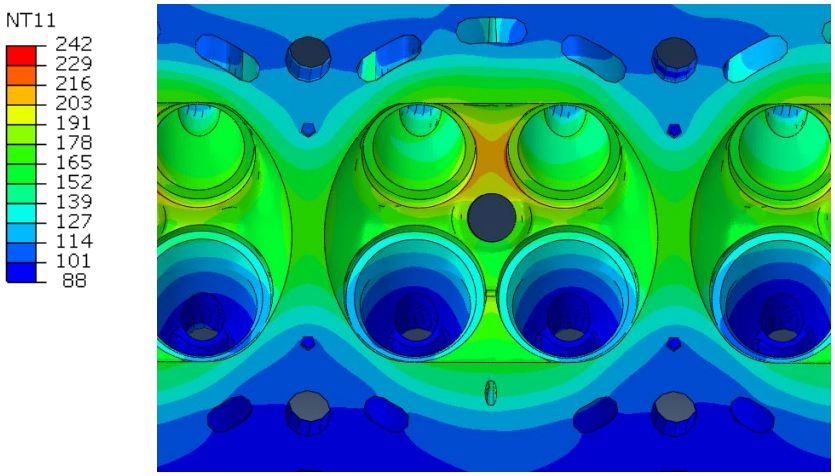

Figure 4.34: Cylinder head combustion chamber temperature field distribution. In this region, the highest temperature of approximately 220°C occurs on the exhaust valve bridge.

4.3.2 Cylinder Head Critical Locations for Predicted Fatigue Life

Critical locations were identified by determining the strain amplitudes between two steps and plotting them on a contour map of the cylinder head. The steps from which the strain amplitudes were determined are: after the thermal loading application, and after the thermal loading removal. The critical areas were also determined for different directions of loading. For example, the critical areas were identified in the x, y, z, minimum principal, middle principal, and the maximum principal directions. Using principal strains as a direction of loading is a useful approach for capturing multi-axial loading with uniaxial damage models.

Four critical areas were identified for the cylinder head. The critical areas were determined by the maximum strain amplitude found for each direction of loading. A detailed description of these four critical areas follows:

Critical Area 1

Figure 4.35 identifies the critical location (location of probable failure) due to loading in the x-direction; this site is on the valve bridge, and is located between the intake valves. In this region, there is a concentration of stress due to the geometrical design that may be contributing to this area's probability of failure.

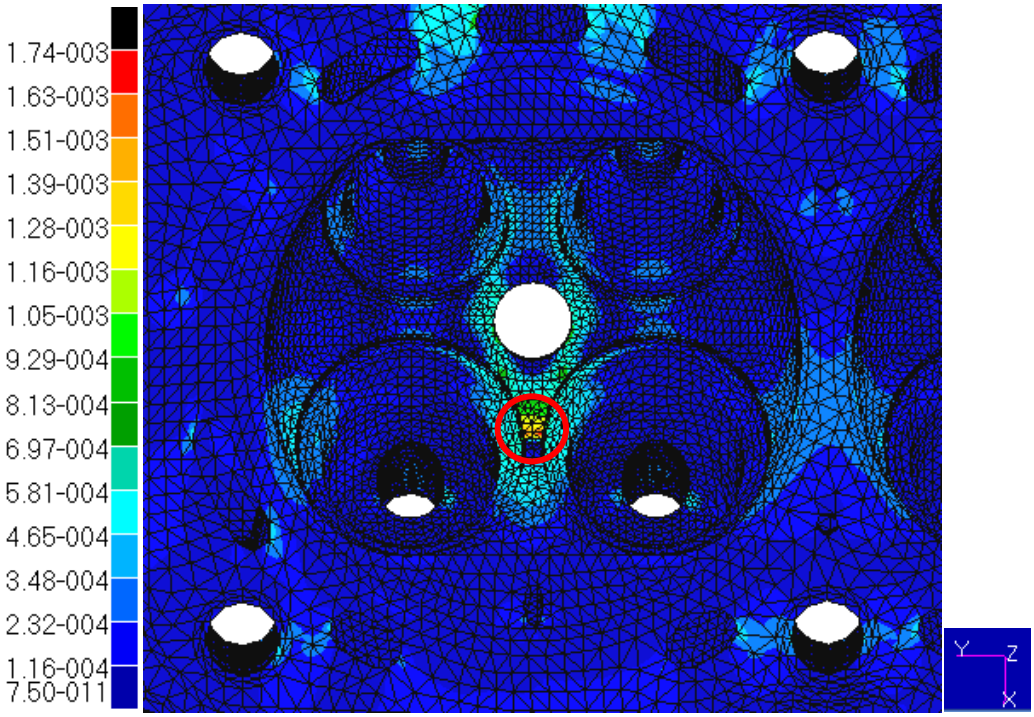

Figure 4.35: Cylinder head critical location due to x-direction loading. Location of failure occurs on the valve bridge between the intake valves. The legend indicates the values of strain amplitudes. The maximum strain amplitude is 0.00174 mm/mm.

Figure 4.36 provides an alternative view of the stress concentration located on the valve bridge between the intake valves. In this region, a change to the geometry could potentially reduce the adverse effects of the concentrated stress at the critical location.

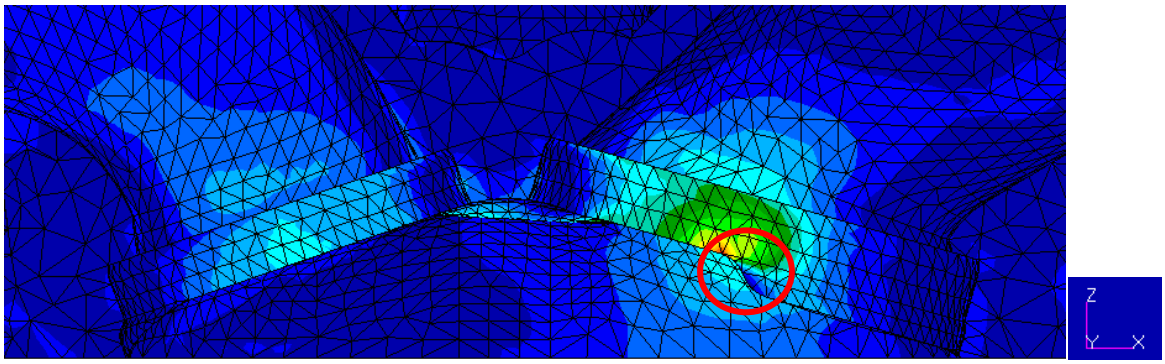

Figure 4.36: Cylinder head stress concentration contributing to x-direction failure. The highlighted area shows the radius in the geometry that could be contributing to part failure. The maximum strain amplitude for this direction of loading is 0.00174 mm/mm.

Critical Area 2

For loading in the y-direction, the critical location for probable failure occurs on the base of the exhaust runner. This location is identified by the red circle in Figure 4.37. This area experiences one of the largest temperature fluctuations, as shown in Figure 4.32.

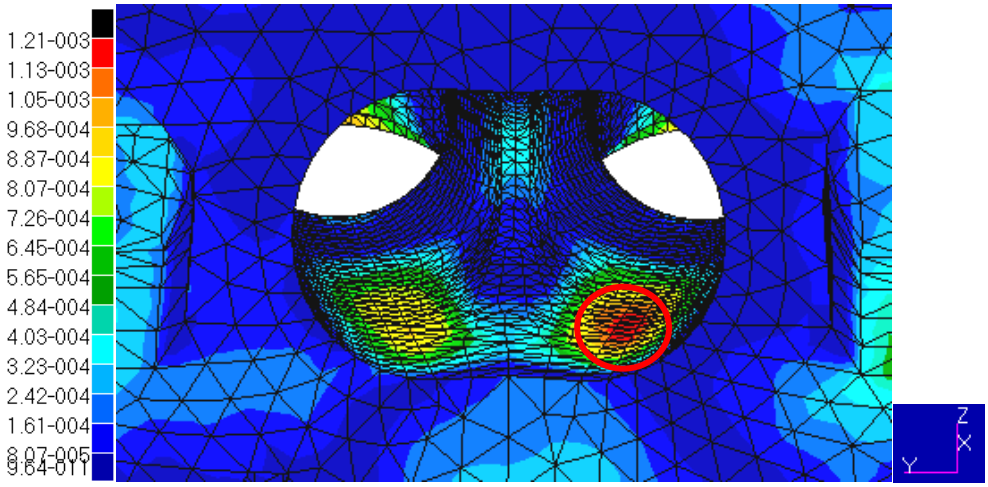

Figure 4.37: Cylinder Head critical location due to y-direction loading. The highlighted area at the base of the exhaust runner shown is the critical location for failure. The strain amplitude in this area is 0.00121 mm/mm.

Critical Area 3

The critical area due to loading in the z-direction and the minimum principal direction is located in the region where the two exhaust runners converge, as shown in Figure 4.38. This area has a sharply defined edge where the exhaust runners converge, causing a very high stress concentration at this location.

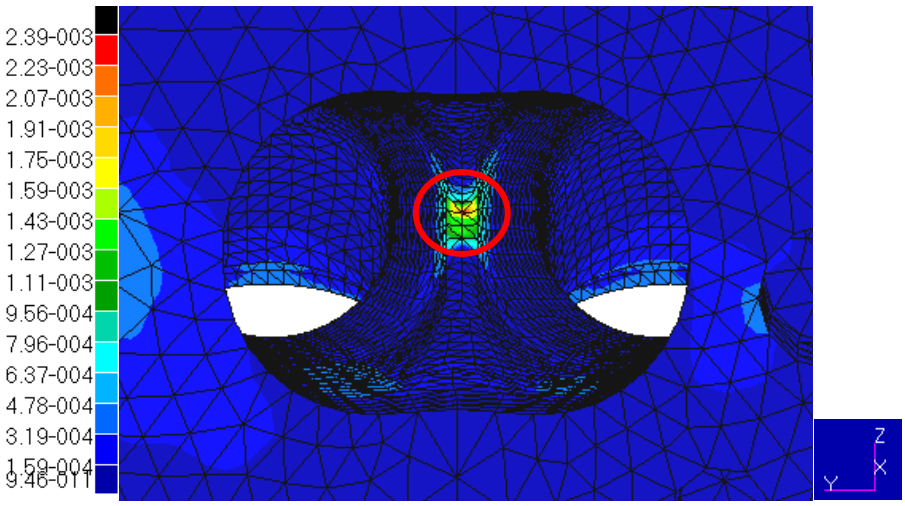

Figure 4.38: Cylinder head critical location due to z-direction and minimum principal strain loading. The highlighted area at the convergence of the exhaust runner is the critical location for failure. The strain amplitude in this area is 0.00239 mm/mm.

Critical Area 4

The critical areas for probable failure due to maximum and middle principal strains are located in approximately the same area. This region is located on the inside of the cooling channel, which is highlighted within the red circle shown in Figure 4.39. This stress concentration occurs in response to geometry that allows the cylinder head bolts to clamp the cylinder head to the engine block.

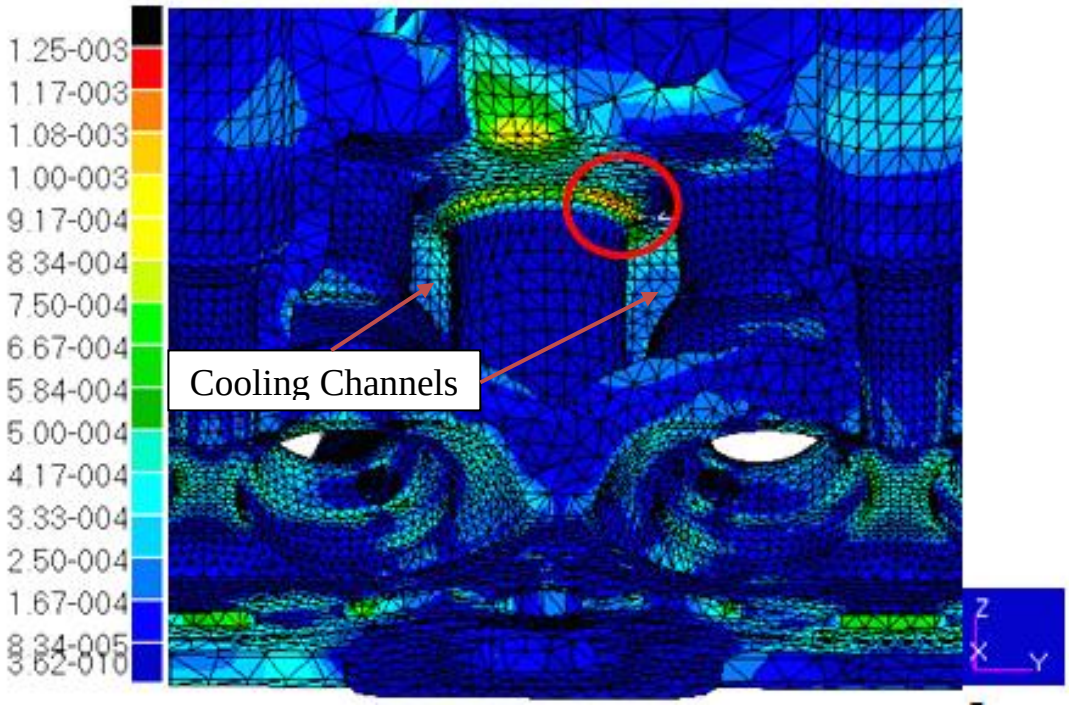

Figure 4.39: Cylinder Head critical location due to maximum and middle principal strain loading. The highlighted area in the cooling channels is the critical location for failure for these directions of loading. The strain amplitude in this area is approximately 0.00125 mm/mm.

4.3.3 Identification of the Nodes for Critical Fatigue Areas

In order to use the identified critical areas with the FLC program, the fatigue life needs to be predicted for specific nodes. For each identified critical area, the node experiencing the highest strain amplitude was selected for the prediction of fatigue life. Table 4.7 identifies the nodes that represent the critical areas, and includes a brief description of the location.

Table 4.7: Identification of the critical nodes within areas of probable failure and description of the location.

Cylinder Head Critical Node Locations	
X-Direction	
Node Number	**Description of Location**
266892	Across Intake Valve Bridge
Y-Direction	
Node Number	**Description of Location**
313397	In base of exhaust runner
Z-Direction	
Node Number	**Description of Location**
183136	Stress concentration that links exhaust runners
Minimum Principal Direction	
Node Number	**Description of Location**
183136	Stress concentration that links exhaust runners (Same as z-direction)
Mid Principal Direction	
Node Number	**Description of Location**
165802	Stress Concentration area in Cooling channel
Maximum Principal Direction	
Node Number	**Description of Location**
165769	Stress Concentration area in Cooling channel (Same as Mid. Prin. Direction)

4.3.4 Cylinder Head Simulation Model: Fatigue Life Prediction Results

The fatigue life for the nodes in the identified critical regions was predicted using the FLC program to apply 6 damage models; following is a list of the applied damage models:

- Basquin-Manson-Coffin
- Smith-Watson-Topper
- von Mises
- Morrow
- ASME
- Taira's

Unlike the fatigue life predictions for the material specimens, the Skelton damage model was not applied to the fatigue life predictions for the model cylinder head because the simulation only calculates results for certain states of operation. The stress and strain were only calculated at the initial and maximum operating conditions; the lack of data for intermediate conditions prohibits the construction of a full hysteresis loop, and thus prevents the calculation of *n'*.

Using the most fundamental aspect of all of the damage models, displays the Δε/2 associated with each direction of loading. This measure represents the critical node based on its direction of loading and the corresponding Δε/2 value.

Table *4.8* displays the Δε/2 associated with each direction of loading. This measure represents the critical node based on its direction of loading and the corresponding Δε/2 value.

Table 4.8: Cylinder head Δε/2 based on the associated node and direction of loading.

Loading Direction	Damage Model		
	Basquin-Manson-Coffin, SWT, Morrow, Taira's	von Mises	ASME
	Δε/2		
165769 - X-Direction	0.00174	N/A	N/A
165802 - Y-Direction	0.00121	N/A	N/A
183136 - Z-Direction	0.00239	N/A	N/A
183136 - Min. Prin.	0.00247	N/A	N/A
266892 - Mid. Prin.	0.00041	N/A	N/A
313397- Max. Prin.	0.00115	N/A	N/A
165769 - Multi-Axial	N/A	0.00232	0.00644
165802 - Multi-Axial	N/A	0.00081	0.00208
183136 - Multi-Axial	N/A	0.00238	0.00235
266892 - Multi-Axial	N/A	0.00016	0.00511
313397 - Multi-Axial	N/A	0.00132	0.00180

The fatigue life was predicted for loading in the x, y, z, minimum principal, middle principal, and the maximum principal direction using the FLC program. The node that produced the most critical fatigue life predictions was Node 183136, located at the convergence point of the exhaust

runners. The location of this region is graphically highlighted in Figure 4.38. At this location, failure is most likely to occur in the z or minimum principal direction of loading.

Figure 4.40 compares the predictions of fatigue life by the various uniaxial damage models for the critical nodes. The figure shows the critical nodes and their respective direction of loading with the fatigue life predicted by each of the damage models. In most cases, the predicted fatigue life is greater than the FLC maximum (2,000,000), resulting in a prediction of infinite life. Consequently, the y-axis of the graph was limited to a more realistic maximum value of 10^3 cycles (LCF cut-off). It is evident that the most critical node, and the only node predicted to have a short fatigue life by all of the damage models, is Node 183136; this finding is consistent with the results presented in Table 4.8. The von Mises and ASME damage model predictions involve multi-axial approaches to the prediction of fatigue life. The fatigue life predictions of the multi-axial damage models for the critical nodes are shown in Figure 4.41; the predictions were consistent for most nodes, but diverged for Node 266892 as the ASME model predicted a markedly reduced fatigue life for this critical node, and the von Mises model did not.

The fatigue life predictions of all of the damage models were completed using the 150°C and 200°C damage model parameters. The parameters for these temperature conditions were chosen because the average temperature observed between each thermal loading state was approximately 135°C, which is more closely represented by the 150°C experimental data than the 200°C data. However, the damage model parameters derived from the experimental data for 200°C produced a more reliable pattern in the predictions of the examined damage models than the parameters for 150°C. This is likely due to discrepancies in the experimental data. The available experimental data for 150°C is unreliable and inconsistent due to an apparent outlier for

the Δε/2 measure at 0.004mm/mm. Consequently, until more experimental testing takes place, fatigue life predictions will be determined with both sets of parameters. The predictions based on the 200°C condition are presented in Figures 4.40 and 4.41, and those based on the 150°C parameters are presented in Figures 4.42 and 4.43.

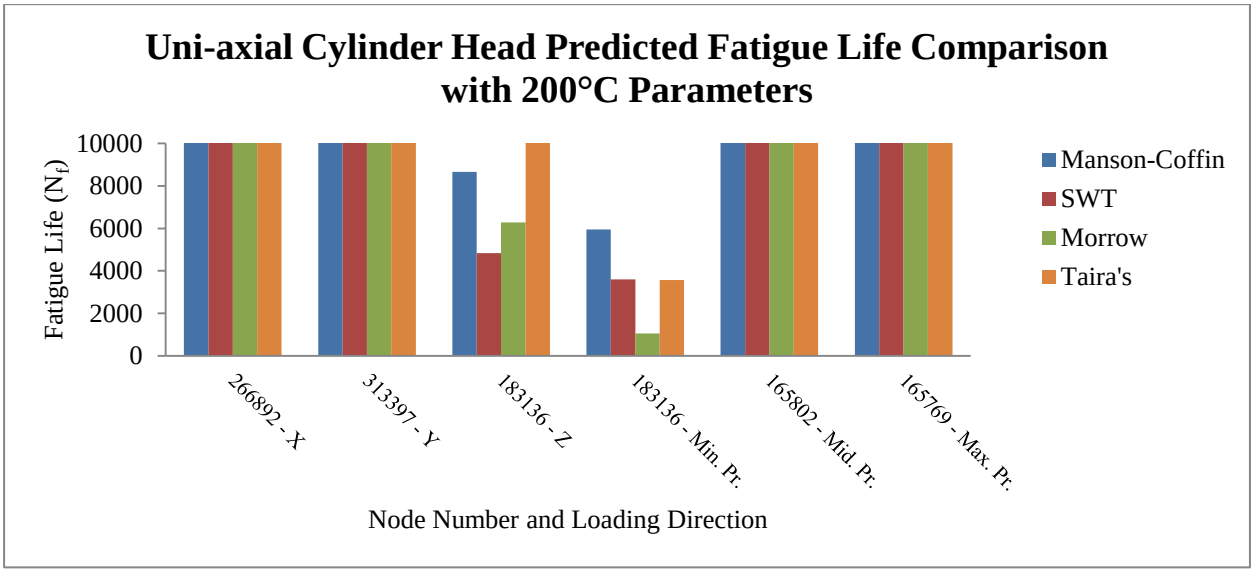

Figure 4.40: Cylinder head uniaxial fatigue life predictions with 200°C parameters.

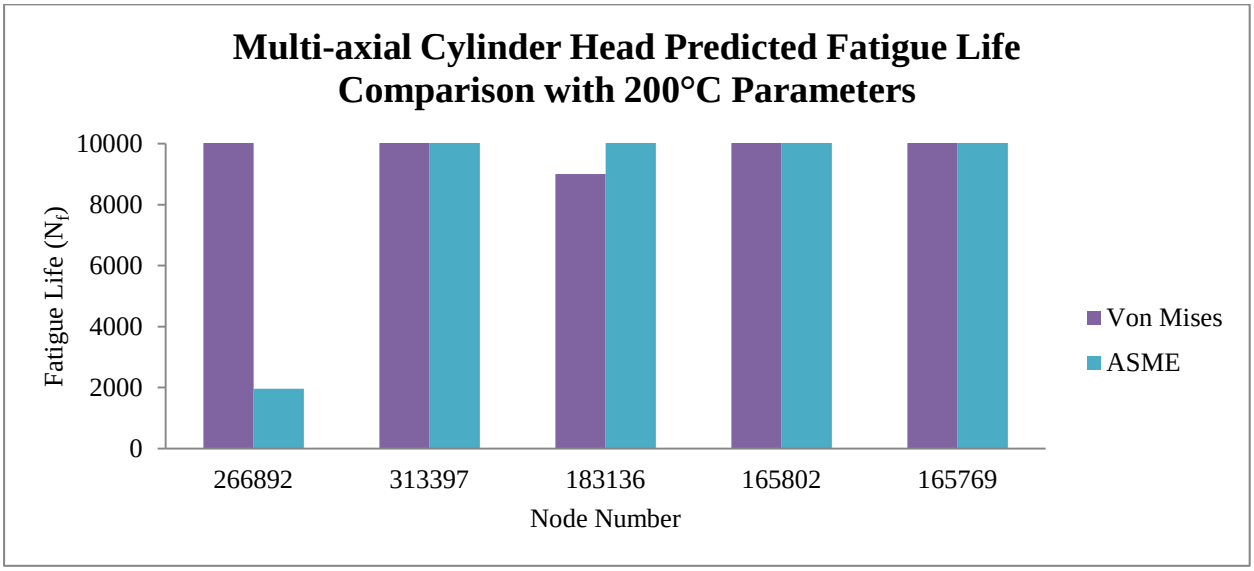

Figure 4.41: Cylinder head multi-axial fatigue life predictions with 200°C parameters

The results obtained from the FLC program for the most critical node (183136) are summarized in Table 4.9. As the von Mises and ASME models are multi-axial damage models, they produce only one value for the predicted fatigue life, whereas the uniaxial damage models produce predictions for both of the specified loading directions.

Table 4.9: Summary of calculated fatigue life predictions for node 183136 with 200°C parameters

	Direction of Loading	
Damage Model	**Z**	**Minimum Principal**
Basquin-Manson-Coffin	8658	5948
SWT	4839	3596
Morrow	6284	1049
Taira's	522990	3572
Von Mises (Multi-Axial)	9001	
ASME (Multi-Axial)	23300	

Figure 4.42 and Figure 4.43 show the comparison of fatigue life predictions for the critical node using various damage models with the 150°C damage model parameters. In general, the findings differ from the predictions made using the 200°C damage parameters. The predictions from the various damage models are less consistent, but the predicted fatigue life is generally lower for the 150°C condition. The S-N curve for the 150°C condition predicts shorter fatigue life for the same $\Delta\varepsilon/2$ value that resulted in the longer fatigue life predicted by the 200°C curve. One pattern that is evident under both conditions is that Node 183136 is the most critical node according to most damage models. Node 266892 is also a more evident concern according to several damage models (uniaxial and multi-axial) when the 150°C parameters were applied to the prediction of fatigue life.

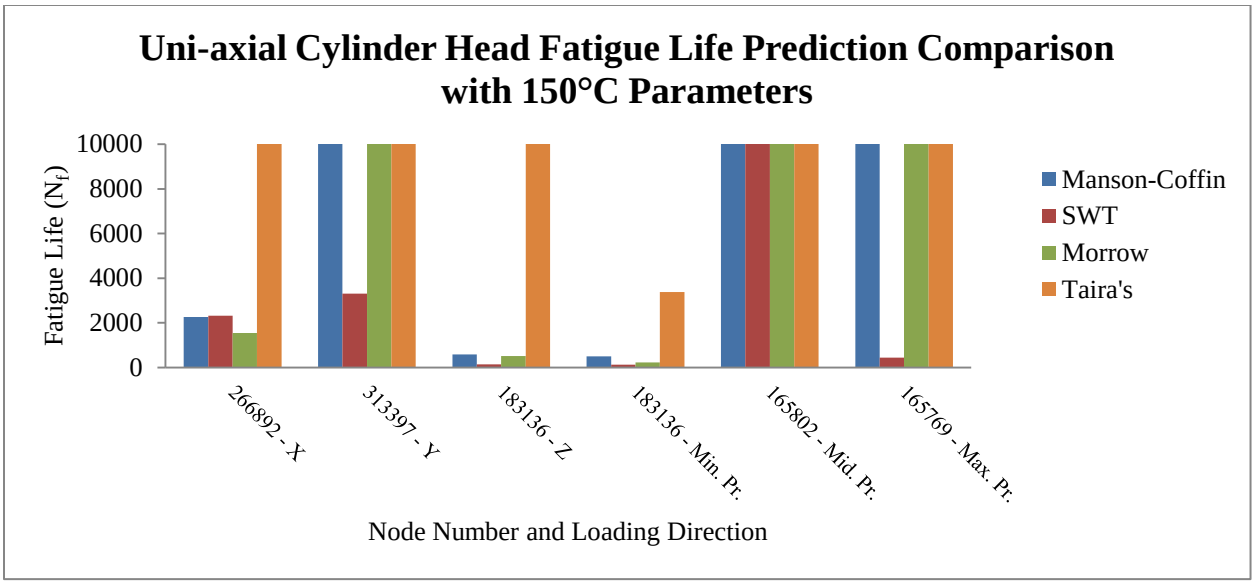

Figure 4.42: Cylinder head uniaxial fatigue life predictions with 150°c parameters.

A trend that is apparent in the multi-axial fatigue life predictions for the 150°C condition is that the ASME model predicts much lower fatigue life than the von Mises model because the ASME model calculated a higher Δε/2 value for this temperature condition than the von Mises model.

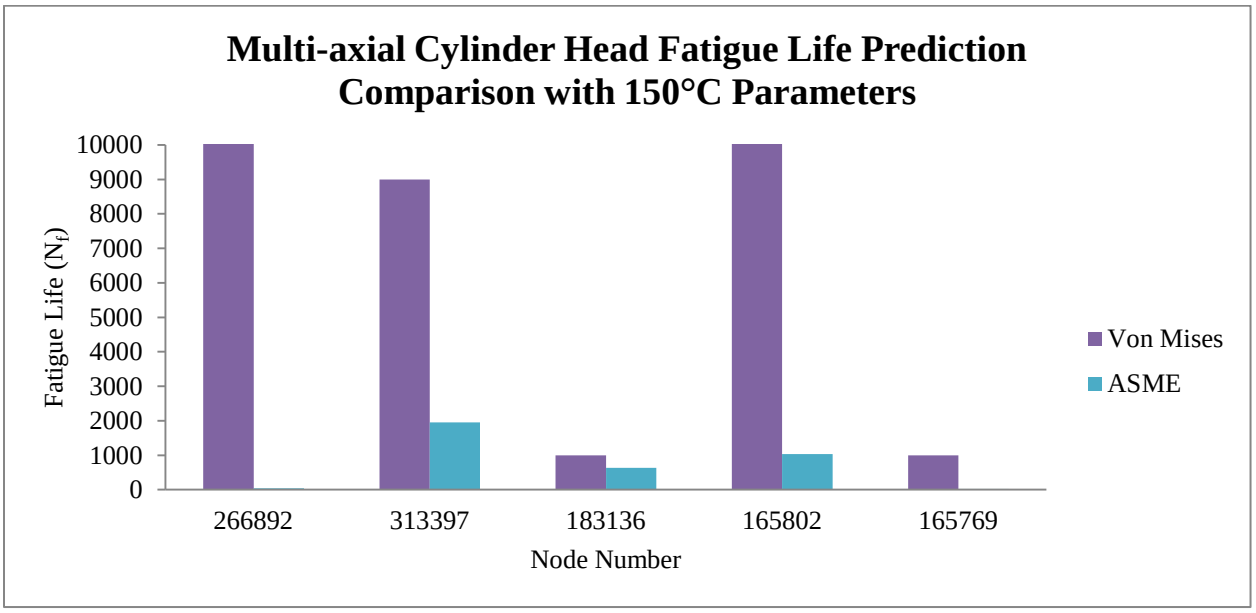

Figure 4.43: Cylinder head multi-axial fatigue life predictions with 150°C parameters.

The predictions for fatigue life obtained from the FLC program for the most critical node (183136) with the 150°C parameters applied to various uniaxial and multi-axial damage models are summarized in Table 4.10.

Table 4.10: Summary of predicted fatigue life for node 183136 with 150°C parameters.

	Direction of Loading	
Damage Model	**Z**	**Minimum Principal**
Basquin-Manson-Coffin	593	499
SWT	143	123
Morrow	510	222
Taira's	239633	3374
Von Mises (Multi-Axial)	1001	
ASME (Multi-Axial)	635	

4.4 Discussion of Cylinder Head Simulation Model: Fatigue Life Prediction Results

The following sections examine possible reasons for discrepancies between the fatigue life predictions for the studied damage models and the predictions of the Basquin-Manson-Coffin damage model. The damage model findings are compared to the Basquin-Manson-Coffin results because the Basquin-Manson-Coffin model is the original equation from which most of the other damage models are derived. Note that there is no currently available experimental data for the cylinder head in the model simulations that can be used to directly validate the damage models (i.e., by comparing the simulation results to reliable test results obtained for cylinder head specimens under all of the experimental conditions considered in this thesis research); direct validation of potentially useful damage models would be an objective of future research.

4.4.1 Discussion of Model Comparison (Smith-Watson-Topper Fatigue Life Predictions)

The SWT model is a modification of the Basquin-Manson-Coffin model. This model, like the Basquin-Manson-Coffin model, includes the parameters for strain range ($\Delta\varepsilon$) and the maximum stress (σ_{max}). In the z-direction, the σ_{max} was 186.2 MPa, and in the minimum principal direction,

the σ_{max} was 189.6 MPa. When the values for σ_{max} were included (i.e., the SWT equation), the predictions for fatigue life were slightly lower than the values predicted by the Basquin-Manson-Coffin damage model. Thus, inclusion of the effects of σ_{max} leads to slightly more conservative predictions of fatigue life for the conditions considered in this study.

4.4.2 Discussion of Model Comparison (Morrow Fatigue Life Predictions)

The Morrow damage model includes the effects of mean stress (σ_{mean}), and is also a modification of the Basquin-Manson-Coffin model. The σ_{mean} in the z-direction was 15.5 MPa, and in the minimum principal direction, σ_{mean} was 92.9 MPa. If the σ_{mean} was zero, then the predicted results will be identical to those predicted by the Basquin-Manson-Coffin damage model. Thus, if the $\Delta\varepsilon$ is equivalent, then the σ_{mean} is the factor that differentiates the fatigue life predictions for the Morrow and Basquin-Manson-Coffin damage models. For the conditions considered in this thesis, the outcomes of the Morrow model tended to be similar relative to the predictions of the Basquin-Manson-Coffin damage model. Using the 150°C parameters the predicted fatigue lives were very close. However, when using the 200°C parameters the predicted fatigue lives varied more when loading was considered in the minimum principal direction.

4.4.3 Discussion of Model Comparison (von Mises Fatigue Life Predictions)

The von Mises model employs a multi-axial approach to determine a measure of equivalent strain amplitude (i.e., calculates this parameter with the von Mises equivalent amplitude relationship). This equivalent strain amplitude value is then applied to the Basquin-Manson-Coffin model. Thus, the difference between the outcomes of the von Mises and Basquin-Manson-Coffin models is dependent upon the equivalent amplitude. For the conditions considered in this thesis, the outcomes of the von Mises model tended to be very close using

200°C parameters and about half when using the 150°C parameters, when related to the predictions of the Basquin-Manson-Coffin damage model.

4.4.4 Discussion of Model Comparison (ASME Fatigue Life Predictions)

The ASME damage model is similar to the von Mises model; they are both multi-axial models that determine and include a parameter for equivalent strain amplitude, which is applied to the Basquin-Manson-Coffin model to predict the fatigue life of a component. Thus, the relative differences between the fatigue life predictions of the Basquin-Manson-Coffin model and the ASME model fatigue lives are dependent upon the value of the equivalent strain amplitude calculated from the ASME relationship. For the conditions considered in this thesis, the outcomes of the ASME model tended to be very close using 150°C parameters and approximately double when using the 200°C parameters, when related to the predictions of the Basquin-Manson-Coffin damage model.

4.4.5 Discussion of Model Comparison (Taira's Fatigue Life Predictions)

This damage model is not based upon the Basquin-Manson-Coffin model, and thus a direct comparison of the specific elements that differentiate the models cannot be made (as in sections 5.6.1 to 5.6.4). Nevertheless, the most evident discrepancy between the predictions of Taira's model and the other uniaxial damage models can be seen in Figures 142 and 144 for Critical Node 183136 (particularly for loading in the z-direction). This is likely due to the location of node 183136 (exhaust runner), which experiences some of the highest operating temperatures. So, using the Taira's model, damage associated with temperature can be captured, however, temperature damage cannot be captured with the Basquin-Manson-Coffin model. This can lead to very different fatigue life predictions.

Chapter 5 Conclusion and Future Recommendations

This thesis reviewed several aspects of TMF material model development and the calculation of fatigue life predictions in conditions that feature temperature variation and cyclic loading. Presentation of the content of this thesis follows the steps taken to reach the final objective of developing an effective AL319-T7material model and method for predicting the fatigue life of cylinder heads constructed of a particular material and exposed to TMF-inducing conditions (variations in temperature and cyclic loading at several strain rates). The final conclusions for each of the key components of this thesis are presented in the following order: experimental testing, available experimental data, material model development theory, material model development, validation of material models, implementation of the FLC program routine, fatigue life prediction results for material specimens, cylinder head simulations and fatigue life predictions, and future recommendations.

5.1 Conclusions

1. Experiments for this thesis were conducted at the University of Michigan. The experiments were performed over five temperature levels (25, 150, 200, 250, and 300 °C) and at three strain rates ($5x10^{-5}$, $5x10^{-4}$, and $5x10^{-3}$ mm/mm/s). The strain rates have been assigned identifiers R1, R2, and R3, respectively. Experiments were conducted using three different approaches, including iso-thermal monotonic loading (tensile only), iso-thermal cyclic loading (tension and compression), and TMF cyclic loading (tension and compression with varied temperature). The experimental equipment used for this was an MTS servo hydraulic silent flow flex test 40 equipped with a 100 kN load capacity. Strain measurements were taken at the middle of the hour glass shape of the test specimen using

an MTS extensometer. The stress was determined by comparing the load applied by the MTS servo hydraulic silent flow flex test 40 and the cross-sectional area of the test specimen. Tests were performed on two different specimens that have different dimensions to comply with ASTM E606 standards.

2. All of the monotonic loading tests of material specimens at three strain rates have been completed. For the isothermal and TMF cyclic loading conditions, only R1 experiments have been completed. For 25°C experiments a sample size of three was used, for all other temperatures a sample size of one was used. Furthermore, only the IP TMF experimental results were completed and presented in this thesis. No experimental testing was conducted on the cylinder head to validate the outcomes of the simulation studies on model specimens of the cylinder head. Data collection was problematic under some conditions; for example, many specimens were destroyed during TMF cyclic loading experiments due to low quality test results, severely curtailing the availability of specimens for more isothermal and TMF experiments. Performing TMF specimen experiments is a very difficult task, now that the ability to perform usable TMF test data is known, more iso-thermal and TMF specimens can be performed in the future when test specimens become available
3. Two material models were developed to replicate the material properties of the aluminum alloy, AL319-T7; the material model parameters were derived from test data of material specimens of AL319-T7. One material model represents monotonic loading of this material and the other represents cyclic loading of this material. The material model used to characterize monotonic loading was isotropic hardening. A combined hardening model, comprised of kinematic and isotropic hardening, was used to characterize cyclic

loading. This was the first attempt to accurately predict fatigue life for TMF using only a combined hardening material model, and neglecting the effects of creep and oxidation. The material models that were developed were used in ABAQUS to represent the material properties of AL319-T7 during later stages of the study. The procedures used to develop the material models and apply them in ABAQUS proved to be effective and feasible, based on material model validations (Section 3.5).

4. All of the monotonic loading material models and their simulations have been completed and validated. Validation was performed by comparing the areas under the experimental and simulation σ-ε curves. The discrepancies between the outcomes for the test material and the simulated material were generally <10%, and so are considered to be acceptable according to FIAT standards. Currently, R1 material models have been developed for cyclic loading conditions. Validation of these cyclic loading material models was performed by comparing the dissipated energy for the hysteresis loops from simulations and experiments; these models were also considered to have an acceptable level of error. Generally less than 10% difference between experimental and simulation hysteresis loops. Thus, it was concluded that the R1 cyclic loading material model was appropriate for simulating isothermal and TMF cyclic loading in model specimens of the material under the relevant experimental conditions.
5. The first version of the FLC program is currently operational, and is returning acceptable results for predicted fatigue life of both the material specimen and the model cylinder head. This program was developed, so that it can import an ABAQUS report file (for model specimens based on the material models developed for this study; see Conclusion 3) and predict fatigue life according to the following damage models: Basquin-Manson-

Coffin, SWT, Skelton, Morrow, von Mises, ASME, and Taira's models. After predicting the fatigue life for each node, the FLC program creates an output file that is readable in MSC Patran, which can generate a new contour map on the meshed part of the model specimen. This contour map enables the user to identify and locate critical areas of the model specimen that are based on fatigue life. In general, the FLC program is fully functional within the specific limits entailed by the objectives of the current research. Several potential modifications have been identified that would enable the FLC program to be used more broadly (e.g., in conjunction with other FEA software applications).

6. Fatigue life predictions were performed for material model specimens for the 0.005 mm/mm, 0.004mm/mm, and 0.003 mm/mm strain amplitudes, and the following damage models were applied: Basquin-Manson-Coffin, SWT, Skelton, von Mises, Morrow, ASME, and Taira's models. In general, as the strain amplitudes decreased and the number of fatigue life cycles increased, the strain-based damage models became less accurate for the work in this thesis. This increase in error matched the development of a horizontally linear S-N curve. Based on comparisons of the predicted fatigue life (and % error) from various damage models, the Skelton damage model appears to be the most accurate model for fatigue life predictions due to its better correlation to experimental results. However, the Skelton damage model requires more parameters that need to be determined from experimental data, so this damage model may not be economically feasible under some circumstances. The results calculated from simulations based on the Basquin-Manson-Coffin, SWT, and Morrow models were comparable because the mean stress values were very low for the conditions examined, so did not differentiate the outcomes from these models. The ASME damage model over-estimated the fatigue life

for most of the conditions examined. The predictions of the von Mises model correlated well with experimental results (i.e., low % error) for the conditions in which the predictions of the Basquin-Manson-Coffin, SWT, and Morrow models did not (i.e., high % error). However, this was reversed if the predicted results for the Basquin-Manson-Coffin, SWT, and Morrow models strongly correlated with experimental results. To determine which damage model predicts fatigue life the best is difficult, conclusions upon the best model at predicting fatigue life should be determined for each experimental condition. The predicted fatigue life for simulations of the TMF condition found that the predictions of the Basquin-Manson-Coffin, SWT, Skelton, Morrow, von Mises, and ASME damage models all markedly under–estimated fatigue life. However, the fatigue life prediction based on Taira's model was much closer to the fatigue life determined experimentally. This is most likely due to the fact that Taira's model is a TMF damage model that includes a temperature damage factor, whereas the other damage models do not.

7. A simulation was conducted with the AL319-T7 combined hardening material model applied to the model cylinder head. Using these simulation results, the fatigue life was predicted with the FLC program. Measures of fatigue life were predicted using all of the damage models, except for the Skelton model, which requires a parameter derived from a complete hysteresis loop. The cylinder head simulation only determines results for the maximum and minimum loading conditions; results are not determined for intermediate loading conditions, so a complete hysteresis loop cannot be constructed from the simulation data, and the cyclic hardening exponent required by Skelton damage model cannot be derived. Four critical locations of potential failure were identified in the

cylinder head. The most critical area was located at the convergence of the two exhaust runners. The predominant trend observed in the isothermal specimen simulations, in which the results for the Basquin-Manson-Coffin, SWT, and Morrow damage models were all similar, was also observed for the cylinder head simulations. Likewise, under TMF cyclic loading conditions, Taira's model predicted slightly larger values for fatigue life; this was also the case for the cylinder head simulation results, and the results obtained for this damage model were more accurate than the other uniaxial damage models. When comparing the multi-axial damage models, the von Mises model predicted higher values for fatigue than the ASME model. In fact, the ASME model predicted fatigue life measures that were comparable to the predictions of the Basquin-Manson-Coffin model. In general, although based on incomplete and preliminary data, the model comparisons suggest that the Taira's model is likely to be the best damage model when attempting to predict TMF life.

8. The overall conclusion of this thesis is that the accuracy of the experimental results is low due to the lack of repeatability of the results. The lack of experimental repeatability was due to many test specimens being destroyed during the initial phase of testing at the University of Michigan. The material models developed for both monotonic and cyclic loading conditions returned strong correlations (less than 10% error in most cases) when comparing simulation and experimental stress-strain curves. The comparison of the predicted fatigue lives with the experimental fatigue lives showed overall strong correlation, thus proving that the damage model parameters are reliable for cylinder head fatigue life predictions. Four critical locations of failure were identified for the cylinder head, the most critical predicted fatigue life is approximately on average 5000 cycles.

Based on a rough estimate of two cycles a day the cylinder head will remain free of any crack initiation for nearly seven years.

5.2 Future Recommendations

In future, it is essential that additional isothermal and TMF cyclic loading tests are performed to ensure that data from an appropriate number of specimens has been collected for each of the experimental conditions considered in this study; currently, there is no cyclic loading test data for some strain rates and the data collected for some experimental conditions is based on a single specimen. The additional test data will improve the consistency and reliability of the results used to derive model parameters. After obtaining reliable experimental data, the damage model parameters should be re-calibrated using the new, and complete, set of test data. This should provide more consistent and reliable predictions of the fatigue life of a component when these damage models are implemented. Likewise, the re-calibrated measures of the damage model parameter should be more accurate and valid estimates. Consequently, the fatigue life predictions should also be more accurate when the appropriate damage model is chosen to simulate the experimental conditions. It is also recommended that experimental fatigue tests be performed on specimens of the cylinder head. Initially, these tests should focus on the critical areas determined in this thesis research. This will allow comparison of test results with simulated fatigue life predictions for the cylinder head based on various damage models. This will serve to validate the damage models, and also inform model selection to ensure that the appropriate damage model is chosen to represent the experimental conditions under investigation. The FLC program should also be further developed to increase the robustness of the program, and improve its functionality and flexibility, so that it can used with other FEA software applications, and damage models.

References

[1] P. Suresh. 2004. Fatigue of Materials Second Edition. Cambridge University Press 2004.

[2] K. Mocellin, M. Ferraro, V. Velay, R. Logé, F. Rézai-Aria. Numerical Life Prediction Of Mechanical Fatigue For Hot Forging Tools.

[3] R.P. Skelton, C.J. Rees and G. A. Webster. Energy Damage Summation Methods For Crack Initiation and Growth During Block Loading In High-Temperature Low-Cycle Fatigue. Fatigue Fract. Engng Mater. Struct. Vol. 19, No. 2/3, 1997, 287-297

[4] Budynas R, Nisbett J. 2011. Shigley's Mechanical Engineering Design Ninth Edition. McGraw-Hill 2011.

[5] M. A. Meggiolaro, J. T. Pinho de Castro. A Critical Evaluation of Fatigue Crack Initiation Parameter Estimates. The Society of Automotive Engineers. 2004-01-2219.

[6] J.D. Morrow. Cyclic Plastic Strain Energy and Fatigue of Metals. Internal Friction, Damping, and Cyclic Plasticity - ASTM STP 378. American Society for Testing and Materials, Philadelphia, PA, 1964, 45-87

[7] R.P. Skelton. Energy Criterion for High Temperature Low Cycle Fatigue Failure. The Institute of Metals. Vol. 7,1991, 427-439

[8] R.N. Smith, P. Watson, and T.H. Topper. A Stress-Strain Parameter for the Fatigue of Metals. *Journal of Materials,* Vol. 5, No. 4, 1970, 767-778

[9] N.E. Dowling. Mean Stress Effects in Stress-Life and Strain-Life Fatigue. The Society of Automotive Engineers. F2004/51

[10] [7] R.P. Skelton, T. Vilhelmsen, G.A. Webster. Energy Criteria and Cumulative Damage During Fatigue Crack Growth. Elsevier. Vol. 20, No. 9,1998, 641-649

[11] Abaqus Reference Manual

[12] J Lemaitre and J. L. Chaboche. Mechanics of Solid Materials. Cambridge University Press, New York, NY, USA, 2000.

[13] Crack Initiation/ Strain Life (ε-N) Analysis http://www.mscsoftware.com/training_videos/patran/Reverb_help/index.html#page/Fatigue%2520Users%2520Guide/fat_theory.15.4.html (Accessed April 2013)

[14] H.T. Kang, Y.L.Lee, J. Chen, D.Fan. A Thermo-mechanical Fatigue Damage Model for Variable Temperature and Loading Amplitude Conditions. Internatinal Journal of Fatigue. 2007, 1797-1802

[15] Ince A., Glinka G. 2011. A Modification of Morrow and Smith-Watson-Topper Mean Stress Correction Model, Fatigue & Fracture of Engineering Materials & Structures. 2011

[16] Delprete C., Sesana R., Vercelli A. 2010. Multiaxial damage assessment and life estimation: application to an automotive exhaust manifold. Fatigue – Elsevier. 2010

[17] Delprete C, Rosso C. Exhaust manifold thermo-structural simulation methodology. *SAE Technical Paper* 2005; 2005-01-1076

[18] ASME. Class 1: components in elevated temperature service. Cases of ASME Boiler and Pressure Vessel Code, Section III, Division 1, Appendix T, New York, 1988. pp. 97 and 104

[19] Taira S. 1973. Relationship Between Thermal Fatigue and Low-Cycle Fatigue at Elevated Temperature. Fatigue at Elevated Temperatures, ASTM STP 520, American Society for Testing and Materials. 1973, pp. 80-101.

[20] Sehitoglu H., Engler-Pinto Jr. C.C., Maier H., Foglesong T. Thermo-Mechanical Fatigue of Cast 319 Aluminum alloys.

[21] D. Socie, B. Socie. 2007. Thermomechanical Fatigue Made Easy. Fatigue. 2007

[22] J. Machacek. Fatigue of Steel Structures. http://people.fsv.cvut.cz/~machacek/prednaskyOK3E/OK3-5E.pdf. Accesed August 19 2013.

[23] J. Svoboda. 1982.Fatigue and Fracture Toughness of Five Carbon or Low Alloy Cast Steels at Room or Low Climate Temperature. Carbon and Low Alloy Steel Technical Research Committee Steel Founders' Society of America. No. 94A,1982.

[24] Z. Lopez. 2012. Correlations among Tensile and Cyclic Deformation Properties for Steels and Implications on Fatigue Life Predictions. The University of Toledo. 2012.

[25] S. Trampert, T. Gocmez, S. Pischinger. 2008. Thermomechanical Fatigue Life Prediction of Cylinder Heads in Combustion Engines. Journal of Engineering for Gas Turbines and Power. 2008.

[26] M. Grieb, H-J. Christ, B. Plege. 2010. Thermomechanical Fatigue of Cast Aluminum Alloys for Cylinder Head Applications – Experimental Characterization and Life Prediction. Fatigue. 2010.

[27] F. Dunne, N. Petrinic. 2005. Introduction to Computational Plasticity. Oxford 2005.

[28] Key to Metal - True Stress - True Strain Curve: Part Four. http://www.keytometals.com/page.aspx?ID=CheckArticle&site=kts&NM=279 (Accessed September 2013)

Appendix A: Developed Material Model Parameters

In the tables below the parameters that represent the monotonic and cyclic loading material models can be found. These parameters were determined with the ABAQUS calculation method that was discussed in this thesis.

A.1 Monotonic Loading Material Models

A.1.1 R1 Material Models

Table A.1: Monotonic Material Model for 25°C R1

25°C R1	
Elastic Properties	
Young's Modulus (MPa)	Poisson's Ratio
76027	0.33
Plastic Properties	
True Stress (MPa)	Plastic Strain (mm/mm)
180.77	0
184.41	0.0001
186.87	0.0002
189.45	0.0003
191.86	0.0004
193.92	0.0005
196.19	0.0006
198.13	0.0007
200.03	0.0008
201.78	0.0009
203.32	0.001
205.02	0.0011
206.22	0.0012
207.78	0.0013
209.12	0.0014
210.37	0.0015
211.74	0.0016
213.04	0.0017
214.15	0.0018
215.29	0.0019
216.4	0.002
217.56	0.0021
218.39	0.0022
219.61	0.0023
255.04	0.0073

264.54	0.0093
272.25	0.0113
278.76	0.0133
284.02	0.0153
288.03	0.0173

Table A.2: Monotonic Material Model for 150°C R1

150°C R1	
Elastic Properties	
Young's Modulus (MPa)	Poisson's Ratio
69764	0.33
Plastic Properties	
True Stress (MPa)	Plastic Strain (mm/mm)
140.312649	0
165.568589	0.002489614
175.0526948	0.002782511
181.6637296	0.002989989
185.2480348	0.003146575
188.7895351	0.003491423
196.55387	0.004757797
208.382848	0.007297061
213.2910683	0.009175963
217.4158399	0.010901889
221.6525827	0.012751525
224.6191312	0.020009007

Table A.3: Monotonic Material Model for 200°C R1

200°C R1	
Elastic Properties	
Young's Modulus (MPa)	Poisson's Ratio
70867	0.33
Plastic Properties	
True Stress (MPa)	Plastic Strain (mm/mm)
50.02845528	0
101.029085	0.001352287
130.649596	0.001848457
140.1815221	0.002046525
150.126261	0.002377772
155.1447164	0.00260938
160.0591298	0.003065778
165.0389317	0.003761793
166.4923116	0.004120958
170.0143454	0.004944025
175.0290518	0.006970841
180.0384175	0.010141679
181.5079332	0.013611269

Table A.4: Monotonic Material Model for 250°C R1

250°C R1	
Elastic Properties	
Young's Modulus (MPa)	Poisson's Ratio
53604	0.33
Plastic Properties	
True Stress (MPa)	Plastic Strain (mm/mm)
50.89852325	0
100.2510276	0.001850789
105.2903321	0.002043884
109.4656837	0.002271639
111.5236121	0.002580223
115.5184107	0.003301053
120.5686809	0.005313378
123.4616891	0.008432257
122.5124524	0.011073503
122.3836171	0.014680567
119.1644191	0.016523638

Table A.5: Monotonic Material Model for 300°C R1

300°C R1	
Elastic Properties	
Young's Modulus (MPa)	Poisson's Ratio
52241	0.33
Plastic Properties	
True Stress (MPa)	Plastic Strain (mm/mm)
50.14052385	0
68.12680719	0.001318022
69.14066987	0.001534513
70.21416015	0.00172324
70.96305	0.002362775
73.75591035	0.004222147
75.60455347	0.00652497
76.1337303	0.008719431
76.40265814	0.016245382
74.97595185	0.020007729

A.1.2 R2 Monotonic Material Models

Table A.6: Monotonic Material Model for 25°C R2

25°C	
Elastic Properties	
Young's Modulus (MPa)	Poisson's Ratio
81818	0.33
Plastic Properties	
True Stress (MPa)	Plastic Strain (mm/mm)
161.0176367	0
200.2090484	0.000202176
225.8381382	0.000482647
250.0784165	0.00115543
275.1051163	0.003043182
300.0687615	0.006655446
325.0311546	0.013588265
330.0204455	0.016007452
333.165674	0.018783289

Table A.7: Monotonic Material Model for 150°C R2

150°C	
Elastic Properties	
Young's Modulus (MPa)	Poisson's Ratio
72033	0.33
Plastic Properties	
True Stress (MPa)	Plastic Strain (mm/mm)
175.1945753	0
200.0821182	0.000390933
212.9380014	0.000695416
230.0287545	0.003276261
240.0215906	0.006290756
250.0489343	0.011815933
255.0031139	0.016619918
257.180377	0.021773579
254.289436	0.02626834

Table A.8: Monotonic Material Model for 200°C R2

200°C R1	
Elastic Properties	
Young's Modulus (MPa)	Poisson's Ratio
64199	0.33
Plastic Properties	
True Stress (MPa)	Plastic Strain (mm/mm)
125.6832792	0
150.4775504	0.000205041
160.2845985	0.000303357
170.3320909	0.00080548
180.0267714	0.001790812
190.097664	0.006738819
195.1312865	0.009247006
198.0894111	0.01382541
196.0174998	0.01433491
197.5608947	0.01707262
195.8579317	0.017669238
192.9976085	0.02024891
192.8256328	0.024204124

Table A.9: Monotonic Material Model for 300°C R2

300°C	
Elastic Properties	
Young's Modulus (MPa)	Poisson's Ratio
71775	0.33
Plastic Properties	
True Stress (MPa)	Plastic Strain (mm/mm)
65.36856605	0
80.86100983	0.000260973
86.37203234	0.000810642
92.65372996	0.002948182
95.05462479	0.005110125
96.09962636	0.008469268
96.26710376	0.010345022
96.06389942	0.010821695
95.68473292	0.012109448

A.1.3 R3 Material Models

Table A.10: Monotonic Material Model for 25°C R3

25°C R3	
Elastic Properties	
Young's Modulus (MPa)	Poisson's Ratio
81180	0.33
Plastic Properties	
True Stress (MPa)	Plastic Strain (mm/mm)
150.8410391	0
200.0380191	0.000320411
225.1805046	0.00075972
250.0986825	0.002006841
275.0277116	0.004839453
280.0611073	0.005607413
300.4889737	0.00978846
310.9183312	0.013078045
314.935471	0.014745605
317.2280321	0.016256475

Table A.11: Monotonic Material Model for 150°C R3

150°C	
Elastic Properties	
Young's Modulus (MPa)	Poisson's Ratio
76730	0.33
Plastic Properties	
True Stress (MPa)	Plastic Strain (mm/mm)
205.4220114	0
212.2724655	0.000246408
220.9640838	0.000490833
230.0033604	0.000990448
241.3778114	0.0024666
252.1173868	0.004730054
262.8471045	0.008110503
270.3190291	0.01211256
274.4641927	0.016638335
274.2967079	0.021156869
260.2385151	0.023032558

Table A.12: Monotonic Material Model for 200°C R3

200°C	
Elastic Properties	
Young's Modulus (MPa)	Poisson's Ratio
68405	0.33
Plastic Properties	
True Stress (MPa)	Plastic Strain (mm/mm)
200.5362463	0
210.8055979	0.000301816
220.9559421	0.000772432
230.0263866	0.002521297
241.1657928	0.007119184
243.3185234	0.008395007
253.0680082	0.022465599
252.1571459	0.031147154
248.7103742	0.037808913
243.4992766	0.040933015

Table A.13: Monotonic Material Model for 300°C R3

300°C	
Elastic Properties	
Young's Modulus (MPa)	Poisson's Ratio
71441	0.33
Plastic Properties	
True Stress (MPa)	Plastic Strain (mm/mm)
70.72683388	0
80.72647112	0.000202605
86.22696714	0.002099024
85.77336512	0.002108248
90.06595787	0.003145289
93.04353166	0.004214696
94.04809165	0.005415184
96.06993368	0.006110053
95.65039542	0.006614207
96.65373478	0.010239071
96.36562899	0.012137077
98.41307799	0.014218178
98.18706257	0.01841758
98.85091531	0.021311199
95.30042173	0.028116275

A.2 Cyclic Loading Material Models

A.2.1 R1 Cyclic Loading Material Models

Table A.14: Cyclic Material Model for 25°C R1

25°C	
Elastic Properties	
Young's Modulus (MPa)	Poisson's Ratio
73852	0.33
Plastic Properties	
Kinematic Hardening	
True Stress (MPa)	Plastic Strain (mm/mm)
52.29592563	0
98.66554542	0.000388073
119.649166	0.000596407
131.2664307	0.000726965
149.5425713	0.000984584
163.0194033	0.001197725
173.0510821	0.001363358
182.4359105	0.001546485
194.1632923	0.001788189
235.8530945	0.003208834
Isotrpic Hardening	
True Stress (MPa)	Plastic Strain (mm/mm)
52.29592563	0
134.1601356	0.001662274
145.86513	0.008311372
148.5945418	0.014954332

Table A.15: Cyclic Material Model for 150°C R1

150°C	
Elastic Properties	
Young's Modulus (MPa)	Poisson's Ratio
78538	0.33
Plastic Properties	
Kinematic Hardening	
True Stress (MPa)	Plastic Strain (mm/mm)
24.42178117	0
119.6775665	0.000968916
127.3211416	0.001374608
137.34782	0.001547229
140.7967108	0.002002967
146.2898786	0.002332575
153.0369584	0.002554858
158.418847	0.002770643
162.7781848	0.003124699
179.9895812	0.004896981
Isotrpic Hardening	
True Stress (MPa)	Plastic Strain (mm/mm)
24.42178117	0
110.2279736	0.0024
118.3987299	0.012374466
135.0243067	0.020965284

Table A.16: Cyclic Material Model for 200°C R1

200°C	
Elastic Properties	
Young's Modulus (MPa)	Poisson's Ratio
75657	0.33
Plastic Properties	
Kinematic Hardening	
True Stress (MPa)	Plastic Strain (mm/mm)
31.9012184	0
37.71208989	0.000115258
50.08867277	0.000165237
63.96376352	0.00024437
105.2699683	0.000960786
109.374058	0.001054959
121.2429221	0.001634358
143.7186801	0.003934121
148.8258554	0.004648713
150.7755321	0.005180299
Isotrpic Hardening	
True Stress (MPa)	Plastic Strain (mm/mm)
31.9012184	0
101.5572366	0.002636857
109.23262	0.013184284
119.0100152	0.02373171

Table A.17: Cyclic Material Model for 250°C R1

250°C	
Elastic Properties	
Young's Modulus (MPa)	Poisson's Ratio
68498	0.33
Plastic Properties	
Kinematic Hardening	
True Stress (MPa)	Plastic Strain (mm/mm)
62.53691072	0
81.14546289	0.00186753
85.24211338	0.002294767
85.54263533	0.002601469
88.96351719	0.003047476
89.50940213	0.003427144
91.70690794	0.003690735
91.98060369	0.00399394
92.22769018	0.004383438
94.78797505	0.005048735
Isotrpic Hardening	
True Stress (MPa)	Plastic Strain (mm/mm)
62.53691072	0
68.97093372	0.003495591
71.10900341	0.017477956
72.70674274	0.031460321

Table A.18: Cyclic Material Model for 300°C R1

300°C	
Elastic Properties	
Young's Modulus (MPa)	Poisson's Ratio
57195	0.33
Plastic Properties	
Kinematic Hardening	
True Stress (MPa)	Plastic Strain (mm/mm)
11.83579775	0
27.73879131	0.000825832
28.42301348	0.000985869
29.50432888	0.001134509
30.62553202	0.001424123
33.84130596	0.002598758
35.26584349	0.003467438
36.5697076	0.004958791
37.03350902	0.005586346
Isotrpic Hardening	
True Stress (MPa)	Plastic Strain (mm/mm)
11.83579775	0
29.09371256	0.003910268
32.64449047	0.019551341
38.34190289	0.035192414

VITA AUCTORIS

NAME:	Luke Miller
PLACE OF BIRTH:	Windsor, ON
YEAR OF BIRTH:	1987
EDUCATION:	Essex District High School, Essex, ON, 2005
	St. Clair College, Eng. Tech. Diploma, Windsor, ON, 2009
	University of Windsor, BASc., Windsor, ON, 2011